Coronal magnetic energy release by current sheet reconnection

A thesis presented to
The University of Waikato
in fulfillment of the thesis requirement
for the degree of

Doctor of Philosophy

by

Jacob Heerikhuisen

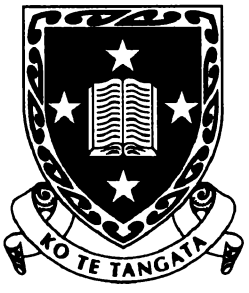

The University of Waikato
Te Whare Wānanga o Waikato

The University of Waikato
September, 2001

Preface

The work in this thesis often builds on the work of previous authors. However, the main body of results presented in Chapters 4 to 7 were all obtained and analysed by the present author. Chapters 2 and 3 provide a basis for the later chapters of original work.

Matlab was used to analyse almost all the data obtained from numerical codes. The exception being the multiple null work of Chapter 5, where we used IDL instead. All Matlab routines were written by me, while the IDL routines were pre-existing.

Chapter 4 provides numerical confirmation of the analytic results reviewed in Chapter 3. The 2-D code used in Section 4.1, "MHD2D", was written and first used by Craig and Watson (1999). This code was used with only minor modifications. The numerical results of this section (along with those of Sections 5.1, 5.2, 5.4 and 5.5) appeared in Heerikhuisen, Craig and Watson (2000). The basic 3-D code of Section 4.2 was written by I.J.D. Craig, but I modified this to include 4th-order differences and accurate control of the time-step. The numerical results of this Chapter are all original, though at times they reconfirm known results.

Chapter 5 investigates some of the secondary effects associated with magnetic merging. The saturation work of Section 5.2 reconfirms the results of Craig and Watson (1999), and uses a version of their code which I modified to take advantage of the four-fold symmetry present in head-on merging simulations. The compressible results are completely new. I wrote the compressible code and experimented with pseudo-viscosity before settling on the complicated flux corrected transport algorithm to eliminate numerical over-shoot. The osculation analysis of Section 5.4 has been done many times before, but only for a steady-state situation. I showed that time-dependent effects undo osculation and did some numerical simulations (using my symmetric version of the MHD2D code) which backed this up. Section 5.5 represents a numerical investigation into the tearing mode, again using the MHD2D code. I fruitlessly investigated head-on merging (using my symmetric version of MHD2D) for tearing, before redoing one of Biskamp's calculations. I finally did find magnetic islands forming in the context of sheared reconnection.

Most of the background work for Chapter 6 appears in Craig and Fabling (1996) and the PhD thesis of Fabling (1997). The major extension with the multiple null work came when I decided to investigate more than one ring of outer nulls, and Section 6.3 details these new results. All the work of Chapter 6 appears in Craig, Fabling, Heerikhuisen and Watson (1999). The code used for the numerical results in this chapter was written entirely by P.G. Watson.

Chapter 7 provides a new application of the reconnection solutions reviewed in Chapter 3 to investigate the energy of protons accelerated in reconnecting coronal magnetic fields. The code and routines used here were written entirely by myself. This work is to appear in a joined paper (Heerikhuisen, Litvinenko and Craig, 2001).

Abstract

In this thesis we investigate the rapid release of energy in the solar corona, with a particular view to understanding the solar flare in which magnetic reconnection is thought to play a key role. A review of existing reconnection solutions is given in Chapters 2 and 3, with new analytic and numeric results are presented in subsequent chapters.

Although much of the work in this thesis is computational, numerical investigations are always motivated theoretically. In Chapters 4 and 5 several aspects of two dimensional reconnection are investigated using a periodic time-dependent incompressible code. One of the main points is to check the veracity of the analytic solution of Craig and Henton (1995) by running the code from general initial conditions. Other aspects of 2-D merging covered include the tearing mode instability, osculation and the effects of finite compressibility.

We employ a 3-D time-dependent code, in Chapter 4, to check that the analytically predicted spine and fan forms develop from general initial conditions. Scalings with resistivity of the associated current structures are also investigated. Most of the analytic work so far has revolved around single null magnetic configurations. Chapter 6 focuses on reconnection solutions in the presence of multiple nulls. Finally, we look at an application of the analytic theory in the context of particle acceleration. In Chapter 7 we trace proton orbits using a physically plausible analytic current sheet solution.

Acknowledgements

First and foremost I would like to thank my supervisor Associate Professor Ian Craig. He always had things for me to do, yet I never felt pressured. I am also grateful for funding received to attend two ANZIAM conferences. Of course my visit to the University of New Hampshire was also partially funded by Ian and my second supervisor Associate Professor Alfred Sneyd's Marsden grant. To this end I am also grateful to Yuri Litvinenko who co-funded the UNH visit, and for making me feel welcome there.

Secondly Dr. Paul Watson who was always willing to lend me a helping hand. He also deserves a big thanks for the many hours of proof reading he had to endure.

Dr. Stephen Joe was at times extremely helpful with LaTeX and enigmatic computing problems, despite his catch phrase "read the documentation".

I would also like to thank my fellow PhD students Farhad Ali and David Harder. They have been a great source of help, since the three of us often encountered similar hurdles in our daily research.

Saving the best for last, it is my pleasure to thank my dearest Sivajah Somasundaram, whose support was invaluable and whose meticulous proof reading helped remove many unwanted errors from this thesis.

Contents

Chapter 1

Introduction

1.1 Solar flares

Ever since the dawn of civilisation has man looked up at the Sun. As telescopes became prevalent over the last few centuries, following their invention by Galileo, it was realised that there is considerable structure to the glowing orb. Sunspots in particular attracted interest and their positions and durations were meticulously recorded (see Bray and Loughhead, 1979). Later still it was realised that these sunspots are intimately related to the Sun's complicated magnetic field. These days several satellites and many ground based observatories monitor the Sun, and in particular the activity associated with its ever changing magnetic field. Detailed accounts of the Sun's magnetic activity can be found, for example, in Priest (1984), Stix (1989) and Golub and Pasachoff (1997). In the rest of this chapter we give a brief overview of material relevant to the present body of work.

The source of the Sun's energy is nuclear fusion. Within the core the temperature and gravitational pressure are high enough to sustain the fusion of hydrogen to helium. The heat generated within the core is sufficient to ionize all gases present, so that the Sun constitutes entirely of plasma. Thermal energy from the core initially moves out via radiation. About 3/4 of the way to the surface, temperature gradients and density are such that convective instabilities develop. Hence the region from here to the surface is known as the convection zone (see Figure 1.1). Observations of the surface of the Sun confirm the presence of convection cells, also known as granules.

Above the surface lies the solar atmosphere which is divided into three distinct regions. Lowest is a very thin layer known as the photosphere. This region is still relatively dense and emits most of the solar radiation. Just above this lies the slightly less dense chromosphere. Then, over a very narrow transition region the temperature and density change dramatically as we enter the corona. The corona

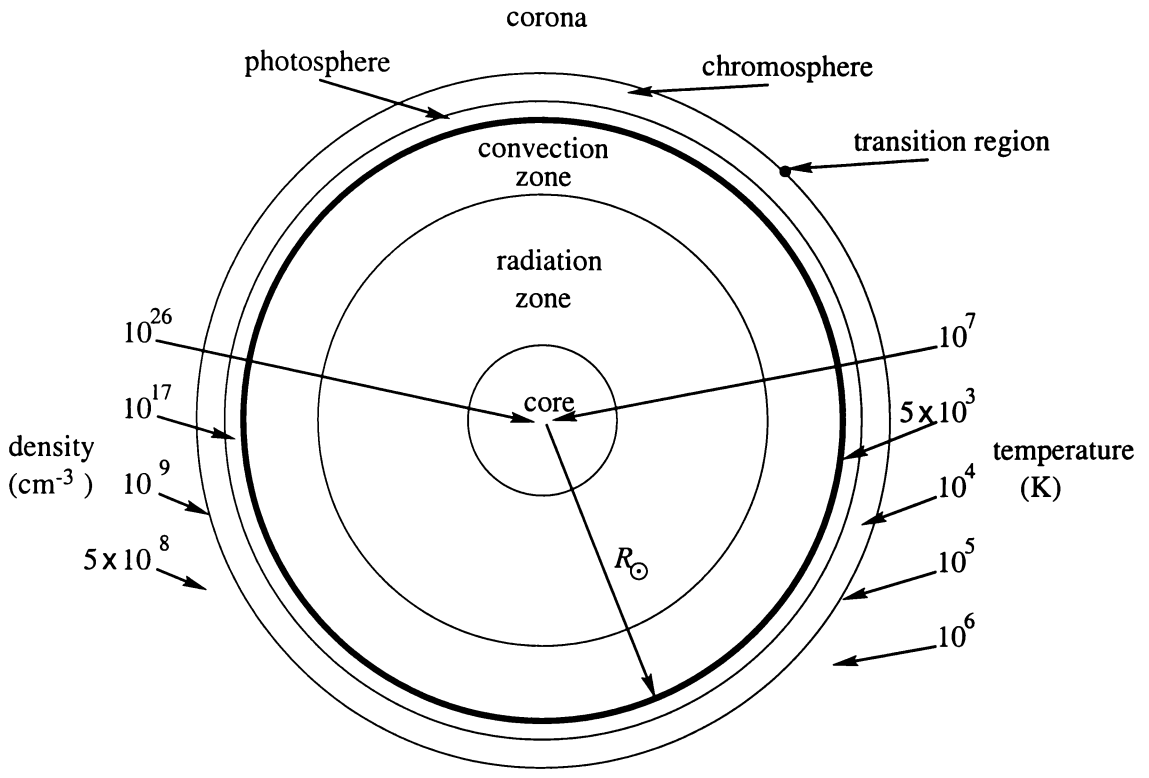

Figure 1.1: Schematic slice through the Sun depicting the various layers present (Priest, 1984) (note that in reality these layers are intermingled with often highly corrugated interfaces). Here $R_\odot = 6.96 \times 10^8 m$ is the solar radius. Typical number densities of the various regions are shown on the left, while typical temperature values are shown on the right. For comparison, the number density and temperature at the surface of the Earth are $10^{19} cm^{-3}$ and $300K$.

is the Sun's outermost layer. Its very low density makes it appear as a transparent envelope around the rest of the Sun, visible only during an eclipse when the much brighter photosphere is hidden. The corona extends out well beyond the Earth's orbit, and the extremely high temperature of the low corona is somewhat of a mystery.

The Sun has a strong magnetic field associated with it (many thousands of times greater than that of the Earth). Since the plasma provides almost no resistance to the flow of electric current, magnetic field is effectively "frozen" into it. This means that magnetic field is stretched and tangled due to the convective motion of the plasma. This stretching and tumbling amplifies the field and represents the basic dynamo mechanism which is believed to be the source of the Sun's magnetic field.

The dynamo effect responsible for the magnetic field tends to create tubes of magnetic flux. Due to the associated magnetic pressure, plasma inside such a tube is less dense than its surroundings. This causes tubes of magnetic field to "float"

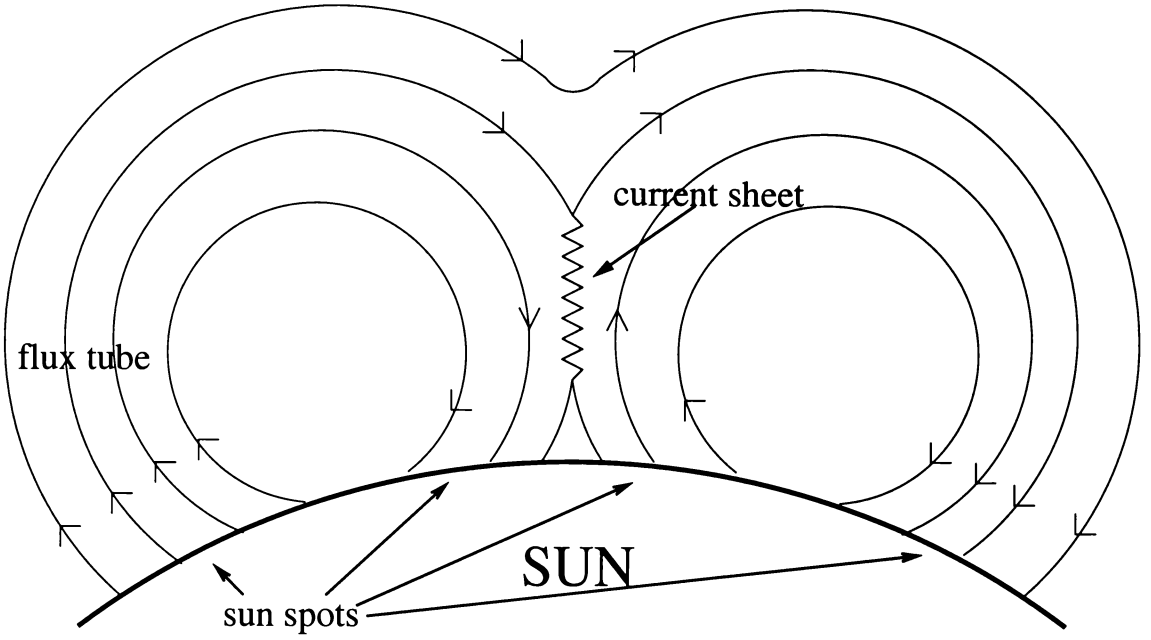

Figure 1.2: Schematic diagram showing the merging of magnetic loops in the Sun's corona.

to the surface where they sprout into the corona. Large flux tubes that erupt from the Sun's surface are anchored by a pair of sunspots (see Figure 1.2). This effect explains why countless loops of magnetic field appear to be threading the solar surface in a random way. As such the Sun's magnetic structure is in stark contrast to the distinct dipole magnetic structure of the Earth, which is in fact very similar to that of a simple bar magnet.

The convection driving the field generation is a dynamic process, so that many flux loops are entering the corona at any time, while their foot-points are all moving relative to each other. This leads to highly stressed states within the coronal magnetic structure. Observations of the corona (see for example Sturrock (1980), or more recent satellite data from YOHKOH (Bentley and Mariska, 1996) and SOHO (available on their website)) confirm that the magnetic energy locked up in such stressed configurations, typically covering length scales of the order of the diameter of the Earth, can be released explosively over a time scale of only a few minutes. This phenomenon is known as the solar flare.

A typical flare event is characterised by a "precursor" phase, "impulsive" or "flash" phase, and a decay phase (Stix, 1989). The precursor phase consists of thermal radiation of up to 10^7K. This is followed by the impulsive phase which typically lasts around 1 minute and consists of bursts in γ-rays, X-rays and microwave radiation. These outbursts are concluded by a slow decay phase lasting around 30

minutes. Other than radiation and fluid motion, some of the flare energy is released via energetic particles. Electrons in the 10-100 keV range and protons in the 10-100 MeV range are common, with some protons getting as high as several GeV.

The total energy released by a flare event ranges from 10^{27} to 10^{32} ergs (10^{25} Joules) — around 100 million times more powerful than the biggest man-made nuclear explosion. Consider the total magnetic energy within a $10^{9.5}$ cm cube of 100 Gauss field, these figures being typical of coronal magnetic merging conditions. Multiplying the magnetic energy density $B^2/8\pi$ by the volume gives a total energy of 10^{32} ergs. Clearly the magnetic field has the energy potential. However, the low resistance means that static diffusion will only release this amount of energy over the space of a million years! Since there appear to be no other viable sources to account for this quantity of energy, the question is: what mechanism allows the magnetic field to release energy so explosively?

Though an interesting phenomenon in its own right, solar flare research has received some prominence in recent times since such outbursts have been linked to telecommunication disruptions on Earth. A large proportion of the flare energy is converted to kinetic energy of charged particles, and if the Earth is in the path of such a barrage these can cause major damage. Clearly the ability to predict a flare eruption would save power and telecommunication companies millions of dollars. Knowing when a large quantity of high energy charged particles is due to strike is also critical to space missions, since astronauts themselves are at risk once they leave the relative safety of the Earth's magnetic field. Finally, the military is interested in knowing when their sensitive detection equipment is likely to be overpowered by a radiation outburst from the Sun. Of course, at such times the enemy's detection equipment will also be inoperable.

Predicting solar flares can be compared to predicting when and where an earthquake will strike. There are certain precursors and indicators, but it is far from an exact science. In fact only over the last decade or so have realistic models of the energy release mechanism been developed. Even now, a description which takes all factors into account eludes us. One aspect of the flare mechanism has become almost universally accepted however: the key role that magnetic reconnection plays in the rapid conversion of magnetic energy. Understanding the solar flare mechanism is the prime motivation of the reconnection studies within this thesis. In-depth accounts of magnetic reconnection and its various applications can be found, for example, in Priest and Forbes (2000) and Parker (1994).

1.2 Magnetic reconnection

Magnetic reconnection is the breaking and rejoining of pairs of magnetic field lines. For example, Figure 1.3 shows how a pair of field lines CA and BD may reconnect to form BA and CD. This change in magnetic field line connectivity allows reconnection to release energy locked up in the magnetic field topology.

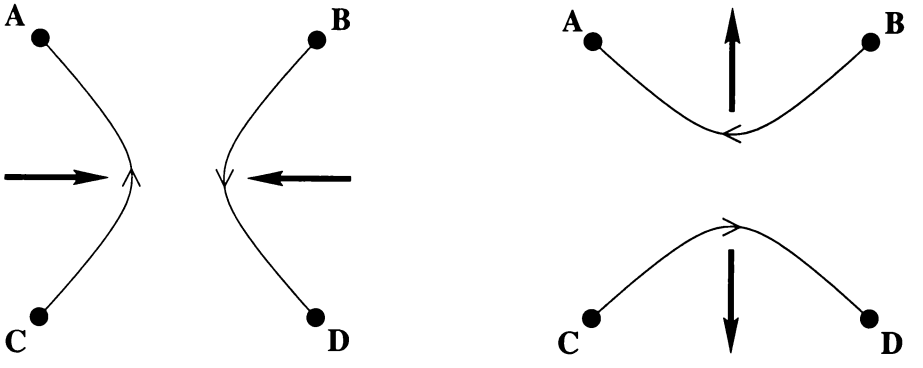

Figure 1.3: Magnetic lines of force are pushed together (left) before reconnecting to a different topology (right). Tension in the reconnected field lines pulls them apart.

Figure 1.2 shows two coronal loops of magnetic field being driven together. This is the essence of early models such as that by Sweet (1958). Due to the plasma's extremely low resistance, it is only in regions of high electric current that magnetic field lines can move independently of the plasma (diffuse), and reconnection occurs. Of course large currents form at places of steep magnetic gradient, and steep magnetic gradients occur when anti-parallel fields are pushed together. As such, rapid reconnection is a result of both advection and diffusion. Figure 1.4 shows a close-up of the current sheet region of Figure 1.2. X-point configurations such as this form the basis of most reconnection models.

As mentioned before, the coronal plasma is highly conducting and it is this extremely low electrical resistance that creates difficulties when we attempt to solve the physical equations governing the system. On one hand, since it is so small, a good approximation would seem to be to set resistivity to zero. Unfortunately such a simplification precludes reconnection, since in this limit field lines cannot diffuse at all. As we shall see, a solution's behaviour with respect to resistivity is a critical factor in determining its energy release properties.

1.3 Thesis overview

This thesis is set out as follows. In the next chapter we will introduce the governing MHD equations and review four classic planar merging models put forward by Sweet

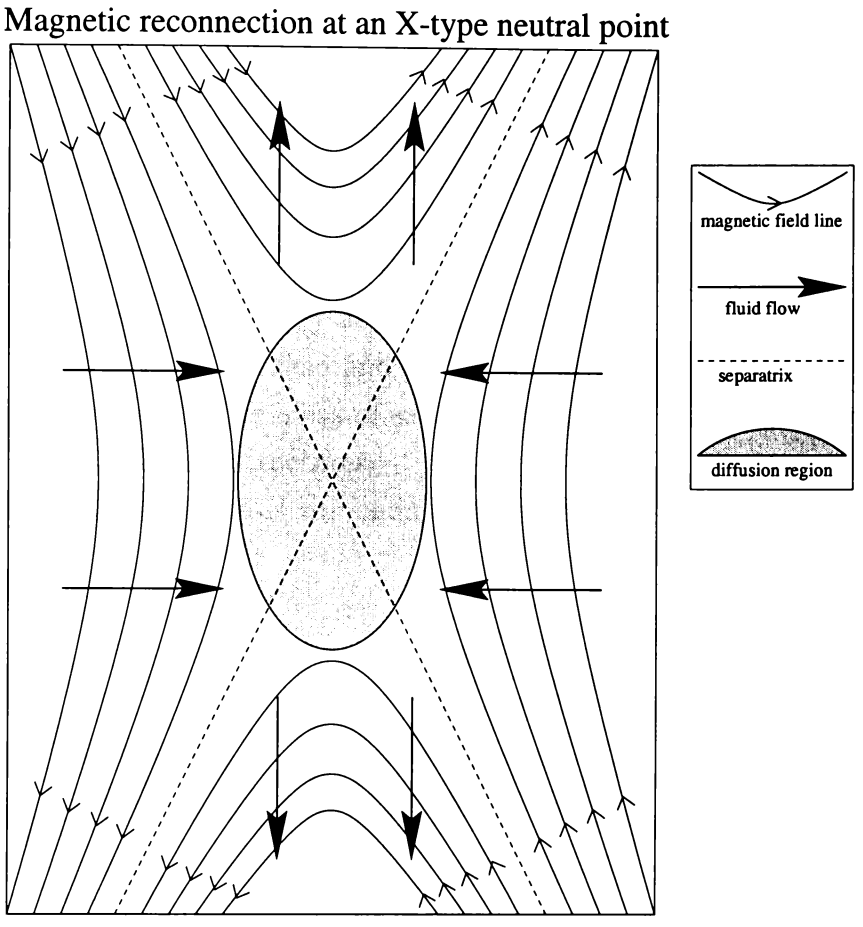

Figure 1.4: Close-up of the current region in Figure 1.2. This represents the prototypical X-point configuration where anti-parallel magnetic fields meet at a current sheet (diffusion region) and are reconnected.

(1958), Parker (1963), Petschek (1964), Syrovatskii (1971), and Sonnerup and Priest (1975) respectively. These models provide the conceptual basis for much of the work in later chapters.

Analytic solutions discovered more recently (Craig and Henton (1995); Craig, Fabling, Henton and Richard (1995); Craig and Fabling (1996)) will be reviewed in Chapter 3. The properties of these solutions, particularly their behaviour with respect to resistivity, will also be investigated.

In Chapter 4 we present a range of numerical solutions which are intended to test the predicted forms of the analytic solutions of Chapter 3. The MHD equations are solved numerically in both two and three dimensions, and a detailed comparison with the properties of the analytic solutions is made.

Chapter 5 investigates five topics of two dimensional magnetic merging. We firstly take a detailed look at the influence of a shear component in the velocity field. We then go on to investigate several aspects of magnetic merging which provide corrections to the generic solutions of the preceding two chapters. Saturation of the

current layer is covered, along with osculation, compressibility and the tearing mode instability.

Reconnection geometries containing multiple nulls is the subject of Chapter 6. We review previous work by Fabling (1997), and present extensions which encompass aspects of spine, fan and separator reconnection models.

Chapter 7 represents an application of the exact solutions reviewed in Chapter 3. Here we investigate the energy and trajectory properties of protons accelerated in both the standard X-point field and the field obtained from the Craig & Henton solution. We include also the ideas of saturation and equalisation in obtaining the magnetic and electric field structures.

Finally Chapter 8 contains the summary and conclusions of the work in this thesis.

Chapter 2

MHD equations and early reconnection models

In this chapter we will introduce the system of equations used throughout this thesis. These will then be non-dimensionalised, before we look at a few of their generic properties. The second section of this chapter reviews some early models and solutions to the coronal reconnection problem. As such, the present discussion provides the background material for the later chapters, in particular Chapter 3 which introduces more recent exact analytic solutions.

2.1 Governing equations

We assume the system is governed by the magnetohydrodynamic (MHD) equations. The MHD equations are a combination of Maxwell's equations and the equations of fluid dynamics. This approximation treats the plasma as collision dominated, in other words we assume that the mean free path of protons and electrons is much smaller than the typical length scales involved. The orbits of individual charged particles will be investigated in Chapter 7. In what follows we will work in the cgs system of units, before imposing our non-dimensionalisation.

2.1.1 Primitive equations

Maxwell's equations for an electric field $\mathbf{E}$ and magnetic field $\mathbf{B}$, along with a charge density $\bar{q}$ and current density $\mathbf{J}$, can be written in cgs units (e.g. Parker, 1979) as

$$4\pi\mathbf{J} + \frac{\partial \mathbf{E}}{\partial t} = c\nabla \times \mathbf{B} \tag{2.1}$$

$$\frac{\partial \mathbf{B}}{\partial t} = -c\nabla \times \mathbf{E} \tag{2.2}$$

$$\nabla \cdot \mathbf{E} = 4\pi\bar{q} \tag{2.3}$$

$$\nabla \cdot \mathbf{B} = 0\,, \tag{2.4}$$

where c is the speed of light. To model the plasma as a fluid we firstly require conservation of mass. This is reflected in the continuity equation for a velocity field $\mathbf{v}$ and a density profile ρ

$$\frac{\mathrm{D}\rho}{\mathrm{D}t} + \rho\nabla\cdot\mathbf{v} = 0\,, \tag{2.5}$$

where $\mathrm{D}/\mathrm{D}t = (\partial/\partial t + \mathbf{v}\cdot\nabla)$ is the advective derivative. Secondly, the motion of a fluid element will depend on the forces acting on it. Not only do we have a pressure gradient as per standard fluid dynamics, but now there is also the Lorentz force due to the magnetic field. This condition leads to the momentum equation

$$\rho\frac{\mathrm{D}\mathbf{v}}{\mathrm{D}t} = \frac{1}{c}(\mathbf{J}\times\mathbf{B}) - \nabla p\,, \tag{2.6}$$

where p the plasma pressure.

The electric field $\mathbf{E}'$ in the frame of the fluid is

$$\mathbf{E}' = \mathbf{E} + \frac{1}{c}\mathbf{v}\times\mathbf{B}\,. \tag{2.7}$$

Ohm's law states that

$$\mathbf{J}' = \sigma\mathbf{E}'\,, \tag{2.8}$$

where the electric conductivity is given by $\sigma \simeq 10^7 T^{3/2} \simeq 10^{16}\ \mathrm{s}^{-1}$ (cgs) for a fully ionized coronal plasma at temperature $T = 10^6 K$ (Parker, 1994). Since MHD is not a relativistic theory, we can take $\mathbf{J}' = \mathbf{J}$. Combined with (2.7) this gives

$$\mathbf{J} = \sigma(\mathbf{E} + \frac{1}{c}\mathbf{v}\times\mathbf{B})\,.$$

We now substitute this into Ampere's law

$$4\pi\mathbf{J} = c\nabla\times\mathbf{B}\,, \tag{2.9}$$

where we have ignored the displacement current (see equation (2.1)) since it is of order v/c. This gives us the result

$$\mathbf{E} = \left(\frac{c}{4\pi\sigma}\right)\nabla\times\mathbf{B} - \frac{1}{c}\mathbf{v}\times\mathbf{B}\,. \tag{2.10}$$

If we now define the resistivity

$$\bar{\eta} = \frac{c^2}{4\pi\sigma}\,, \tag{2.11}$$

the above becomes

$$\mathbf{E} = \frac{\bar{\eta}}{c}\nabla\times\mathbf{B} - \frac{1}{c}\mathbf{v}\times\mathbf{B}\,. \tag{2.12}$$

Taking the curl of this, and using (2.2) we obtain the induction equation

$$\frac{\partial\mathbf{B}}{\partial t} = \nabla\times(\mathbf{v}\times\mathbf{B}) + \bar{\eta}\nabla^2\mathbf{B}\,. \tag{2.13}$$

Equations (2.5), (2.6), (2.13) and (2.4) represent the MHD system of equations for a conducting fluid. We will now look at the process of non-dimensionalising these equations.

2.1.2 Non-dimensionalisation

The above equations are more convenient to work with once we non-dimensionalise them for our coronal reconnection problem. We reparameterise with respect to the following typical coronal values (see for example Priest, 1984).

$$\rho_c \simeq 10^{-14}\mathrm{g/cm}^3 \tag{2.14}$$

$$B_c \simeq 10^2\mathrm{G} \tag{2.15}$$

$$L_c \simeq 10^{9.5}\mathrm{cm} \tag{2.16}$$

Note that ρ_c corresponds to a number density of $n_c \simeq 10^{10}\mathrm{cm}^{-3}$, if we assume that the plasma consists almost exclusively of electrons and protons. From these we can define the Alfvén speed and the Alfvén time.

$$v_A = \frac{B_c}{\sqrt{4\pi\rho_c}} \simeq 10^{8.5}\mathrm{cm/s} \tag{2.17}$$

$$t_A = \frac{L_c}{V_A} \simeq 10\mathrm{s} \tag{2.18}$$

We also define the plasma beta, the ratio of gas pressure to magnetic pressure, as

$$\beta_p = \frac{p_c}{B_c^2/8\pi} \simeq 10^{-2}\,. \tag{2.19}$$

Using $p_c = n_c k T_c$, this corresponds to a coronal temperature of 10^6K.

Combining all the previous results we can write the non-dimensional MHD equations as follows:

$$\frac{\partial\rho}{\partial t} + \nabla\cdot(\rho\mathbf{v}) = 0 \tag{2.20}$$

$$\rho\left(\frac{\partial\mathbf{v}}{\partial t} + (\mathbf{v}\cdot\nabla)\mathbf{v}\right) = (\nabla\times\mathbf{B})\times\mathbf{B} - \beta_p\nabla p \tag{2.21}$$

$$\frac{\partial\mathbf{B}}{\partial t} = \nabla\times(\mathbf{v}\times\mathbf{B}) + \eta\nabla^2\mathbf{B} \tag{2.22}$$

$$\nabla\cdot\mathbf{B} = 0\,. \tag{2.23}$$

Here

$$\eta = \frac{\bar{\eta}}{L_c v_A} \tag{2.24}$$

is the inverse Lundquist number. In these units $\eta \simeq 10^{-14}$. As we shall see, the smallness of η greatly affects the dynamics of the magnetised fluid.

2.1.3 Ideal MHD

Let us, for a moment, consider the case of ideal MHD where we set $\eta = 0$. This should be a good approximation given that the plasma provides almost no resistance

to the flow of current. In this limit, however, the magnetic field is "frozen" into the fluid. In other words, the magnetic flux associated with a fluid line element remains fixed. This means magnetic field can only be advected and not diffused, and reconnection is not possible. To see why this is so, let us consider the time evolutions of magnetic flux and a fluid line element.

Using equations (2.20) and (2.22) (with $\eta = 0$) we have

$$\begin{aligned}\frac{\partial}{\partial t}\left(\frac{\mathbf{B}}{\rho}\right) &= \frac{1}{\rho}\nabla \times (\mathbf{v} \times \mathbf{B}) + \frac{\mathbf{B}}{\rho^2}\nabla \cdot (\rho \mathbf{v}) \\ &= \frac{1}{\rho}\left[(\mathbf{B} \cdot \nabla)\mathbf{v} - (\mathbf{v} \cdot \nabla)\mathbf{B} - \mathbf{B}(\nabla \cdot \mathbf{v})\right] + \frac{\mathbf{B}}{\rho^2}\left[\rho(\nabla \cdot \mathbf{v}) + \nabla\rho \cdot \mathbf{v}\right] \\ &= \frac{1}{\rho}(\mathbf{B} \cdot \nabla)\mathbf{v} - (\mathbf{v} \cdot \nabla)\left(\frac{\mathbf{B}}{\rho}\right) .\end{aligned}$$

Hence, by definition of the advective derivative $D/Dt = \partial/\partial t + \mathbf{v} \cdot \nabla$, magnetic flux evolves according to

$$\frac{\mathrm{D}}{\mathrm{D}t}\left(\frac{\mathbf{B}}{\rho}\right) = \left(\frac{\mathbf{B}}{\rho} \cdot \nabla\right)\mathbf{v} . \tag{2.25}$$

Consider now the advection of a fluid line element $\delta\mathbf{l}$. Suppose at a given point in time $\delta\mathbf{l}$ is the line element between $\mathbf{x}$ and $\mathbf{x} + \delta\mathbf{l}$. An instant later the ends have been advected by the flow rates $\mathbf{u}(\mathbf{x})$ and $\mathbf{u}(\mathbf{x} + \delta\mathbf{l})$ as depicted in Figure 2.1.

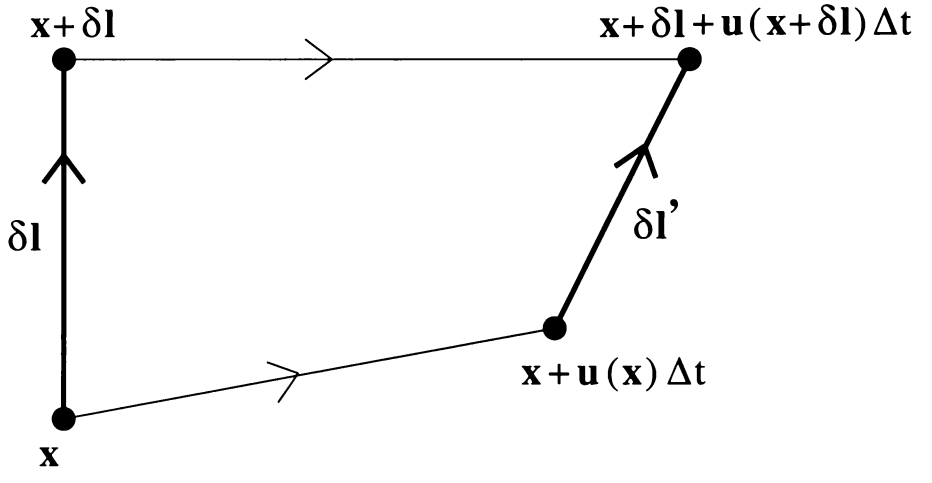

Figure 2.1: Advection of fluid line element $\delta\mathbf{l}$ by a velocity field $\mathbf{u}$.

By writing

$$\mathbf{u}(\mathbf{x} + \delta\mathbf{l}) = \mathbf{u}(\mathbf{x}) + U_{ij}\,\delta\mathbf{l} ,$$

where $U_{ij} = \partial u_i/\partial x_j$, we can see that

$$\delta\mathbf{l}' = \delta\mathbf{l} + (\delta\mathbf{l} \cdot \nabla)\mathbf{u}\,\Delta t .$$

Hence a fluid line element will be advected according to

$$\frac{D}{Dt}\delta\mathbf{l} = (\delta\mathbf{l} \cdot \nabla)\mathbf{u} . \tag{2.26}$$

The above analysis shows that $\mathbf{B}/\rho$ behaves exactly as a fluid line element, and hence magnetic field lines do not move with respect to the fluid in the ideal $\eta = 0$ approximation. This restriction, however, does allow the material to travel *along* the field lines. In practice the "frozen in" condition applies to regions of low current, since under such conditions the resistive term in the induction equation is exceedingly small.

2.1.4 Ohmic dissipation rate

Rapid release of energy is the prime objective of most reconnection work. To help quantify this we employ the Ohmic dissipation rate defined as

$$W_\eta = \eta \int_V J^2 \mathrm{d}V \ , \tag{2.27}$$

where J is the current density and V the volume in question. We can now define two distinct classes of solutions, based upon whether the Ohmic dissipation rate scales as a positive or negative power of η. We will say that a solution represents "fast" reconnection if $W_\eta \sim \eta^k$, where $k \leq 0$. All other solutions will be classed as "slow".

Remembering that our aim is to understand the rapid release of energy within the solar corona, "fast" solutions will be of primary interest. However, since such solutions predict infinite dissipation in the limit $\eta \to 0$, we cannot expect solutions with this property to be valid for all values of resistivity on physical grounds. The merits and limitations of the various solutions will be discussed as they appear.

2.2 Early magnetic reconnection models

We now introduce four magnetic merging models. The first, Sweet-Parker, is an order of magnitude analysis which will be referred to often in the rest of this thesis. The second, by Petschek, is a reconnection model similar to Sweet-Parker, except that it makes more (some questionable) assumptions which improve its energy dissipation properties. We also mention Syrovatskii's solution to the merging problem when resistivity is absent. Finally we introduce the resistive incompressible merging solution of Sonnerup and Priest. This last model is an exact annihilation solution and turns out to be a special case of the reconnection solutions reviewed in Chapter 3.

It should be stressed that neither the resistive models of Sweet-Parker or Petschek represent exact solutions to the MHD equations. In Chapter 3 we will introduce a family of exact solutions. These are much more recent than the four models mentioned here, and encompass the Sonnerup and Priest solution of Section 2.2.4.

2.2.1 Sweet-Parker model

The Sweet-Parker mechanism represents a heuristic model based on the X-point geometry of Figure 1.4. This model was first suggested by Sweet (1958) and analysed by Parker (1957, 1963) who also performed an order of magnitude calculation.

Let us examine the configuration shown in Figure 2.2, where we have nearly anti-parallel fields being washed into a current sheet of length λ with a velocity u. The fields reconnect at the neutral point and are expelled through a narrow jet of width l with velocity v.

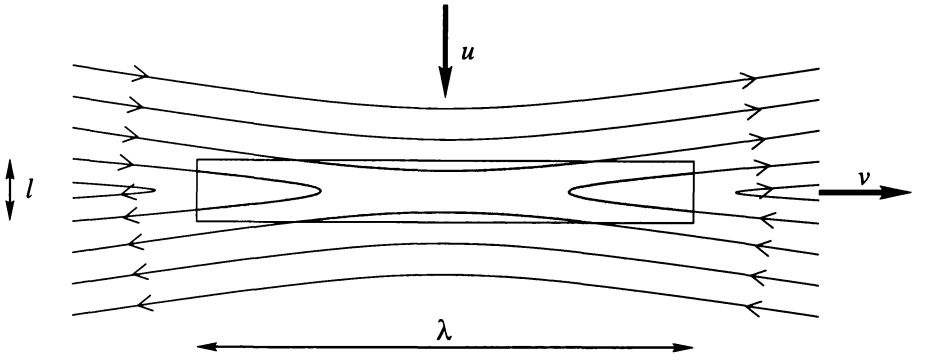

Figure 2.2: Sweet-Parker reconnection geometry. Nearly anti-parallel magnetic field reconnects at a current sheet (shaded region) of fixed length λ and width l which varies with resistivity.

Conservation of mass implies

$$\rho_{\rm in} u\lambda = \rho_{\rm out} v l \ . \tag{2.28}$$

For the rest of this analysis we will adopt the incompressible approximation (by setting $\rho = 1$ everywhere) for analytic simplicity, since the scaling results remain the same.

Along the inflow axis the momentum equation (2.21) reduces to

$$\frac{\rm d}{{\rm d}y}\left(\frac{1}{2}u^2 + p + \frac{1}{2}B_x^2\right) = 0 \ , \qquad (x = 0) \ ,$$

while along the outflow axis it implies

$$\frac{\rm d}{{\rm d}x}\left(\frac{1}{2}v^2 + p + \frac{1}{2}B_y^2\right) = 0 \ , \qquad (y = 0) \ .$$

Integrating these we have

$$p_0 - p_{\rm in} = \frac{1}{2}u^2 + \frac{1}{2}B_{\rm in}^2 \qquad (\text{along } x = 0) \tag{2.29}$$

$$p_0 - p_{\rm out} = \frac{1}{2}v^2 + \frac{1}{2}B_{\rm out}^2 \qquad (\text{along } y = 0) \ . \tag{2.30}$$

Here p_0 is the pressure at the origin where both the magnetic and velocity fields vanish. In the above equations $p_{\rm in}$, $p_{\rm out}$, u and $B_{\rm out}$ will all be comparatively small quantities. This is because for the inflow the magnetic field is large, so that $p_0 \simeq B_{\rm in}^2/2$, while for the outflow the velocity is large, so that $p_0 \simeq v^2/2$. Hence we deduce that

$$v \simeq B_{\rm in} \ . \tag{2.31}$$

This means that the Alfvén speed within the sheet is determined by the field strength just outside the sheet. Substituting this result into (2.28) yields

$$l \sim \frac{u\lambda}{B_{\rm in}} \ . \tag{2.32}$$

We can now equate the magnetic energy advected into the current sheet with the energy dissipated through Ohmic heating (2.27), so that we have

$$uB_{\rm in}^2\lambda \sim \eta \left(\frac{B_{\rm in}}{l}\right)^2 l\lambda \ , \tag{2.33}$$

where we have used $J \sim B_{\rm in}/l$. This reduces to

$$u \sim \frac{\eta}{l} \ .$$

Keeping our global magnetic field $B_{\rm in}$ and length scale λ fixed with η we deduce from (2.32) and (2.33) that

$$l \sim \eta^{1/2} \quad , \quad u \sim \eta^{1/2} \ . \tag{2.34}$$

Hence the corresponding Ohmic dissipation rate will scale as

$$W_\eta \sim \eta^{1/2} \ . \tag{2.35}$$

The above analysis shows that the magnetic energy conversion $W_\eta \to 0$ as $\eta \to 0$. Since η is exceedingly small, the above analysis, which is dimensionally correct, does not bode well for magnetic energy release models based on anti-parallel merging. Improvements are possible, in "flux pile-up" models where $B_{\rm in}$ varies with η for example, but the scaling (2.35) does represent an important global limit which ultimately bounds all basic merging models, with the exception of the Petschek mechanism which we will now investigate.

2.2.2 Petschek mechanism

The basis of the Petschek reconnection mechanism (Petschek, 1964) is a small diffusion region whose length λ and width l are both much smaller than the global length scale L. What happens in this case is that slow mode shocks are set up along

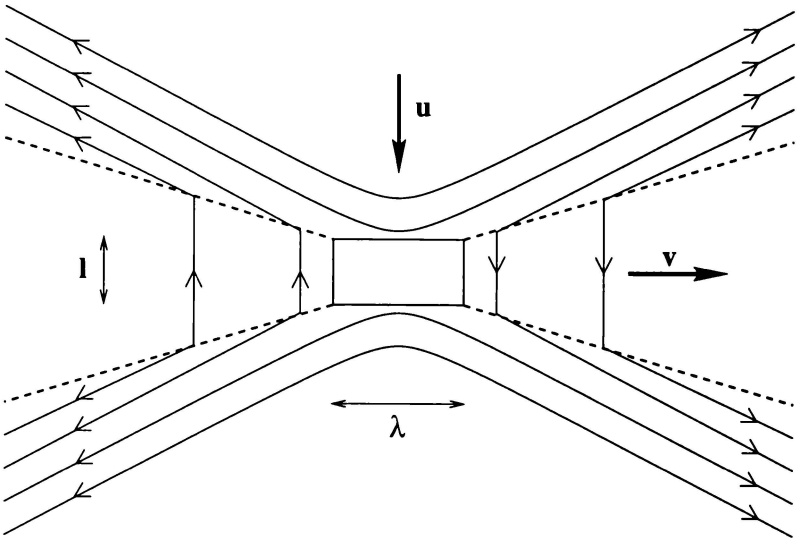

Figure 2.3: Schematic representation of the Petschek mechanism. Magnetic field reconnects at a current sheet whose dimensions decrease with resistivity, while the aspect ratio remains constant. The dashed lines represent slow mode shocks which will also accumulate current.

the "separatrices" of the corresponding global X-point (dashed lines in Figure 2.3). The advantage is that the X-point angle is large, so that flux is readily evacuated from the neutral point. This in turn helps to maintain the inflow. A schematic diagram of the Petschek process is shown in Figure 2.3.

Remember, from (2.32), that in the case of incompressible flow

$$u \sim v_A \frac{l}{\lambda} , \tag{2.36}$$

since the Alfvén speed is given by $v_A = B/(4\pi\rho)^{1/2}$. So we can see that in the case $\lambda \simeq l$ we have extremely rapid reconnection, compared with that of a long thin current sheet where

$$u \sim v_A \eta^{1/2} .$$

The critical question seems to be: what is the sheet length λ? Petschek's point was that there is no kinematic limit on the size of λ. However the inflow can only reach the Alfvénic outflow level in the limiting case of a symmetric global X-point structure, in which case there is tremendous tension where the strong incoming field lines are highly curved. Hence the upper limit on the actual merging rate is somewhat less than this.

By considering the external field as potential, it is possible to deduce (see for example Parker, 1979) that the inflow speed scaling will be somewhere between

$$v_A \eta^{1/2} \lesssim u \lesssim v_A \ln(\eta) . \tag{2.37}$$

Since $\ln(x)$ grows more slowly than any positive power of x, the maximum inflow rate is effectively $u \sim \eta^0$. Using this result along with conservation of magnetic flux

$$B_{\rm in} u \simeq \eta J \,, \tag{2.38}$$

implies

$$l \sim \eta \,, \tag{2.39}$$

where we have used $J \sim B_{\rm in}/l$. Equation (2.36) then implies that the volume of the diffusion region scales as η^2, which will stifle the Ohmic dissipation rate associated with the sheet. However, current will also accumulate along the shocks. Hence the total Ohmic dissipation will scale as

$$W_\eta \simeq \eta \left(\frac{B_{\rm in}}{l}\right)^2 Ll \sim \eta^0 \,. \tag{2.40}$$

By our definition given in Section 2.1.4, this model, then, describes "fast" reconnection.

Although formally correct, Petschek's assumptions about the dimensions of the diffusion region have, in recent years, cast doubt upon its validity. All numerical simulations (including all compressible and incompressible runs presented in this thesis), with the exception of a few which have very specific boundary conditions and invoke a localised enhancement of the plasma resistivity (Heyn and Semenov, 1996), give rise to "long" current sheets whose length remains approximately fixed with reductions in η. It would seem that in general current sheets generated during magnetic merging conform much more to the Sweet-Parker model than to that of Petschek.

2.2.3 Syrovatskii solution

The Syrovatskii solution (Syrovatskii, 1971) represents a magnetic merging solution which is very different from those discussed in the previous two sections. While most proposed merging mechanisms require external flows to drive anti-parallel fields together, Syrovatskii's solution in fact assumes uniform pressure and vanishing resistivity, so that all currents are either points or singular lines. As such no reconnection occurs, but insight can be gained into the formation of current sheets which will apply also in the fully resistive case.

Under these conditions the magnetic flux function ψ satisfies Laplace's equation

$$\nabla^2 \psi = 0 \,, \tag{2.41}$$

so that ψ is harmonic and complex analysis may be used. The relationship between the flux function and the magnetic field is given by (2.43). We will not enter into

the details of the analysis here, choosing instead to quote the result and point the interested reader to fuller treatments such as Biskamp (1994). The Syrovatskii solution may be written as

$$F(z) = \frac{\alpha}{2} z\sqrt{z^2 + b^2} + \frac{I}{2\pi} \ln\left(\frac{z + \sqrt{z^2 + b^2}}{b}\right) , \tag{2.42}$$

where b is the length of the current sheet, I is a measure of the total current in the sheet, and α is an arbitrary amplitude factor. This represents a branch cut where $\psi = 0$ along the y axis (see Figure 2.4). Here the flux function is given by

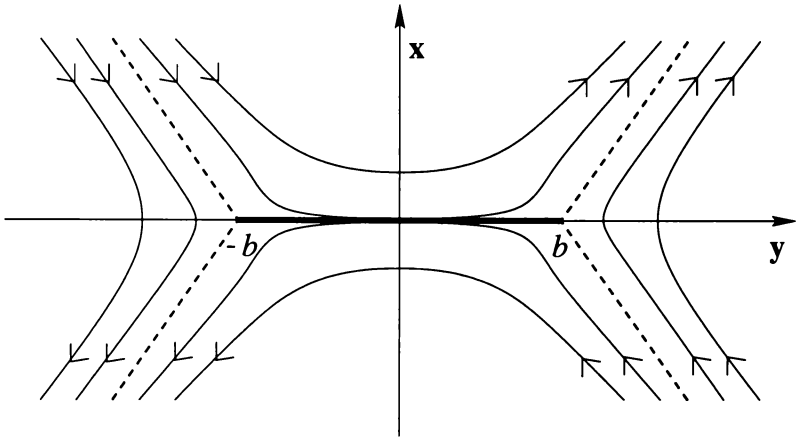

Figure 2.4: Field line structure of Syrovatskii solution. The bold line represents a branch cut current sheet, while the dashed lines are the separatrices.

$\psi = \mathrm{Re}(F(z))$. The corresponding magnetic field is given by

$$\frac{\mathrm{d}F}{\mathrm{d}z} = B_y + iB_x = \frac{1}{\sqrt{z^2 + b^2}} \left(\frac{I}{2\pi} + \alpha\frac{b^2}{2} + \alpha z^2\right) , \tag{2.43}$$

and the current will be

$$J(y) = B_y(0_+, y) - B_y(0_-, y) = \frac{2}{\sqrt{b^2 - y^2}} \left(\frac{I}{2\pi} + \alpha\frac{b^2}{2} - \alpha y^2\right) . \tag{2.44}$$

The magnetic field, however, has bad behaviour at the ends of the current sheet unless we set

$$I = \pi\alpha b^2 . \tag{2.45}$$

It should be noted that the restriction (2.45), which is required for a well behaved field, reduces the solution to that of Green (1965).

The Syrovatskii solution represents an entirely different approach to the magnetic merging problem. It uses the ideal approximation ($\eta = 0$), and does not assume an external flow profile a priori. As such care must be taken when interpreting this solution in the context of resistive merging. However, it does introduce a self-consistent analytic model for the formation of current sheets in highly conducting plasmas.

2.2.4 Sonnerup and Priest annihilation solution

In 1975 Sonnerup & Priest managed to formulate an exact solution to resistive merging which closely relates to the Sweet-Parker model. Their solution specifies a stagnation point flow coupled with a one dimensional anti-parallel magnetic field. It turns out that this solution is a special case of the more general family of solutions discussed in the next chapter and so we postpone a detailed analysis until then. For the present we will give a qualitative treatment only.

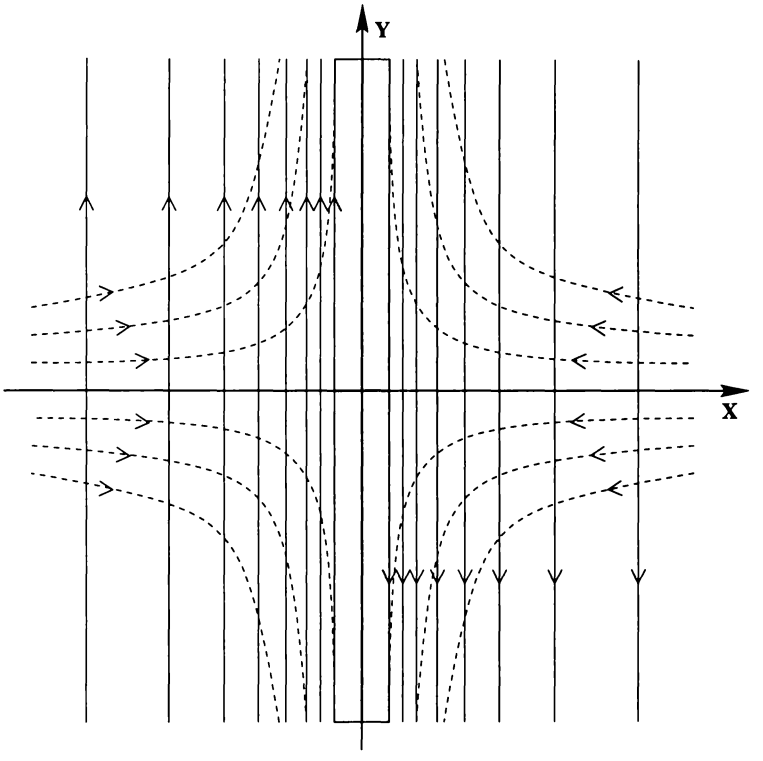

Figure 2.5: Schematic diagram of the steady-state Sonnerup and Priest solution for anti-parallel magnetic merging. Stagnation point flow (dashed lines) washes anti-parallel field lines (solid) into a current sheet (shaded) where they annihilate along a neutral line aligned to the y-axis.

Figure 2.5 shows the stagnation point flow and anti-parallel magnetic field. One important feature of this solution is that magnetic field piles up at the edge of the current sheet. The level of "flux pile-up" scales with resistivity, so that

$$B_{\text{sheet}} \sim \eta^{-1/2} .$$

Since the sheet width scales as

$$l \sim \eta^{1/2} ,$$

the Ohmic dissipation rate is given by

$$W_\eta \sim \eta \left(\frac{B_{\text{sheet}}}{l} \right)^2 \eta^{1/2} \sim \eta^{-1/2} . \tag{2.46}$$

By the definition of Section 2.1.4 this solution is a "fast" dissipater of energy.

The beauty of this solution is its simplicity. However it has two main drawbacks. Firstly, since the field is strictly 1-D, the solution describes magnetic annihilation rather than reconnection. The second drawback, in common with the solutions of the next chapter, is the unphysically high build-up of magnetic field (and hence pressure) at the edge of the current sheet. The second effect means that although the solution is formally "fast", it is physically incomplete. Care must therefore be taken when interpreting the dissipation rate of flux pile-up solutions, since the limit $\eta \rightarrow 0$ is undefined (see Section 5.2).

2.3 Summary

In this chapter we have introduced the MHD equations, looked at some of their properties, and reviewed a few of the early reconnection models and solutions. The models of particular interest for the remainder of this thesis are the Sweet-Parker model of Section 2.2.1 and the Sonnerup and Priest solution of Section 2.2.4. In the next chapter we will review more recent solutions for two and three dimensional reconnection.

Chapter 3

Exact reconnection solutions in two and three dimensions

Due to their non-linear and coupled nature, the MHD equations (2.20–2.23) provide a formidable opponent in the battle for non-trivial analytic solutions. Numerically things are not much better, since the smallness of the resistivity (10^{-12} or smaller) requires impossibly high resolution. Combine this with the compressible three dimensional time-dependent nature of the problem, and a full numerical solution becomes intractable even for very modest values of resistivity. At this point we could simply switch fields, however with some simplifying assumptions and physical insight, we can come a long way to understanding magnetic energy release in coronal reconnection.

3.1 Incompressible steady-state planar MHD

By its very nature, the cutting and rejoining of distinct field lines, magnetic reconnection requires at least two dimensions. Early attempts at explaining rapid energy release from the coronal magnetic field were centered around planar X-point configurations (see Figure 1.4). Before we investigate this founding work, let us introduce the equations governing the simplest conditions under which reconnection is possible.

We begin by assuming a steady-state ($\partial/\partial t = 0$), incompressible (ρ is uniform), two-dimensional geometry. In this case the magnetic field can be written in terms of a flux function ψ and the velocity field in terms of the stream function ϕ as follows.

$$\mathbf{B} = \nabla\psi(x,y) \times \hat{\mathbf{z}}\,, \qquad \mathbf{v} = \nabla\phi(x,y) \times \hat{\mathbf{z}} \tag{3.1}$$

It should be noted that, although a flux function always exists in 2-D, a stream function is only possible when the density is uniform, since only in this case $\nabla\cdot\mathbf{v} = 0$.

We also choose to work with the curled form of the momentum equation (2.21), since under these conditions the plasma pressure does not appear explicitly in the equations.

$$\nabla \times (\mathbf{v} \cdot \nabla)\,\mathbf{v} = \nabla \times [(\nabla \times \mathbf{B}) \times \mathbf{B}] \tag{3.2}$$

Writing this in terms of the flux and stream functions we have

$$\left[\nabla^2 \phi, \phi\right] = \left[\nabla^2 \psi, \psi\right] \ . \tag{3.3}$$

Here we use the Poisson bracket notation defined by $[f, g] = f_x g_y - f_y g_x$, where subscripts denote partial derivatives.

Using the vector identity

$$\nabla \times (\nabla \times \mathbf{a}) = \nabla(\nabla \cdot \mathbf{a}) - \nabla^2 \mathbf{a}$$

and (2.23), we can write the steady-state version of the induction equation (2.22) as

$$\nabla \times (\mathbf{v} \times \mathbf{B}) = \eta \nabla \times (\nabla \times \mathbf{B}) \ . \tag{3.4}$$

Uncurling this gives

$$\nabla \chi + \mathbf{v} \times \mathbf{B} = \eta \nabla \times \mathbf{B} \ , \tag{3.5}$$

where χ is an unknown scalar function. We can now substitute for the flux and stream functions to obtain

$$E + [\phi, \psi] = \eta \nabla^2 \psi \ . \tag{3.6}$$

The first two components of (3.5) vanish, therefore we must have $\chi = \chi(z)$. This implies $E = -\partial \chi / \partial z$ is a constant, since ϕ and ψ are functions of x and y only.

3.2 Craig and Henton solution

Craig and Henton (1995) (C&H hereafter) derive an MHD solution which allows energy to be dissipated at the fast ($W_\eta \sim \eta^{-1/2}$) rate (see equation 2.27). This solution is very similar to the Sweet-Parker model described in Section 2.2.1 with magnetic field being swept into a long thin current sheet. The key to this model's "fast" energy dissipation is that in this case magnetic flux accumulates at the edge of the sheet, significantly increasing the magnetic field gradient across the sheet. This, of course, leads to higher current density and an increased dissipation rate. For this reason solutions with this property (which includes the Sonnerup and Priest solution of Section 2.2.4) are referred to as "flux pile-up" solutions.

In order to construct a solution to (3.3) and (3.6), some initial assumptions of the forms of ϕ and ψ need to be made. The assumptions of a stagnation point flow ($\phi = \alpha xy$) and anti-parallel field lines ($\psi = \psi(x)$) were first introduced by Sonnerup

and Priest (1975) (see Section 2.2.4 for a brief description). The resulting solution exhibits the "fast" $\eta^{-1/2}$ Ohmic dissipation scaling due to the build up of flux at the edge of the sheet and turns out to be a special case of the C&H solution described below. In Section 3 of their paper, C&H generalise this *annihilation* solution slightly by showing that making only the second assumption leads to three possible forms for the flow (see also earlier work by Jardine *et al.*, 1992). However, true *reconnection* solutions require forms for ϕ and ψ that do not make each of the brackets in (3.3) vanish. Craig and Henton (1995, Section 4) addresses this issue, and we now describe their reconnection solution.

3.2.1 Craig and Henton reconnection solution

We work with the magnetic and velocity fields in terms of a flux and stream function defined by (3.1), and take these to have the forms

$$\phi = f(x) + F(x,y) \ , \quad \psi = g(x) + G(x,y) \ , \tag{3.7}$$

where F and G are harmonic functions. As noted above, a true reconnection solution requires that neither bracket in the momentum equation (3.3) vanishes, and the formulation (3.7) includes non-linear contributions which prevent this. Next we note that

$$\phi = \alpha H(x,y) \ , \quad \psi = \beta H(x,y) \ , \tag{3.8}$$

with α and β constant, gives a current-free equilibrium solution which represents flow along the field lines. With this in mind let us try

$$F(x,y) = \alpha H(x,y) \ , \quad G(x,y) = \beta H(x,y) \ .$$

Assuming these forms, the momentum brackets reduce to

$$(\alpha f''' - \beta g''')H_y = 0 \ , \tag{3.9}$$

which implies

$$f(x) = \frac{\beta}{\alpha} g(x) + q(x) \ , \tag{3.10}$$

where $q(x)$ is an arbitrary quadratic function. For simplicity and elegance we will set $q(x) = 0$. C&H do consider the case where $q(x)$ does not vanish, but this simply leads to the addition of a linear field to the flow, and is of little interest.

Turning now to the induction equation (3.6) we have

$$E + \left(\frac{\alpha^2 - \beta^2}{\alpha} \right) g' H_y = \eta g'' \ . \tag{3.11}$$

Firstly we note that since the right hand side of this equation is a function of x only, we must have H_y also being a function of x only. The only harmonic function

satisfying these conditions is of the form $H \sim xy$. Let us take $H = -xy$, the reason for the negative sign becoming apparent later. Equation (3.11) then reduces to

$$g'' + \left(\frac{\alpha^2 - \beta^2}{\eta\alpha}\right) xg' = \frac{E}{\eta} \,. \tag{3.12}$$

We solve this using the integrating factor

$$U(x) = \exp\left(\mu^2 x^2\right) \,, \quad \text{where} \quad \mu^2 = \frac{\alpha^2 - \beta^2}{2\eta\alpha} \,. \tag{3.13}$$

This gives

$$g'(x) = \frac{E}{\eta} \exp(-\mu^2 x^2) \int_0^x \exp(\mu^2 t^2) \mathrm{d}t \tag{3.14}$$

and

$$g(x) = \frac{E}{\eta} \int_0^x \exp(-\mu^2 s^2) \int_0^s \exp(\mu^2 t^2) \mathrm{d}t \mathrm{d}s \tag{3.15}$$

$$= \frac{E}{\eta} \frac{x^2}{2} \, {}_2\mathrm{F}_2 \left(1, 1, \frac{3}{2}, 2, -\mu^2 x^2\right) \,, \tag{3.16}$$

where ${}_2\mathrm{F}_2$ is a hypergeometric function (Spanier and Oldham, 1987). Hence the solution is

$$\phi(x, y) = -\alpha xy + \frac{\beta}{\alpha} g(x) \,, \quad \psi(x, y) = -\beta xy + g(x) \,. \tag{3.17}$$

In terms of the magnetic and velocity fields it is convenient to introduce the Dawson function (Spanier and Oldham, 1987), defined as follows

$$\mathrm{daw}(x) = \int_0^x \exp(t^2 - x^2) \mathrm{d}t \,. \tag{3.18}$$

We can then write the solution as

$$\mathbf{v} = \left(-\alpha x, \alpha y + \frac{\beta}{\alpha} \frac{E}{\eta\mu} \mathrm{daw}(\mu x)\right) \tag{3.19}$$

$$\mathbf{B} = \left(-\beta x, \beta y + \frac{E}{\eta\mu} \mathrm{daw}(\mu x)\right) \,. \tag{3.20}$$

Clearly we must take $0 \leq \beta < \alpha$ so that $\mu^2 > 0$ and the solution describes fluid washing flux into a current sheet aligned with the y-axis.

Figure 3.1 shows a typical field and flow configuration. The sheared stagnation point flow is evident in the left plot, while the plot on the right clearly shows the X-point nature of the magnetic field.

3.2.2 Interpretation of the Craig and Henton solution

The basis of the above solution is a stagnation point flow superposed with a one dimensional magnetic field. However, the parameter β mixes these two fields together so that there is always some mutual alignment. Indeed as $\beta \to \alpha$ the two

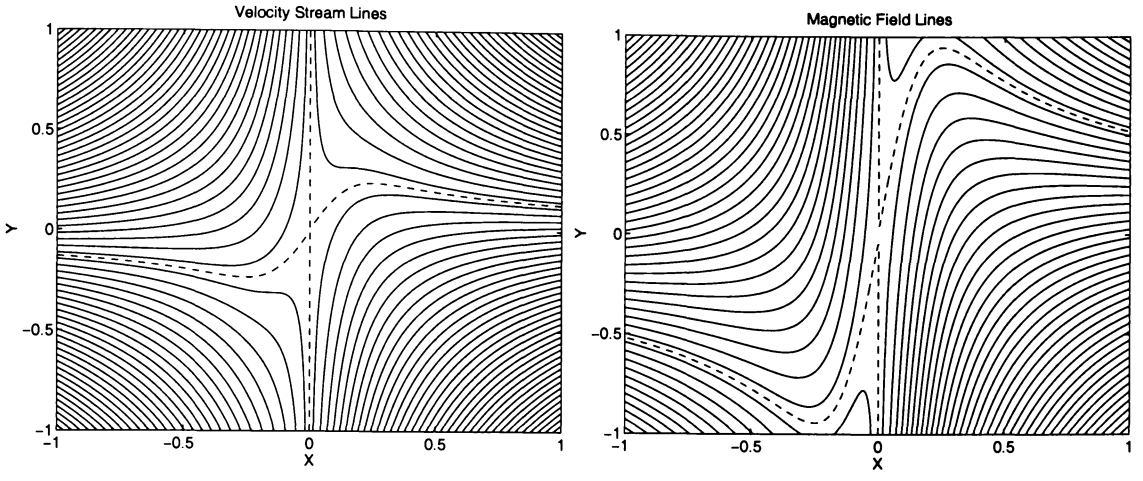

Figure 3.1: Velocity stream lines and magnetic field lines for the Craig and Henton solution (3.19) and (3.20). Dashed lines represent the separatrices (field lines which thread the null). Here we have used $\alpha = 1$, $\beta = 0.5$, $\eta = 0.01$ *and* $E = 0.07$.

fields become the same. It is the mutual alignment which allows magnetic flux to be advected across one of the magnetic separatrices, as required for reconnection. The special case $\beta = 0$ corresponds to the solution of Sonnerup and Priest (1975), but represents only anti-parallel annihilation since both magnetic separatrices coincide (see also Section 2.2.4).

The width of the current layer is characterised by the distance to the peak magnetic field component aligned with the sheet. Looking at equation (3.12) dimensionally, we see that we must have a small length scale across the sheet

$$l \sim \eta^{1/2} . \tag{3.21}$$

Now since daw(x) increases linearly for small x, from (3.20) the peak field being washed into the sheet must scale as

$$B_{\max} \sim \eta^{-1/2} , \tag{3.22}$$

with the corresponding maximum current

$$J_{\max} \sim \eta^{-1} . \tag{3.23}$$

The Ohmic dissipation rate (2.27) can then be obtained

$$W_\eta \simeq \eta J^2 \mathrm{d}V \sim \eta J^2 l \sim \eta^{-1/2} . \tag{3.24}$$

Figure 3.2 illustrates the pivotal role played by η in "piling-up" magnetic field at the edge of the sheet, with the current escalating in sympathy due to the increased field gradient. The scalings (3.21), (3.22) and (3.23) are also apparent.

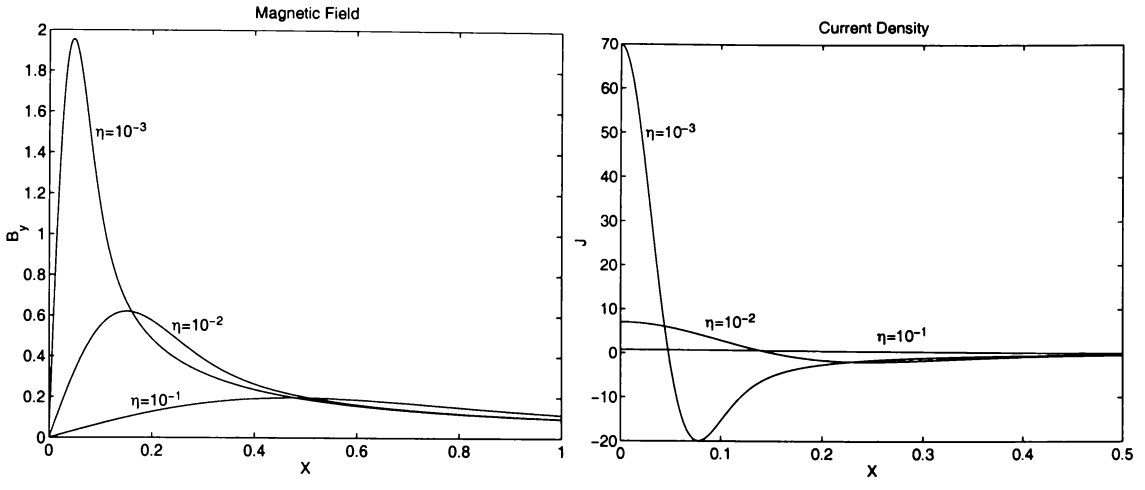

Figure 3.2: Magnetic field and current density through a slice along the x-axis for $\eta = 0.1$, 0.01 and 0.001, with other parameters the same as in Figure 3.1.

3.3 Solutions in three dimensions

Lau and Finn (1990) introduce the idea of kinematic reconnection and use this to predict various forms of reconnection at three dimensional magnetic neutral points (see also Greene, 1988). The eigenstructure of a three dimensional null is of key importance in any reconnection model and can be obtained by considering the Taylor expansion

$$\mathbf{B}(\mathbf{x}) = M\mathbf{x}\,, \tag{3.25}$$

where M is the 3×3 matrix given by $\partial B_i/\partial x_j$. Since $\nabla \cdot \mathbf{B} = 0$ the trace of this matrix vanishes, which in turn implies that the eigenvalues sum to zero. Hence the real components of three eigenvalues will not all be of the same sign. Many eigenstructures are possible (see Lau and Finn, 1990). Of central interest, however, is the case of a force-free equilibrium where the eigenvalues are all real. In this case the current must also vanish, and the eigenstructure can be summarised by Figure 3.3, with a possible reversal of fields. We follow the nomenclature of Priest and Titov (1996) and refer to the plane generated by the vectors corresponding to the eigenvalues of like sign as the "fan" surface, with the remaining eigenvector defining the "spine" curve.

3.3.1 General superposition

The momentum and induction equations in the case of steady-state incompressible MHD can be written in the form:

$$(\mathbf{v}\cdot\nabla)\,\boldsymbol{\omega} - (\boldsymbol{\omega}\cdot\nabla)\,\mathbf{v} = (\mathbf{B}\cdot\nabla)\,\mathbf{J} - (\mathbf{J}\cdot\nabla)\,\mathbf{B} \tag{3.26}$$

$$(\mathbf{v}\cdot\nabla)\,\mathbf{B} = (\mathbf{B}\cdot\nabla)\,\mathbf{v} + \eta\nabla^2\mathbf{B}\,, \tag{3.27}$$

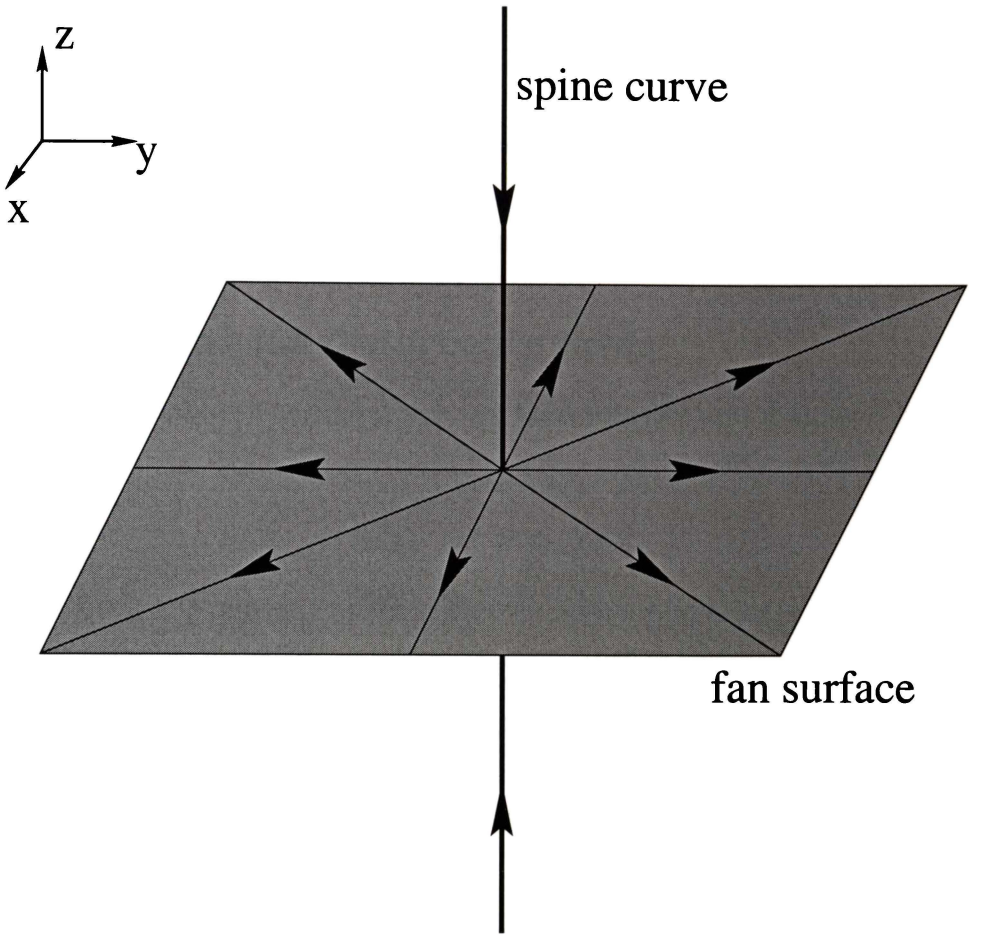

Figure 3.3: Eigenstructure of three dimensional magnetic null point.

where

$$\boldsymbol{\omega} = \nabla \times \mathbf{v} \quad , \quad \mathbf{J} = \nabla \times \mathbf{B}$$

and of course

$$\nabla \cdot \mathbf{v} = 0 \quad , \quad \nabla \cdot \mathbf{B} = 0 \, .$$

The symmetry between the velocity and magnetic field is clear. It is in fact only the resistive term which disallows the trivial $\mathbf{v} = \lambda \mathbf{B}$ solution in the general case of $\nabla^2 \mathbf{B} \neq 0$. Remembering that η is very small, this suggests that the velocity and magnetic fields run almost parallel except in regions of high current.

An important observation to make about the Craig and Henton solution (3.19, 3.20) presented in the previous section is that the velocity and magnetic fields can be written in terms of a superposition of the following form.

$$\begin{aligned} \mathbf{v} &= \alpha \mathbf{v}_a + \frac{\beta}{\alpha} \mathbf{B}_a \\ \mathbf{B} &= \beta \mathbf{v}_a + \mathbf{B}_a \, . \end{aligned}$$

Here

$$\mathbf{v}_a = (-x, y) \quad \text{and} \quad \mathbf{B}_a = \frac{E}{\eta\mu}\text{daw}(\mu y) \tag{3.28}$$

is the annihilation solution of Sonnerup and Priest (1975) (see also Section 2.2.4).

We will now construct the exact three dimensional reconnection solutions first derived by Craig *et al.* (1995) and Craig and Fabling (1996).

3.3.2 Spine and fan disturbance fields

Motivated by the above considerations, we take velocity and magnetic fields of the form

$$\mathbf{v}(\mathbf{x}) = \mathbf{P} + \lambda\mathbf{Q} \tag{3.29}$$

$$\mathbf{B}(\mathbf{x}) = \lambda\mathbf{P} + \mathbf{Q}\,. \tag{3.30}$$

Here we have superposed a background potential field $\mathbf{P}$ with a disturbance field $\mathbf{Q}$.

Let us use the simplest potential field of interest, by taking

$$\mathbf{P} = \alpha\,[\kappa x, (1-\kappa)y, -z]\ , \qquad 0 \le \kappa \le 1\,. \tag{3.31}$$

This form is of course consistent with the planar analysis of Section 3.2.1, where we had to take $H = \alpha xy$. It is easy to spot that linearising about the null at the origin will simply give an eigenstructure similar to that in Figure 3.3. In other words $z = 0$ is the fan plane, while the spine lies along the z-axis. Our next task is to find a form for $\mathbf{Q}$ which will complement this choice of background field.

Rewriting (3.26) as

$$\nabla\times(\boldsymbol{\omega}\times\mathbf{v}) = \nabla\times(\mathbf{J}\times\mathbf{B})$$

and substituting for $\mathbf{P}$ and $\mathbf{Q}$, we find the following condition on $\mathbf{Q}$.

$$(\lambda^2 - 1)\nabla\times[(\nabla\times\mathbf{Q})\times\mathbf{Q}] = \mathbf{0} \tag{3.32}$$

Clearly the $\lambda = \pm 1$ solution is of little interest as the induction equation then implies a current free solution with flow only along field lines. For $\lambda^2 \neq 1$ this condition may be rewritten as

$$\nabla\times\left[(\mathbf{Q}\cdot\nabla)\mathbf{Q} - \nabla(\tfrac{1}{2}Q^2)\right] = \mathbf{0}\,,$$

and so

$$(\mathbf{Q}\cdot\nabla)\,\mathbf{Q} = \nabla\left(\frac{1}{2}Q^2 + \chi\right)\,. \tag{3.33}$$

Here $\chi = \chi(\mathbf{x})$ is an arbitrary scalar function of position. Let us take $\chi = -\frac{1}{2}Q^2$, so that we have

$$(\mathbf{Q}\cdot\nabla)\,\mathbf{Q} = \mathbf{0}\,. \tag{3.34}$$

This condition can be satisfied by taking either the one variable two component "fan" form

$$\mathbf{Q}_F(z) = X(z)\hat{\mathbf{x}} + Y(z)\hat{\mathbf{y}} \,, \tag{3.35}$$

or the two variable one component "spine" form

$$\mathbf{Q}_S(x,y) = Z(x,y)\hat{\mathbf{z}} \,. \tag{3.36}$$

The terms "spine" and "fan" relate to the locations of current accumulation of the associated solution as mentioned in Section 3.3 and depicted in Figure 3.3.

3.3.3 Current structures generated by $\mathbf{Q}_F$ and $\mathbf{Q}_S$

To find the locations of current accumulation in a resistive solution it is instructive to look at the limit $\eta \to 0$. Since the sheet width decreases with η and current intensity increases as η is reduced, it follows that in the limit of zero resistivity current singularities will form. Hence a solution of the ideal ($\eta = 0$) induction equation will have singularities in regions where finite resistivity would generate large currents. In other words we solve

$$\nabla \times (\mathbf{v} \times \mathbf{B}) = \mathbf{0} \,,$$

which, on substituting for $\mathbf{P}$ and $\mathbf{Q}$, becomes

$$(1 - \lambda^2)\nabla \times (\mathbf{P} \times \mathbf{Q}) = \mathbf{0} \,. \tag{3.37}$$

Substituting the fan form $\mathbf{Q}_F = X(z)\hat{\mathbf{x}} + Y(z)\hat{\mathbf{y}}$ into the induction equation (with $\eta = 0$) gives

$$(\kappa X + zX' \,,\; (1-\kappa)Y + zY' \,,\; 0) = \mathbf{0} \,.$$

Solving for each component respectively gives

$$\begin{aligned} X(z) &= Az^{-\kappa} \\ Y(z) &= Az^{\kappa-1} \,. \end{aligned}$$

This disturbance field clearly becomes singular in the $z = 0$ plane (since $0 \leq \kappa \leq 1$ from (3.31)), and hence in the fully resistive case drives currents in the fan surface.

In the case of the spine form $\mathbf{Q}_S = Z(x,y)\hat{\mathbf{z}}$ it is simplest to think in terms of a cylindrical disturbance mode. Specifying a symmetric background field by setting $\kappa = 1/2$ in (3.31), we transform to polar coordinates by taking

$$\begin{aligned} Z(x,y) \to Z(r,\theta) &= f(r)\mathrm{e}^{im\theta} \\ \mathbf{P}(x,y,z) \to \mathbf{P}(r,\theta,z) &= \alpha(\frac{r}{2}, 0, -z) \,, \end{aligned} \tag{3.38}$$

where $r^2 = x^2 + y^2$, $\tan(\theta) = y/x$ and m represents the angular mode number of the disturbance. The ideal ($\eta = 0$) induction equation for a cylindrically symmetric spine disturbance then becomes

$$f + \frac{1}{2} r f' = 0 \tag{3.39}$$

(see (3.63) for the fully time-dependent, resistive, cylindrical induction equation). Solving this gives

$$f(r) = A r^{-2} .$$

Clearly Z is singular along the line $r = 0$, and so this type of perturbation drives currents in a narrow tube aligned to the spine.

3.3.4 Spine and fan solutions

Having established the general forms for spine and fan reconnection in terms of the disturbance fields $\mathbf{Q}_S$ and $\mathbf{Q}_F$, we will now state these as solutions of the induction equation, following the analysis of Craig *et al.* (1997). The induction equation, in terms of our background field $\mathbf{P}$ and disturbance field $\mathbf{Q}$, can be written as

$$-(1 - \lambda^2)\nabla \times (\mathbf{P} \times \mathbf{Q}) = \eta \nabla^2 \mathbf{Q} . \tag{3.40}$$

Taking the fan disturbance field $\mathbf{Q}_F = X(z)\hat{\mathbf{x}} + Y(z)\hat{\mathbf{y}}$, the x and y components of the induction equation become

$$\begin{aligned} \bar{\eta} X'' + z X' + \kappa X &= 0 \\ \bar{\eta} Y'' + z Y' + (1 - \kappa) Y &= 0 , \end{aligned}$$

where

$$\bar{\eta} = \frac{\eta}{\alpha(1 - \lambda^2)} . \tag{3.41}$$

The solution is then

$$X(z) = C_1 \frac{z}{\bar{\eta}^{1/2}} \, \mathrm{M}\left(\frac{\kappa + 1}{2}, \frac{3}{2}, -\frac{z^2}{2\bar{\eta}} \right) + C_2 \, \mathrm{M}\left(\frac{\kappa}{2}, \frac{1}{2}, -\frac{z^2}{2\bar{\eta}} \right) , \tag{3.42}$$

where $\mathrm{M}(a, b, x)$ is a Kummer function (Spanier and Oldham, 1987). Clearly the solution for $Y(z)$ is obtained by simply replacing κ with $(1 - \kappa)$ in the above closed form expression. We can now determine the choice of C_1 and C_2 by considering the asymptotic properties of the Kummer function. These are

$$\mathrm{M}(a, b, x) \sim \begin{cases} 1 + ax/b , & \text{as } x \to 0 , \\ |x|^{-a} & \text{as } x \to -\infty . \end{cases} \tag{3.43}$$

Since we are interested in neutral point merging we discard the even solution by setting $C_2 = 0$. Specifying $Y(1) = 1$ implies $C_1 = 2^{-(\kappa+1)/2} \bar{\eta}^{-\kappa/2}$.

The spine solution is somewhat more difficult to interpret. Following Craig *et al.* (1997), we define a symmetric background field by taking $\kappa = 1/2$ which allows a cylindrical mode decomposition of the disturbance field in planes of constant z, similar to the spine analysis of the previous section. Making the transformation to cylindrical coordinates using (3.38) the induction equation for a cylindrically symmetric spine disturbance becomes

$$f + \frac{1}{2} r f' = \bar{\eta} \left(f'' + \frac{f'}{r} - \frac{m^2}{r^2} f \right) , \tag{3.44}$$

where $\bar{\eta}$ is defined by (3.41). The Kummer function solution to this is

$$f(r) = C \left(\frac{r^2}{|4\bar{\eta}|} \right)^{m/2} \mathrm{M} \left(1 + \frac{1}{2} m, 1 + m, -\frac{r^2}{|4\bar{\eta}|} \right) , \tag{3.45}$$

where C is a constant. Note that we have had to change the sign of α to have inflow over the fan surface and outflow along the spine, to obtain a meaningful spine solution. Under these conditions $\bar{\eta} < 0$, and we have used the modulus of this to make the solution more transparent. Other than for the pathological $m = 0$ mode, $f(r) \sim r^{-2}$ in the far field. Normalising the field to unity using the asymptotic properties (3.43) at the boundary implies $C = \dfrac{1}{4\bar{\eta}}$.

3.3.5 Reconnection scalings of 3-D solutions

As with the planar solutions, we can derive expressions for how various fundamental quantities scale with respect to the resistivity η. This is useful, as it gives an indication of what will happen to the reconnection process as η is reduced. We could simply use the asymptotics (3.43) of the closed form solutions (3.42, 3.45) as we did when we obtained the 2-D scalings of Section 3.2.2. However, it is perhaps more insightful to look at solutions to the induction equation within the diffusion region and match these to solutions in the far field.

Let us substitute the fan formulation (3.35) into the induction equation. We then have

$$-\alpha(1 - \lambda^2) \left[\kappa X + z X' ,\ (1 - \kappa) Y + z Y' ,\ 0 \right] = \eta (X'', Y'', 0) . \tag{3.46}$$

Both x and y components are the same dimensionally and imply the small length scale $\Delta z \simeq \eta^{1/2}$. Another way to see this is to make the substitution $\bar{z} = z/\sqrt{\eta}$. The equation for $\bar{z}$ is then independent of η, indicating the presence of a small length scale $\Delta z \simeq \sqrt{\eta}$. If we identify the region $z < \Delta z$ as a resistive current layer, consistent with the ideal analysis of the previous section, we can deduce resistive scaling laws based on a simple boundary layer treatment of the induction equation.

Looking at the components, we see that well outside the boundary layer ($z \gg \Delta z$)

$$\kappa X_o + z X_o' \simeq 0 \quad , \quad (1-\kappa) Y_o + z Y_o' \simeq 0 \, ,$$

and so

$$X_o \simeq z^{-\kappa} \quad , \quad Y_o \simeq z^{\kappa - 1}$$

on taking the normalisation $X(1) = Y(1) = 1$. Appropriate inner solutions are simply $X_i \simeq C_1 z$ and $Y_i \simeq C_2 z$, consistent with taking the leading order term in a Taylor series expansion. Next we match the inner and outer solutions so that they coincide at the edge of the boundary layer where $z = \eta^{1/2}$. This allows us to determine the constants C_1 and C_2, so that the inner solutions will be given by

$$X_i \simeq \eta^{\frac{-1-\kappa}{2}} z \quad , \quad Y_i \simeq \eta^{\frac{\kappa}{2}-1} z \, .$$

Hence the peak fields (at $z = \eta^{1/2}$) scale with η in the following way

$$X_{\max} \sim \eta^{-\kappa/2} \quad , \quad Y_{\max} \sim \eta^{(\kappa-1)/2} \, . \tag{3.47}$$

The current, given by $\mathbf{J} = (J_x, J_y, J_z) = (-Y', X', 0)$, will scale as

$$J_x \sim \eta^{(\kappa-2)/2} \quad , \quad J_y \sim \eta^{-(\kappa+1)/2} \, . \tag{3.48}$$

The corresponding Ohmic dissipation rate (2.27) will be given by

$$W_\eta \sim \eta (J_x^2 + J_y^2) \Delta z \sim \eta^{-\frac{|1-2\kappa|}{2}} \qquad (0 \leq \kappa \leq 1) \, . \tag{3.49}$$

Hence the dominant dissipation term will always give rise to "fast" reconnection (see Section 2.1.4), with the limiting case being the symmetric $\kappa = 1/2$ fan, for which dissipation is invariant with respect to resistivity (still fast). It is interesting that the fastest rate is when $\kappa = 0$ or 1. This corresponds to a strictly two dimensional background field (3.31), so that the Dawson function scalings of Section 3.2.2 are recovered.

In the case of spine reconnection we specify the disturbance $Z(x,y)\hat{\mathbf{z}}$. To analyse the associated scaling properties it is simplest to work in polar coordinates as we did in the previous section (see equation (3.38)). Substituting $Z(r,\theta) = f(r) e^{im\theta}$ into the cylindrical coordinate induction equation (3.44) gives us the following far field behaviour

$$f_o + \frac{r}{2} f_o' = 0 \, ,$$

on setting $\eta = 0$. This provides an outer solution

$$f_o \simeq r^{-2}$$

on normalising $Z(1) = 1$ as we did for the fan analysis. The inner solution is again simply the first term of the local Taylor expansion $f_i \simeq Cr$, where C is a constant.

Matching this, as we did for the fan disturbance above, to the outer solution at the familiar boundary layer edge $r = \eta^{1/2}$, leads to the following scalings of Craig and Fabling (1996)

$$Z \sim \eta^{-1} \quad , \quad J \sim \eta^{-3/2} \, . \tag{3.50}$$

It is clear that the current scales more favourably in the case of spine reconnection than for fan reconnection. However, the dissipation is now limited to the cylindrical volume $\mathrm{d}V = \pi r^2 L \simeq \pi \eta L$, so that the Ohmic dissipation rate for the symmetric spine scales as

$$W_\eta \simeq \eta J^2 \mathrm{d}V \sim \eta^{-1} \, . \tag{3.51}$$

Despite the more favourable η scaling, due to the dissipation volumes involved we expect fan reconnection to release far more energy at coronal resistivity values (see Craig *et al.* (1997) for power output calculations).

3.3.6 Planar reconnection solutions

The two dimensional solution of Section 3.2 and the three dimensional solutions of this section are not distinct. The 3-D solutions in fact encapsulate the 2-D solutions in a natural way. We already saw some evidence of this when we looked at the Ohmic dissipation rate for a fan disturbance. We will now show that both spine and fan solutions can be reduced to two dimensions to yield the earlier 2-D solutions.

Substituting the spine formulation $\mathbf{Q}_S = Z(x,y)\hat{\mathbf{z}}$ into the induction equation (3.40), we find that the first two components vanish, while the third component gives

$$\alpha(1-\lambda^2)[Z + \kappa x Z_x + (1-\kappa) y Z_y] = \eta \nabla^2 Z \, . \tag{3.52}$$

If we now take $\kappa = 1$ and y as the ignorable coordinate we have on integrating once

$$E + \alpha(1-\lambda^2) x Z = \eta Z' \, , \tag{3.53}$$

where E is a constant of integration. In this case we must take $\alpha < 0$ so that the flow drives anti-parallel field into a sheet aligned to the z axis. Equation (3.53) is then equivalent to equation (3.11) with $g'(x) = Z(x)$ and will hence lead to the planar solution (3.19, 3.20). Clearly taking $\kappa = 0$ will provide the same result, this time with x as the ignorable coordinate.

Substituting the fan formulation $\mathbf{Q}_F = X(z)\hat{\mathbf{x}} + Y(z)\hat{\mathbf{y}}$ into (3.40) and again taking $\kappa = 1$ leads to

$$\alpha(1-\lambda^2)[-X - zX', zY', 0] = \eta[X'', Y'', 0] \, , \tag{3.54}$$

where y is the ignorable coordinate. A single integration of the x component again provides us with the same condition as (3.11) with $g'(x) \to X(z)$ and the corresponding Dawson function solution, though this time we require $\alpha > 0$. However,

there is now some added freedom in terms of a function in the ignorable direction. Integrating the second component twice yields a solution for $Y(z)$ in terms of the error function defined as

$$\mathrm{erf}(x) = \frac{2}{\sqrt{\pi}} \int_0^x \exp(-t^2)\mathrm{d}t \ . \tag{3.55}$$

Hence our solution for Y becomes

$$Y(z) = Y(0) + Y'(0)\frac{\sqrt{\pi}}{2\mu}\mathrm{erf}(\mu z) \ , \tag{3.56}$$

where

$$\mu^2 = \frac{\alpha(1-\lambda^2)}{2\eta}$$

is the same as in (3.13) since $\lambda = \alpha/\beta$. The most general form of planar solution with an ignorable coordinate is

$$\mathbf{v} = \mathbf{P} + \lambda\mathbf{Q} \ , \quad \mathbf{B} = \mathbf{Q} + \lambda\mathbf{P} \ ,$$

with

$$\mathbf{P} = \alpha[-x, y, 0] \tag{3.57}$$

$$\mathbf{Q} = [0, \frac{E}{\eta\mu}\mathrm{daw}(\mu x), Z(0) + Z'(0)\frac{\sqrt{\pi}}{2\mu}\mathrm{erf}(\mu x)] \ , \tag{3.58}$$

where we have transformed to coordinates in the xy plane with z as the ignorable direction for direct comparison with (3.19, 3.20).

It is important to note that the error function component of the solution does not lead to fast reconnection. This is because the resulting field is perpendicular to the direction of the flow, and as such it is not stretched (intensified) during the merging process. The error function solution in fact represents slow magnetic annihilation similar to Sweet-Parker (see Section 2.2.1).

3.3.7 Separator reconnection

We have discussed the two primary forms of reconnection, namely spine and fan, based on the eigenstructure of a three dimensional null point. Although we generally associate reconnection with neutral points of the magnetic field, reconnection is possible in regions where the magnetic field does not vanish anywhere. A clear example of this is the solution given by (3.57) and (3.58), in the case $Z(x) =$ constant $\neq 0$.

Kinematic considerations (see for example Lau and Finn (1990)) predict "separator" reconnection to occur at the intersection of two fan surfaces. Figure 3.4 summarises this geometry. Separator reconnection, then, represents an extension of

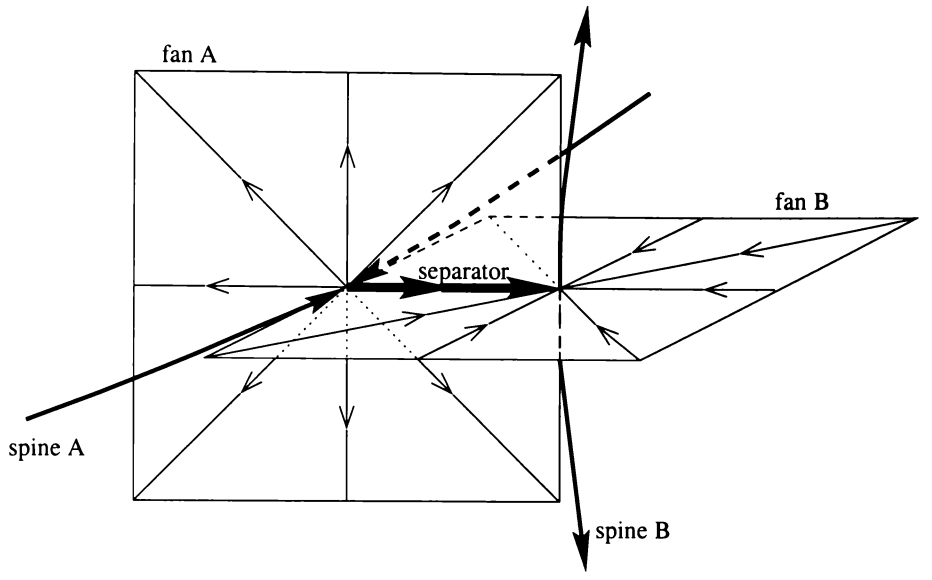

Figure 3.4: Schematic diagram showing a separator line at the intersection of two fan planes.

the planar model which incorporates magnetic field in the ignorable direction, so that the planar separatrices become fan planes which intersect along the ignorable axis to generate a separator line.

More complicated separator solutions than the above example are possible. We postpone a detailed analysis of separator solutions until Chapter 6, where the presence of multiple nulls allows us to produce lines which are the intersection of two fan planes.

3.4 Time-dependent collapse

All the analytic work we have covered so far deals with strictly steady-state situations. However, as Craig and McClymont (1999) show, scaling laws for time-dependent magnetic merging can be deduced by considering the dynamics of a magnetic wave with a global profile during the merging process. Craig and Watson (1999) derive time-dependent effects for exact planar reconnection solutions, incorporating also a finite viscosity. In this section we will attempt to illustrate these effects using a less sophisticated 1-D approach. As one might expect, the bulk scaling features turn out to be the same.

The time-dependent induction equation in the case of a 1-D fan disturbance $\mathbf{Q}_F = Y(z)\hat{\mathbf{y}}$ is

$$\dot{Y} - \alpha(1-\lambda^2)(1-\kappa)Y - \alpha(1-\lambda^2)zY' = \eta Y'' \,, \tag{3.59}$$

where the dot refers to $\partial/\partial t$ and dash is $\partial/\partial z$. Let us now assume that the magnetic

disturbance is initially a smooth global profile. Then in the outer field, where the resistive term is approximately zero, we have

$$\dot{Y} - \bar{\alpha} z Y' = \bar{\alpha}(1-\kappa) Y \ ,$$

where $\bar{\alpha} = \alpha(1-\lambda^2)$. Using the method of characteristics this gives

$$\frac{\mathrm{d}t}{1} = \frac{\mathrm{d}z}{-\bar{\alpha} z} = \frac{\mathrm{d}Y}{\bar{\alpha}(1-\kappa)Y} \ .$$

Integrating these leads to

$$\xi_1 = z e^{\bar{\alpha} z t} \quad , \quad \xi_2 = Y e^{-\bar{\alpha}(1-\kappa)t} \tag{3.60}$$

with the initial condition $Y(t=0) = Y_0(z)$, so that the solution becomes

$$Y(z,t) = Y_0\left(z e^{\bar{\alpha} t}\right) e^{\bar{\alpha}(1-\kappa)t} \ . \tag{3.61}$$

This represents an inward traveling magnetic pulse that increases in amplitude over time. When the pulse approaches the neutral point, the resistive term in equation (3.59) becomes comparable to the terms on the left hand side, so that we have

$$\begin{aligned} Y_0' z e^{\bar{\alpha} t} \bar{\alpha} e^{\bar{\alpha}(1-\kappa)t} + Y_0 \bar{\alpha}(1-\kappa) e^{\bar{\alpha}(1-\kappa)t} - \bar{\alpha}(1-\kappa) Y_0 e^{\bar{\alpha}(1-\kappa)t} - \bar{\alpha} z Y_0' e^{\bar{\alpha} t} e^{\bar{\alpha}(1-\kappa)t} \\ \simeq \ \eta Y_0'' e^{2\bar{\alpha} t} e^{\bar{\alpha}(1-\kappa)t} \ . \end{aligned}$$

Since Y_0 is a smooth global function, we expect it's derivatives to be comparable. In other words $Y_0' \simeq Y_0/L \simeq Y_0$, since $L = 1$ is the global length scale. Using this, and the fact that $z e^{\bar{\alpha} t}$ is constant on a given characteristic ξ_1, we see that

$$\bar{\alpha} \ \simeq \ \eta e^{2\bar{\alpha} t} \ .$$

In other words, we expect the time for a global magnetic field structure to collapse to a small length-scale *fan* current sheet to depend on resistivity in the following way.

$$t_f \ \simeq \ -\frac{1}{2\bar{\alpha}} \ln(\eta) \tag{3.62}$$

In the case of a spine disturbance $\mathbf{Q}_S = Z(x,y)\hat{\mathbf{z}}$ the argument is similar. Let us again adopt the cylindrical formulation (3.38) for the symmetric flow profile $\kappa = 1/2$. The corresponding induction equation is

$$\dot{f} + \bar{\alpha} f + \bar{\alpha} \frac{r}{2} f' = \eta \left(f'' + \frac{f'}{r} - \frac{m^2}{r^2} f \right) \ , \tag{3.63}$$

where we have again used $\bar{\alpha} = \alpha(1-\lambda^2)$. Remembering that in the case of spine reconnection we need to reverse the flow by taking $\alpha < 0$, we will take $\bar{\alpha} = -|\bar{\alpha}|$.

Away from the neutral point, where the resistive term is approximately zero, we then have the characteristic quotients

$$\frac{\mathrm{d}t}{1} = \frac{\mathrm{d}r}{-|\bar{\alpha}|r/2} = \frac{\mathrm{d}f}{|\bar{\alpha}|f} \ .$$

Solving these as for the fan case above gives

$$f(r,t) = f_0\left(re^{|\bar{\alpha}|t/2}\right)e^{|\bar{\alpha}|t} \ , \tag{3.64}$$

where f_0 is the initial smooth global profile. Substituting (3.64) into (3.63) gives

$$f_0'\frac{r}{2}e^{|\bar{\alpha}|t/2}|\bar{\alpha}|e^{|\bar{\alpha}|t} + f_0|\bar{\alpha}|e^{|\bar{\alpha}|t} \simeq \eta\left(f_0''e^{2|\bar{\alpha}|t} + \frac{f_0'}{r}e^{3|\bar{\alpha}|t/2} - \frac{m^2 f_0}{r^2}e^{\bar{\alpha}t}\right) \ .$$

Using the same globality argument as before and recognising that $re^{|\bar{\alpha}|t/2}$ is constant on a characteristic we have

$$c_1\frac{|\bar{\alpha}|}{2} + |\bar{\alpha}| \sim \eta\left(e^{|\bar{\alpha}|t} + c_2e^{|\bar{\alpha}|t} - c_3m^2e^{|\bar{\alpha}|t}\right)$$

so that the scaling of the collapse time with η for symmetric *spine* reconnection is the following

$$t_s \sim -\frac{1}{|\bar{\alpha}|}\ln(\eta) \ . \tag{3.65}$$

It should be noted that Craig and Watson (1999) and Craig and McClymont (1999) show the existence of a time-scale associated with the shear parameter β. However for any physically interesting case, where $\alpha^2 > \beta^2$ and α has the required sign to advect flux into a current sheet, the above time scalings represent the time-scale of the dominant localisation effect.

3.5 Summary

In this chapter we have reviewed a family of solutions for magnetic reconnection in the solar corona. In particular we showed that kinematically predicted spine and fan current structures have natural analytic forms. We also found that the 3-D solutions encapsulate the earlier 2-D reconnection solution of Craig and Henton (1995), which in turn encapsulates the Sonnerup and Priest (1975) solution. It is interesting to note that Galloway and Zheligovsky (1994) obtained the exact spine solution to the induction equation from kinematic considerations in a dynamo theory context. Unfortunately they did not realise that it also represents a solution of the momentum equation!

All the solutions reviewed here exhibit Ohmic dissipation rates which scale independently of any positive power of η, making them formally "fast". The way these solutions overcome the slow Sweet-Parker scaling is "flux pile-up". By this we mean

that the magnetic field at the edge of the current sheet scales as a negative power of η. As such these solutions are physically incomplete — the pressure associated with the pile-up field must be bounded by external conditions. Saturation of the pile-up field and it's effects on current sheet properties will be covered in detail in Section 5.2.

It might seem that the exact three dimensional solutions of this chapter put an end to reconnection research. However, though enlightening, these in no way represent all possible solutions. In the next chapter we will investigate reconnection in a numerical context to verify whether the analytic solutions reviewed here manifest time-dependently under general merging conditions.

Chapter 4

Reconnection simulations in two and three dimensions

In the previous chapter we presented the main existing reconnection models and solutions. Of particular interest are the exact three dimensional solutions discussed in Section 3.3, since these degenerate naturally to encompass the planar reconnection solutions of Craig and Henton (1995) and the earlier annihilation solution of Sonnerup and Priest (1975). However, all the analytic solutions presented are merely steady-state approximations, and it is important to test whether the features such models predict manifest themselves in time-dependent calculations from reasonably general initial conditions.

In the past analytic and numerical works have tended to follow two independent paths. Numerical work, in particular, can yield unexpected, and even contradictory results simply by choosing inappropriate boundary conditions. It is in fact the boundary conditions which represent the main source of confusion when comparing analytic and numerical results, since the analytic models often have no intrinsic boundaries while numerical solutions cannot exist without them. For this reason we choose to use periodic boundary conditions in most of our numerical simulations, since what happens on the boundary is a function of what the internal solution is doing rather than being an arbitrary external condition. Both inflow and outflow can occur across such boundaries, and a periodic region in a sense tessellates an infinite domain.

The system of equations we solve numerically is the following:

$$\frac{\partial \mathbf{v}}{\partial t} = \mathbf{J} \times \mathbf{B} - \boldsymbol{\omega} \times \mathbf{v} - \nabla p + \nu \nabla^2 \mathbf{v}, \tag{4.1}$$

$$\frac{\partial \mathbf{B}}{\partial t} = \nabla \times (\mathbf{v} \times \mathbf{B}) + \eta \nabla^2 \mathbf{B}, \tag{4.2}$$

$$\nabla \cdot \mathbf{B} = \nabla \cdot \mathbf{v} = 0, \tag{4.3}$$

where $\mathbf{J} = \nabla \times \mathbf{B}$ is the current density and $\boldsymbol{\omega} = \nabla \times \mathbf{v}$ represents the vorticity. These

describe the time-dependent evolution of an incompressible plasma, and are simply a specialised reiteration of (2.20-2.23). Unlike the analytic treatments of Chapter 3, we also use kinematic viscosity ν in our numerical calculations. Although any physical plasma will have some level of viscosity, its effect will be minor in terms of energy dissipation since it cannot liberate topological energy tied up in the magnetic field. The main reason for introducing viscosity is to stave off numerical artifacts.

An important feature of the equations (4.1–4.3) is that the small parameters η and ν can be scaled out of the equations if we specify $\nu \sim \eta$. To see this, let us look at the planar equations, in which case we may use the flux and stream function formulation (3.1). The planar equations then reduce to the system (4.9, 4.10) below. If we assume the forms

$$\phi = \alpha xy + f(x,t) \tag{4.4}$$

$$\psi = \beta xy + g(x,t) \tag{4.5}$$

equations (4.9) and (4.10) reduce to (Craig and Watson, 1999)

$$f_t + \alpha x f_x = 2\alpha f - 2\beta g + \beta x g_x + \nu f_{xx} \tag{4.6}$$

$$g_t + \alpha x g_x = \beta x f_x + \eta g_{xx} \, . \tag{4.7}$$

We can see that if we now substitute

$$\bar{x} = c_1 x/\eta^{1/2} = c_2 x/\nu^{1/2} \, , \tag{4.8}$$

both equations become independent of η and ν.

We will begin with two dimensional simulations and see whether solutions similar to the analytic model of Section 3.2 develop. Following this we will investigate three dimensional numerical solutions, where we hope to generate the spine and fan structures predicted by the analytic models of Section 3.3.

4.1 Reconnection simulations in two dimensions

In two dimensions we employ the flux and stream function formulation (3.1). Substituting these into (4.2), (4.3) and the curled form of (4.1) gives

$$\dot{\omega} + [\omega, \phi] = [J, \psi] + \nu \nabla^2 \omega, \tag{4.9}$$

$$\dot{\psi} + [\psi, \phi] = -\eta J, \tag{4.10}$$

where $\dot{f}$ denotes $\partial f/\partial t$, while $\omega = -\nabla^2 \phi$ and $J = -\nabla^2 \psi$.

The simulations take place on the doubly periodic domain $[-1,1] \times [-1,1]$, with boundary conditions given by

$$\phi(-1,y) = \phi(1,y), \qquad \psi(-1,y) = \psi(1,y), \tag{4.11}$$

$$\phi(x,-1) = \phi(x,1), \qquad \psi(x,-1) = \psi(x,1), \tag{4.12}$$

using the two-dimensional doubly periodic code of Craig and Watson (1999). We concentrate on the properties of the transient resistive current layer in contrast to, for example, Longcope and Strauss (1993) who focus on the formation of current singularities in an ideal plasma. Primitive variables, the vorticity magnitude ω and the flux function ψ, are solved explicitly at each time level using a finite difference approximation. The stream function is then determined retrospectively by employing a fast Fourier transform routine to invert $\omega = -\nabla^2\phi$. The time-step size is calculated at each step based on the diffusion time (determined by the magnitudes of both η and ν) and maximum advection rate (which provides a Courant-Friedrichs-Lewy condition, see for example Richtmyer and Morton (1967)). The smallness of the damping coefficients η and ν means that the time-step is limited mainly by the CFL condition. In all our simulations we take a grid spacing so that at least 8 mesh points lie across the current layer. Runs at the highest resolution require grid spacings $\Delta x, \Delta y < 10^{-3}$.

A typical set of initial conditions is given by

$$\phi(x,y) = \alpha_0 \sin(\pi x)\sin(\pi y)/\pi, \tag{4.13}$$

$$\psi(x,y) = \beta_0 \sin(\pi x)\sin(\pi y)/\pi + g_0 \cos(\pi x)/\pi\ . \tag{4.14}$$

Here β_0 acts as a shear parameter and g_0 represents the strength of the disturbance field. Initially there is only shear in the magnetic field, but this term rapidly drives a shear component in the flow. When $\beta_0 = 0$ we generate a symmetric X-point at the origin, and head-on reconnection results. The great advantage of using periodic geometry is that the solution develops self-consistently, unhindered by numerical artifacts caused by the imposition of over-restrictive boundary conditions.

A consistent way to analyse the dynamic current sheet is to determine diagnostics at the time of maximum current (DeLuca and Craig, 1992). In the typical merging simulations of this chapter the current density builds from the small amount associated with the initial disturbance field (4.14) to an intense sheet as magnetic field is washed in by the flow. The current in the sheet reaches a maximum after approximately one Alfvén time for $\alpha_0 \simeq 1$, before dissipating away as the magnetic field reconnects through the X-point.

First we compare the properties of the shear flow numerical reconnection solution ($\beta_0 \neq 0$) with the analytic model of Section 3.2. We then go on to verify the predicted scalings of Section 3.2.2. The scalings are of course independent of the degree of shear determined by β. We postpone an investigation into the effects of the level of shear on the form of the solution until Section 5.1.

4.1.1 Numerical solutions in two dimensions

Figure 4.1 shows the field and flow patterns of a typical sheared reconnection simulation at the time of maximum current. It is clear that, despite the finite length of the sheared current sheet and the influence of viscosity on the flow profile, the field line plot and velocity profile are in good qualitative agreement with the analytic model, at least within the vicinity of the neutral point (compare the boxed areas with Figure 3.1).

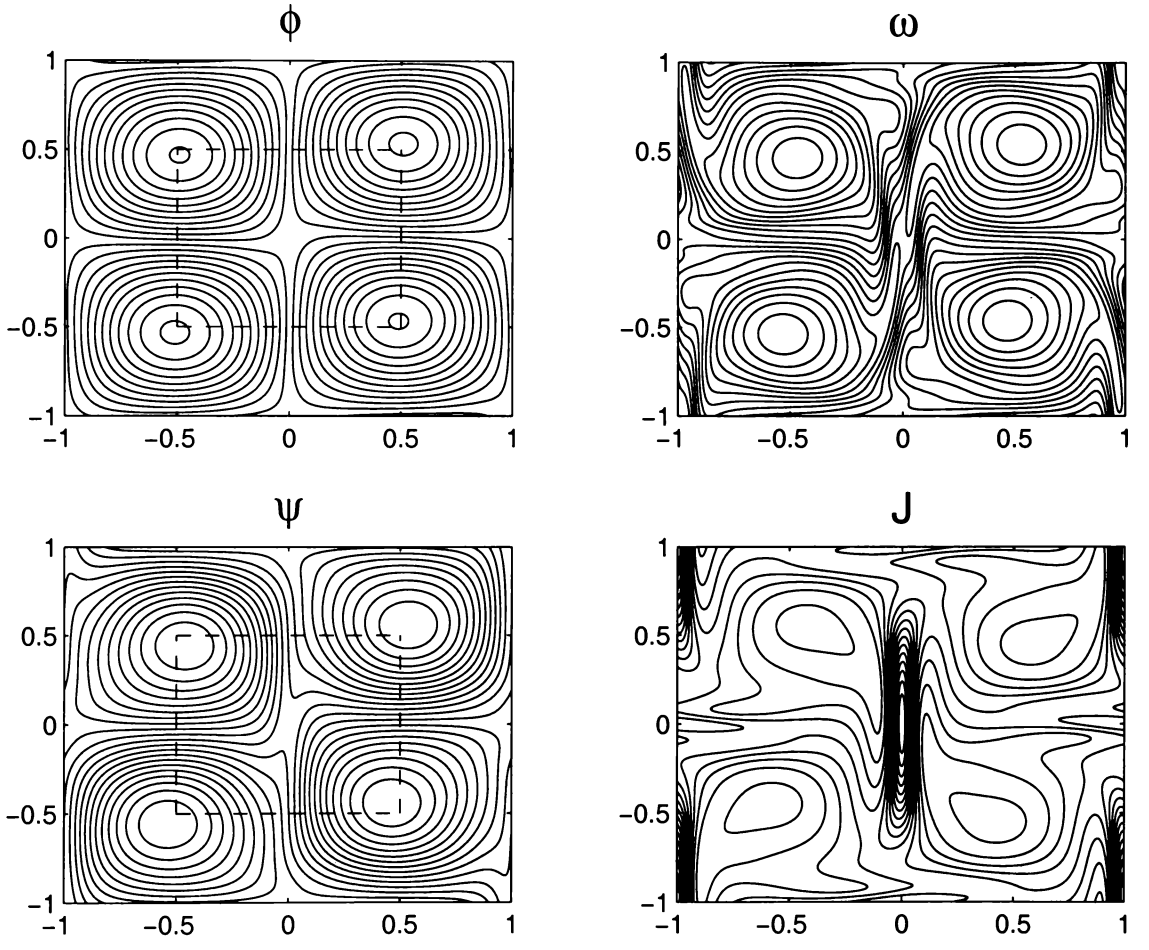

Figure 4.1: Contour plots of ϕ, ω, ψ and J, taken at the time of maximum current ($\sim$ 1 Alfvén time). Here we have used the initial conditions (4.13) and (4.14) with $\alpha_0 = -1$, $\beta_0 = 0.5$, $g_0 = 0.1$ and $\eta = \nu = 0.005$. Resolution is 400 grid points in both the x and y directions.

To provide a more detailed comparison we plot the simulated field profile and the analytic prediction (3.20) *across* the current layer in Figure 4.2. Considering there are no fitting parameters in the analytic model—we use $E = \dot{\psi}$ as measured at the neutral point—we find that flux pile-up of the field in the sheet region is

remarkably well represented by the analytically predicted Dawson function profile of Section 3.2.

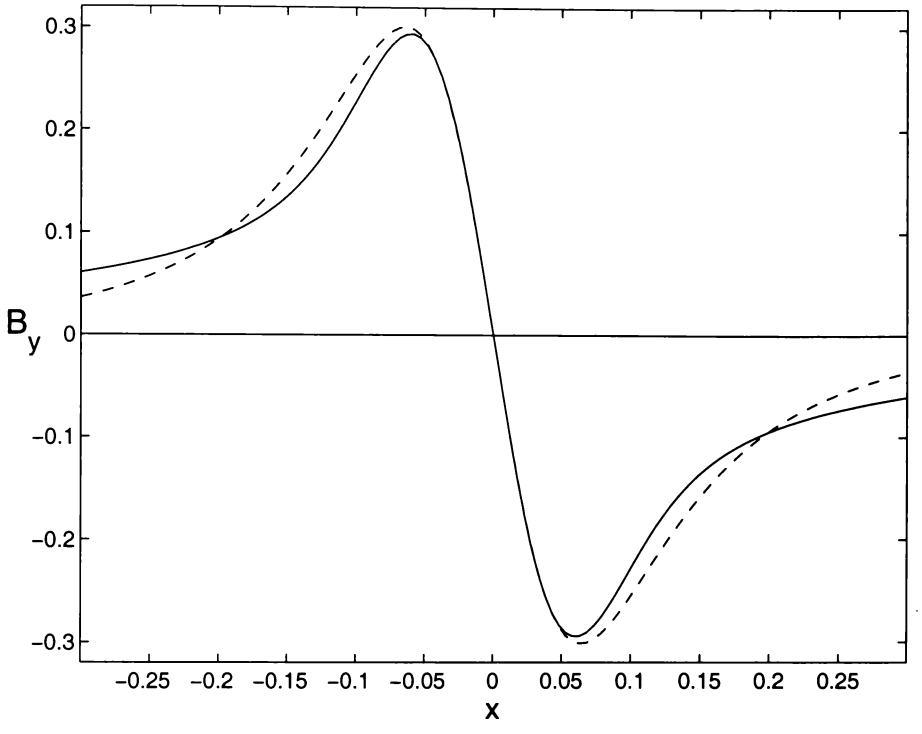

Figure 4.2: A slice of the y-component of **B** *along the inflow axis of the configuration of Figure 4.1. The dashed line is the numerical solution obtained using our periodic time-dependent code, while the solid line represents the analytic Dawson function solution given in (3.20).*

4.1.2 Reconnection scalings in two dimensions

Having established that the qualitative features of the analytic model readily form dynamically from a general initial condition, let us now verify some of the quantitative predictions. We can see in Figure 4.2 that both the analytic and numerical solutions are in close agreement within the current sheet region between the maximum pile-up fields. We will now look at the results of a sequence of runs to see whether the current sheet properties scale with η as predicted in Section 3.2.2.

Figure 4.3 shows the results of a set of scaling runs where we have set $\beta_0 = 0$ in (4.14), so that no shear flows are present. This case is similar to the $\beta = 0$ analytic solution (3.19, 3.20) which reduces to the solution of Sonnerup and Priest (1975). Despite the lack of shear flow, however, the numerical solution still reconnects, due to the presence of perpendicular flows at the ends of the current sheet (see Figure 4.1). The scalings are in good agreement with the predictions given in Section 3.2.2.

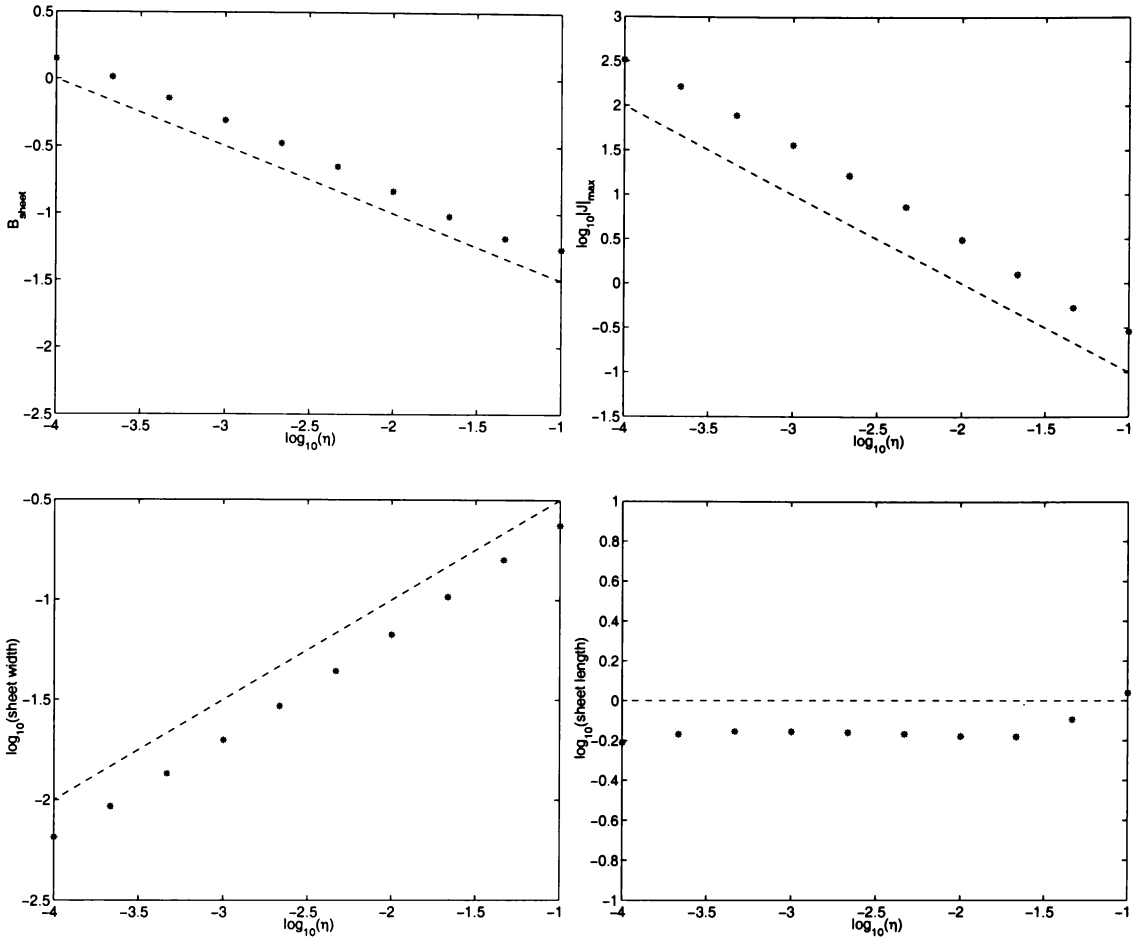

Figure 4.3: Current sheet scalings for the initial conditions (4.13) and (4.14) with $\beta_0 = 0$ *and* $g_0 = 0.06$. *Dashed lines represent the scalings of Section 3.2.2.*

Figure 4.4 is very similar, except that this time we have specified a strong shear flow by setting $\beta_0 = 0.5$. It is clear from these figures that the presence of shear flows does not undermine the scaling properties of the current sheet. It should be mentioned that these scaling results are just a representative sample of a large number of runs.

As we saw in Section 3.3.6, the 2-D solution considered here is in fact a special case of more general 3-D solutions. We also know that time dependent effects can be incorporated (Craig and Fabling, 1998) to obtain an even more sophisticated model. What this two dimensional work demonstrates is that even the *least refined* analytic reconnection solution provides a sound basis for describing the properties of a dynamic reconnecting current sheet.

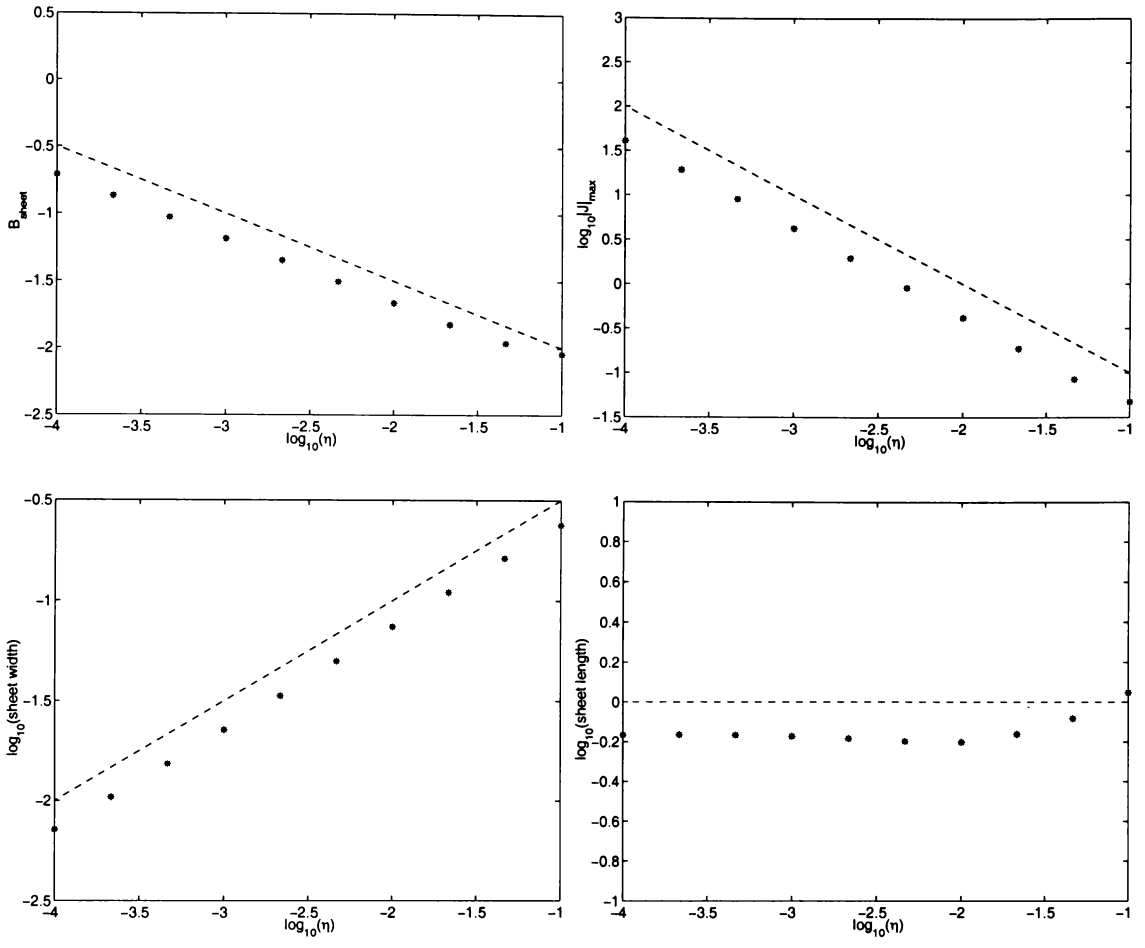

Figure 4.4: Current sheet scalings for the initial condition (4.13) and (4.14) with $\beta_0 = 0.5$ and $g_0 = 0.01$. Dashed lines represent the scalings of Section 3.2.2.

4.2 Reconnection simulations in three dimensions

The code used for the three dimensional calculations is in the same vein as the 2-D code used in the previous section. It solves the incompressible time-dependent MHD equations (4.1, 4.2 and 4.3) over the periodic $(-1, 1)$ cube. However in this case we cannot employ a flux or stream function, and so we are forced to work with $\mathbf{v}$ and $\mathbf{B}$ directly. The advantage of using a flux and stream function is that $\nabla \cdot \mathbf{v} = \nabla \cdot \mathbf{B} = 0$ by definition, whereas care must be taken to prevent divergence via numerical inaccuracies when dealing with the complete vector fields. In fact we are forced to use a "spread out" second derivative in order to conserve $\nabla \cdot \mathbf{B} = 0$.

Unlike the 2-D code of the previous section, the 3-D code does not use the curled form of the momentum equation. As such pressure appears explicitly in the equations. To solve for the pressure we must invert $\nabla p = \boldsymbol{\xi}$, where $\boldsymbol{\xi} = \mathbf{J} \times \mathbf{B} + \nu \nabla^2 \mathbf{v} - \partial \mathbf{v} / \partial t$, which we in fact do by solving $\nabla^2 p = \nabla \cdot \boldsymbol{\xi}$.

The main limiting factor with any 3-D code is resolution. The storage re-

quirements for several variables over three space dimensions becomes excessive very quickly. Even with memory saving tricks such as not storing derivatives and ghost points, a $100 \times 100 \times 100$ cube uses around 400Mb, which is about the storage limit of presently available machines. If we wish to have 10 grid points over a $\sqrt{\eta}$ length scale we are restricted to values of $\eta > 0.01$, which is just on the limit of obtaining interesting results which do not diffuse rapidly in situ. To improve our effective resolving power without introducing more grid points, we employ fourth order differencing. The stability condition on the time step corresponding to fourth order differences in the russian scheme (A.1) is derived in Appendix 1.

4.2.1 Numerical spine, fan and separator solutions

Here we employ the 3-D periodic code mentioned above to model magnetic merging. Though numerical resolution will be limited, we can at least test whether the predicted spine, fan and separator currents form self consistently with fairly general initial conditions. We use the following 3-D periodic stagnation point flow for $\mathbf{v} = (u, v, w)$, analogous to the 2-D background field (3.31) which we used in the analytic work of Chapter 3.

$$\begin{aligned} u &= \alpha \sin(\pi x)\cos(\pi y)\cos(\pi z) \\ v &= \alpha \sin(\pi y)\cos(\pi z)\cos(\pi x) \\ w &= -2\,\alpha \sin(\pi z)\cos(\pi x)\cos(\pi y) \end{aligned} \tag{4.15}$$

We overlay this with a magnetic field $\mathbf{B} = (X, Y, Z)$ which incorporates a component of the flow as well as a disturbance field.

To drive currents in the fan surface we use

$$\begin{aligned} \alpha &= 1 \\ X &= \beta u \\ Y &= \beta v + g_0 \sin(\pi z) \\ Z &= \beta w\ . \end{aligned} \tag{4.16}$$

Figure 4.5 shows the results of a run using these initial conditions.

If instead we wish to drive spine currents we use

$$\begin{aligned} \alpha &= -1 \\ X &= \beta u \\ Y &= \beta v \\ Z &= \beta w + g_0 \sin(\pi y)\ . \end{aligned} \tag{4.17}$$

This is not quite consistent with the analysis of the previous chapter where we used cylindrical mode disturbances. However, the gross feature of the above disturbance,

$g_0 \sin(\pi y)$, is similar to an $m = 1$ mode in the sense that there is one axis along which the disturbance vanishes. The resulting current structure can be seen in Figure 4.6.

For separator currents we expect to obtain a current ribbon (see discussion of Section 3.3.7). To generate this we use the following 2-D flow combined with a planar disturbance and a constant $\hat{\mathbf{z}}$ field.

$$\begin{aligned} u &= \sin(\pi x)\cos(\pi y) \\ v &= -\sin(\pi y)\cos(\pi x) \\ w &= 0 \\ X &= g_0 \sin(\pi y) \\ Y &= 0 \\ Z &= g_0/2 \end{aligned} \tag{4.18}$$

Looking at any slice of constant z, the field line structure is identical to that of "head-on" merging described in the previous section. However in this case the z-axis represents a field line and near anti-parallel field lines in the outfield (where B_z is small) become tilted as they enter the current sheet (where B_z is comparatively large). Figure 4.7 shows such a situation.

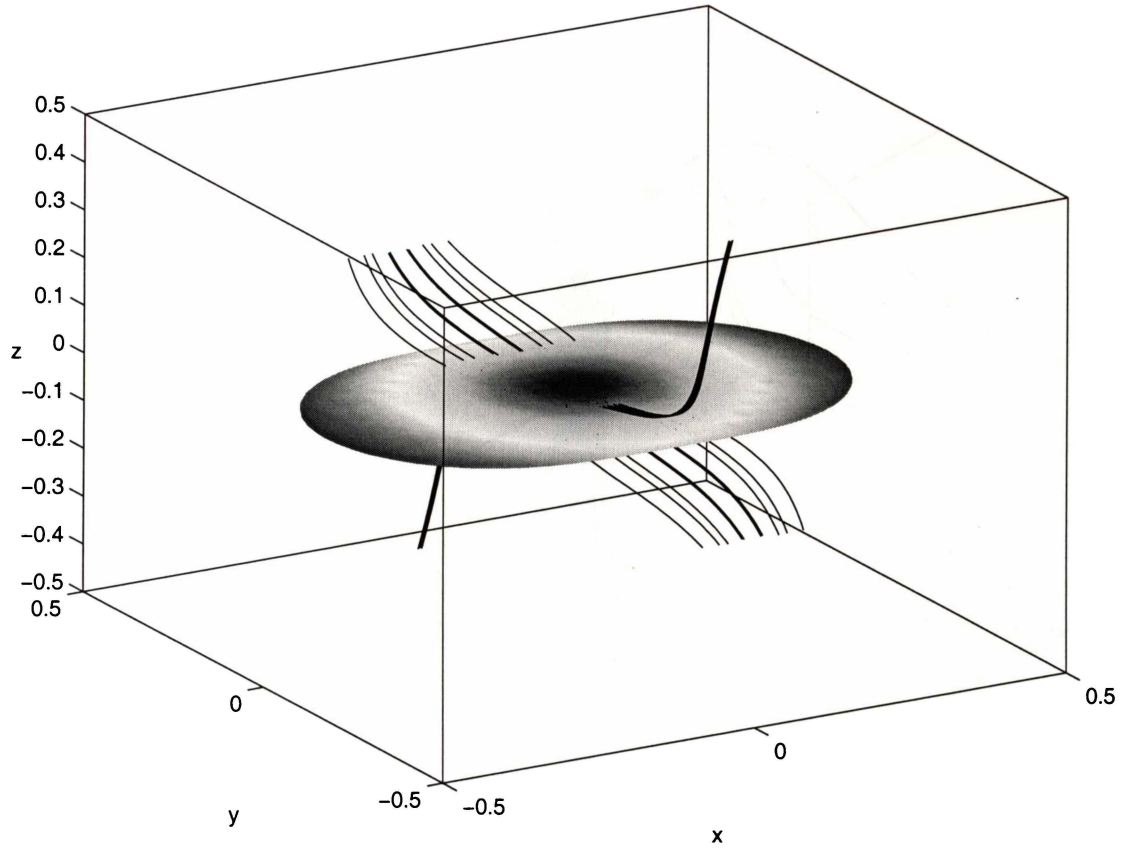

Figure 4.5: Isosurface of current with some representative field lines taken at the time of maximum current showing fan current reconnection. We have used $\eta = \nu = 0.03$ *with the initial conditions (4.15) and (4.16) on a* $60 \times 60 \times 60$ *grid.*

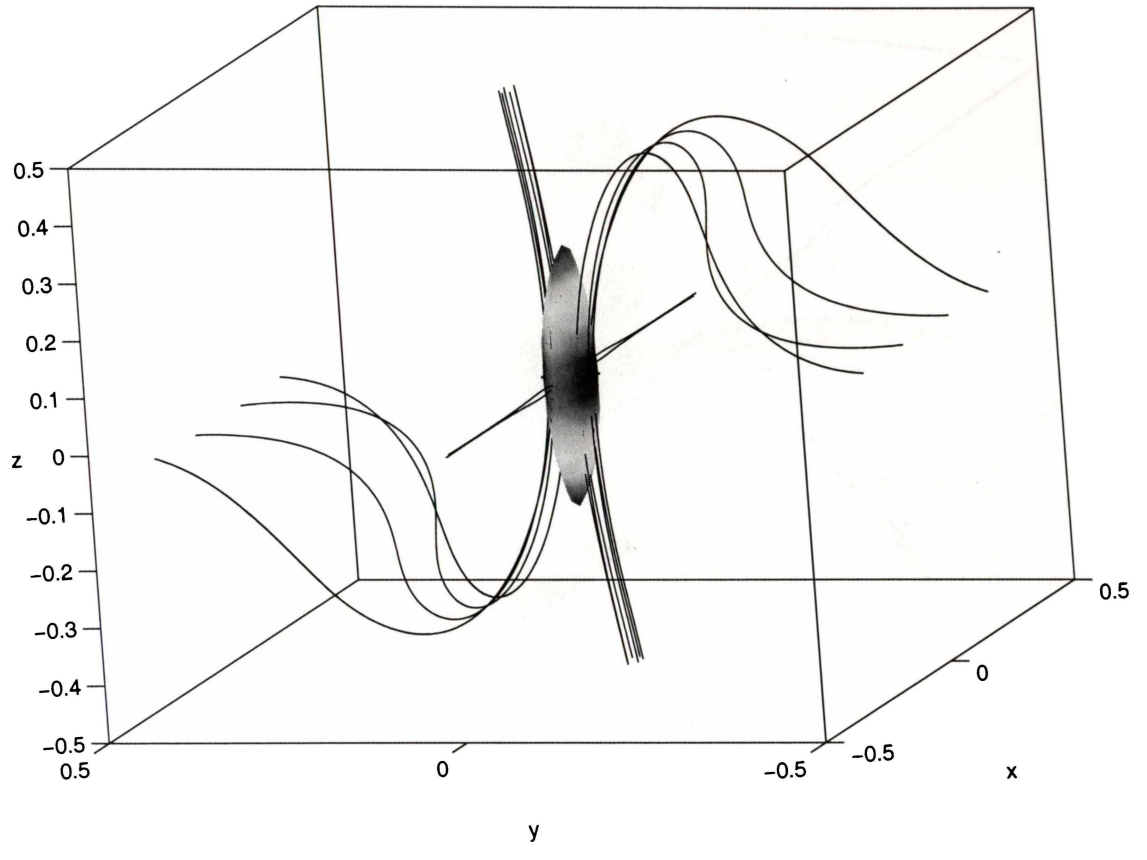

Figure 4.6: Isosurface of current with some representative field lines taken at the time of maximum current showing spine current reconnection. We have used $\eta = \nu = 0.03$ *with the initial conditions (4.15) and (4.17) on a* $60 \times 60 \times 60$ *grid.*

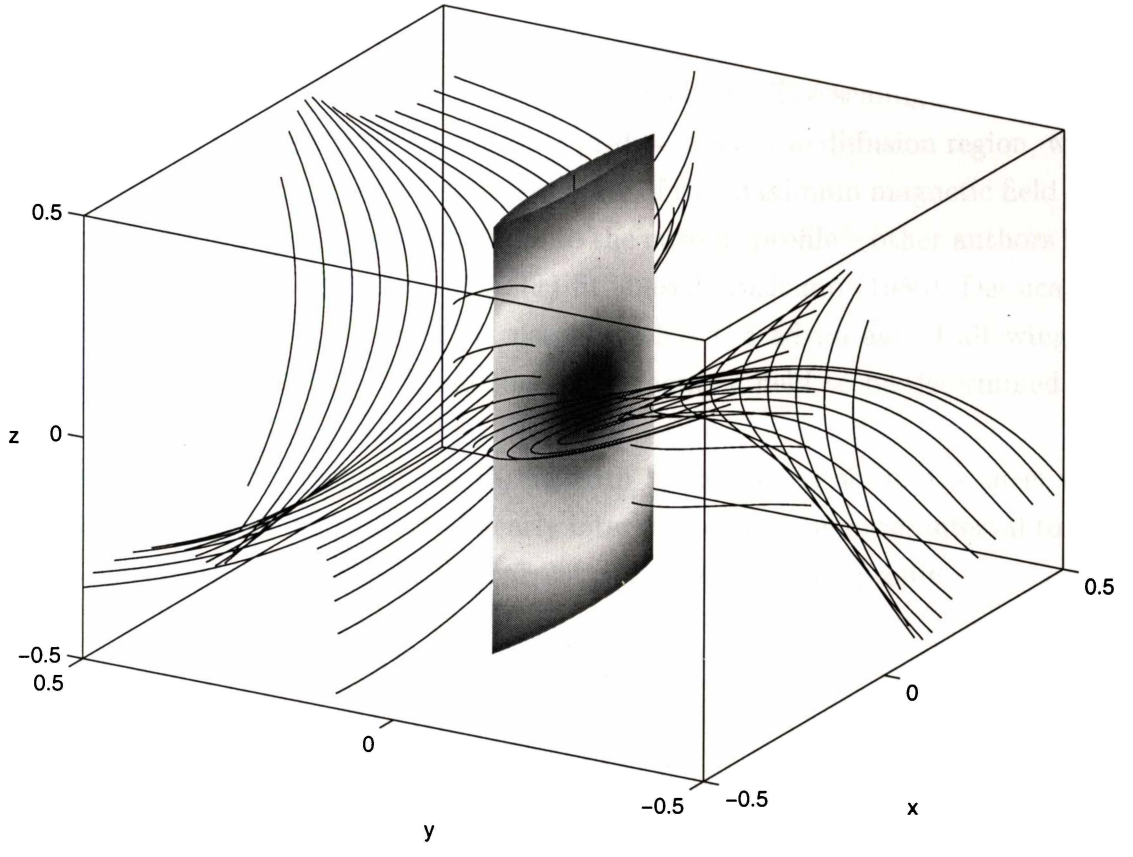

Figure 4.7: Isosurface of current with some representative field lines taken at the time of maximum current showing separator reconnection. We have used $\eta = \nu = 0.03$ *with the initial conditions (4.18) on a* $60 \times 60 \times 60$ *grid. Note the tilting of field lines due to the uniform* B_z.

4.2.2 Numerical scalings in three dimensions

By considering boundary layer effects associated with the resistive current sheet of the analytic model, we can make predictions of how certain critical properties of the sheet scale with respect to the resistivity (see Section 3.3.5). To test these numerically we run the previous initial conditions for a range of η values and measure the maximum current, the magnetic pile-up and the current sheet width. To obtain a consistent set of results we choose a resolution so that for each run we have a fixed number of grid points inside a $\sqrt{\eta}$ length-scale.

Obviously, when working in three dimensions, resolution is a severe limiting factor in obtaining accurate results. Machine capacity, at the time of writing, limits us to 115 mesh points from -1 to 1 in all three directions. The scaling runs skimp on resolution, with normally only a handful of grid points in the diffusion region, which makes it difficult to obtain an accurate estimate of the maximum magnetic field pile-up. For this reason we fit a $\cosh(x)$ curve to the current profile – other authors have used a similar procedure where a $\cosh^2(x)$ fit is used (Biskamp (1986), DeLuca and Craig (1992)). However, the method used here has the advantage of allowing the current profile to be integrated and the peak magnetic field to be determined (see Figure 4.8 and discussion below).

Firstly we establish the current sheet width by traversing across the sheet until the current changes sign. Next we linearly interpolate over the mesh interval to find the sheet width x_w. We then fit the current with the following profile

$$\hat{J}(x) = J_{\max} + 1 - \cosh(\mu x) \ , \tag{4.19}$$

where

$$\mu = \frac{1}{x_w} \cosh^{-1}(J_{\max} + 1) \ .$$

This leads to the maximum pile-up field

$$\hat{B}_{\max} = (J_{\max} + 1)x_w - \sinh(\mu x_w)/\mu \ . \tag{4.20}$$

Figure 4.8 shows the result of this fitting process when we use the fan current initial conditions with 35 grid points (2.4 points in $\sqrt{\eta}$) in all three directions with $\beta = 0.1$ and $\eta = \nu = 0.02$.

When conducting scaling runs with respect to resistivity, one immediate question that arises is what level of viscosity to use. Some authors (e.g. Biskamp) use $\nu = \eta$, which effectively scales both diffusion coefficients out of the equations. The reason for this is that, as we saw when we made the substitution (4.8) at the start of this chapter, when resistivity and viscosity scale in the same way there is a unique small length scale $x \sim \eta^{1/2} \sim \nu^{1/2}$.

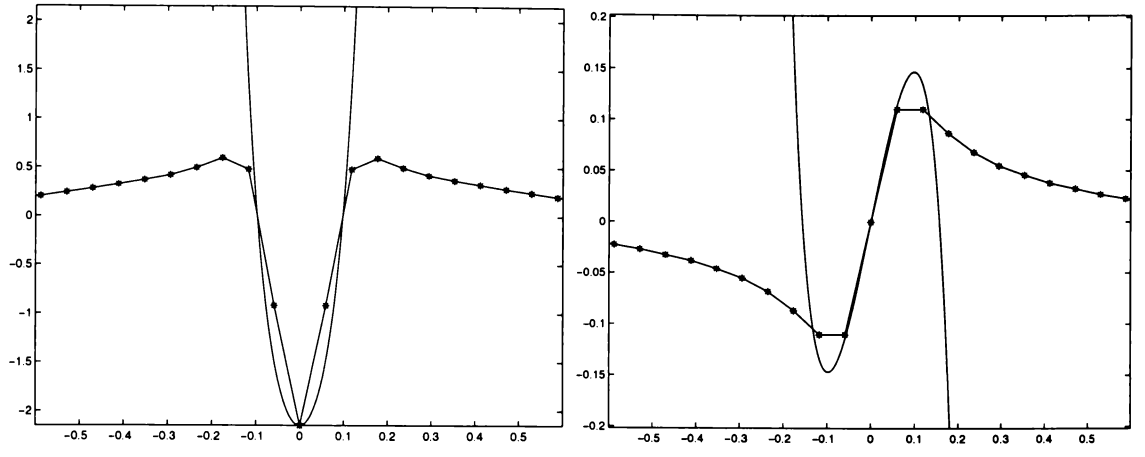

Figure 4.8: Results of the fitting process to both the current (left) and magnetic field (right). The smooth curves are given by (4.19) and (4.20) respectively, while the asterisks mark computed values.

The scaling runs with $\nu = \eta$ work well for both fan and separator configurations. However, for spine curent sheets something goes wrong. The localisation time, in particular, behaves inconsistently. It may be that the periodic nature of our numerical box is causing interference between various nulls. It may also be that the small length scales and steep gradients associated with the spine are not being sufficiently resolved. A third possibility is that the justification for setting $\eta \sim \nu$, based on planar analysis (4.8), does not hold for fully 3-D flows such as those present in the spine calculations. This problem will be the subject of further investigation. For the present we find that holding the viscosity fixed gives rise to consistent results for the spine, as well as for the fan and separator. Hence the scaling results which follow are all done with viscosity fixed at $\nu = 0.01$.

Of the scaling quantities analysed, the localisation times are the most difficult to interpret. The analysis of Section 3.4, in which we predict a scaling for the localisation time, assumes linear inflow conditions which we are not able to replicate in our periodic simulations. The average slope of the velocity profile looks to be important in the fan results, as this implies $\alpha = 4$. However, associating α with the average slope doesn't work for the spine where we see twice the expected value. It is clear though that the time scales as $A \ln(1/\eta)$, where A is some number relating to the inflow profile.

The quartet of graphs in Figure 4.9 depicts scalings for fan current reconnection. In these plots we have used $\beta = 0.1$, $g_0 = 0.003$ and $\nu = 0.01$. Since the initial conditions specify a symmetric flow field ($\kappa = 1/2$) superposed with a weak 1-D disturbance, we expect, from the scaling arguments of Sections 3.3.5 and 3.4, the

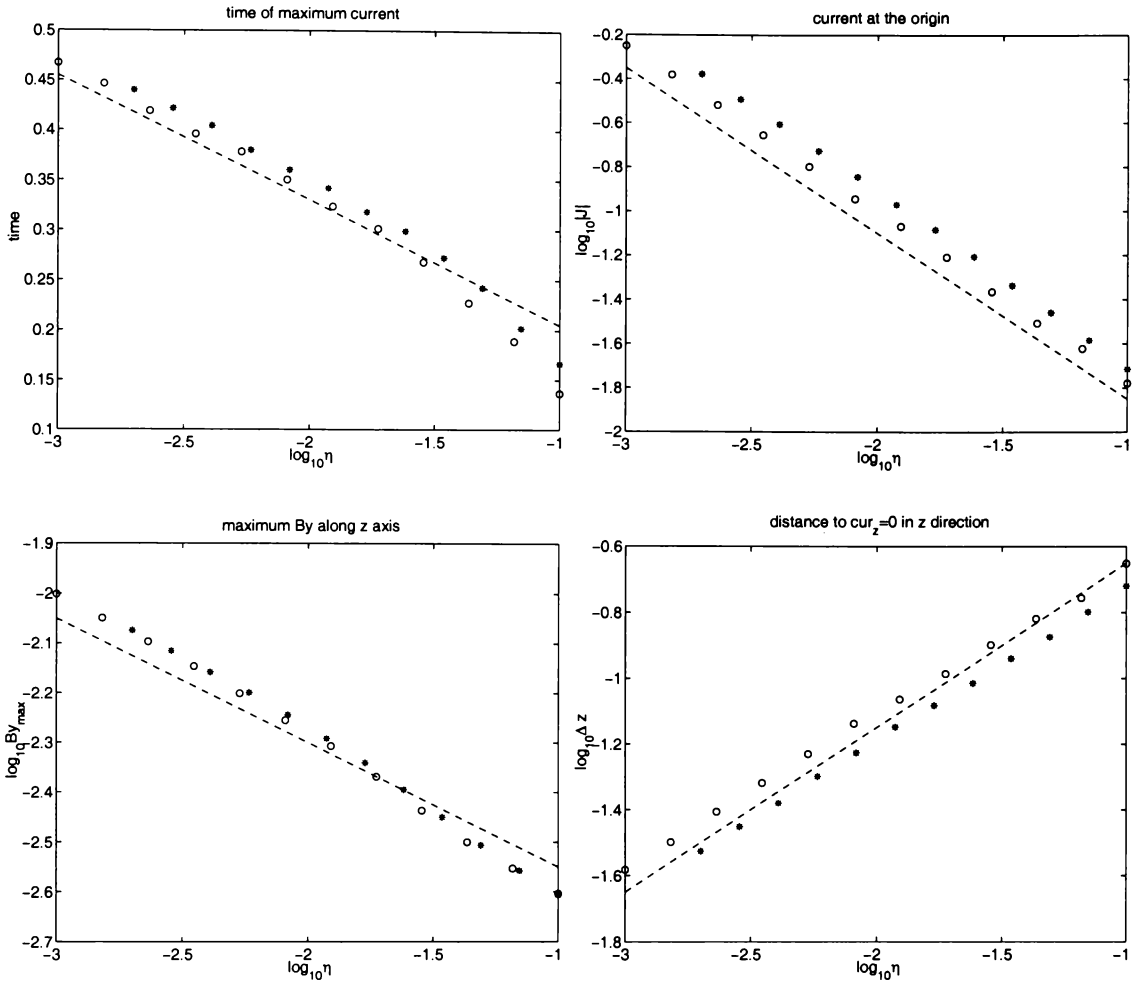

Figure 4.9: Scalings for the time of maximum current, maximum current, maximum field build up and sheet width for a fan reconnection simulation (4.16). The set of runs depicted by '' has 2.5 grid points within a $\eta^{1/2}$ length-scale, while the 'o' runs use only 1.8. The level of viscosity is fixed at $\nu = 0.01$, $\beta = 0.1$ and $g_0 = 0.003$ in all cases. The reference lines reflect the analytic predictions of (4.21).*

scalings to obey

$$t \sim -\frac{1}{2\alpha}\ln(\eta)\,, \quad J_{\max} \sim \eta^{-3/4}\,, \quad B_{\max} \sim \eta^{-1/4}\,, \quad \Delta z \sim \eta^{1/2}\,. \tag{4.21}$$

The slopes of the reference lines in the figure are set in accordance with these predictions and the numerical scalings are in clear agreement.

Figure 4.10 shows the scalings for spine current reconnection. For all runs we have set $\beta = 0.1$, $g_0 = 0.003$ and $\nu = 0.01$. Since we are imposing a weak 1-D disturbance field onto a symmetric stagnation point, we expect, from the scaling arguments of Sections 3.3.5 and 3.4, that the scalings will be given by

$$t \sim -\frac{1}{\alpha}\ln(\eta) \quad , \quad J_{\max} \sim \eta^{-3/2} \quad , \quad B_{\max} \sim \eta^{-1} \quad , \quad \Delta y \sim \eta^{1/2}\,. \tag{4.22}$$

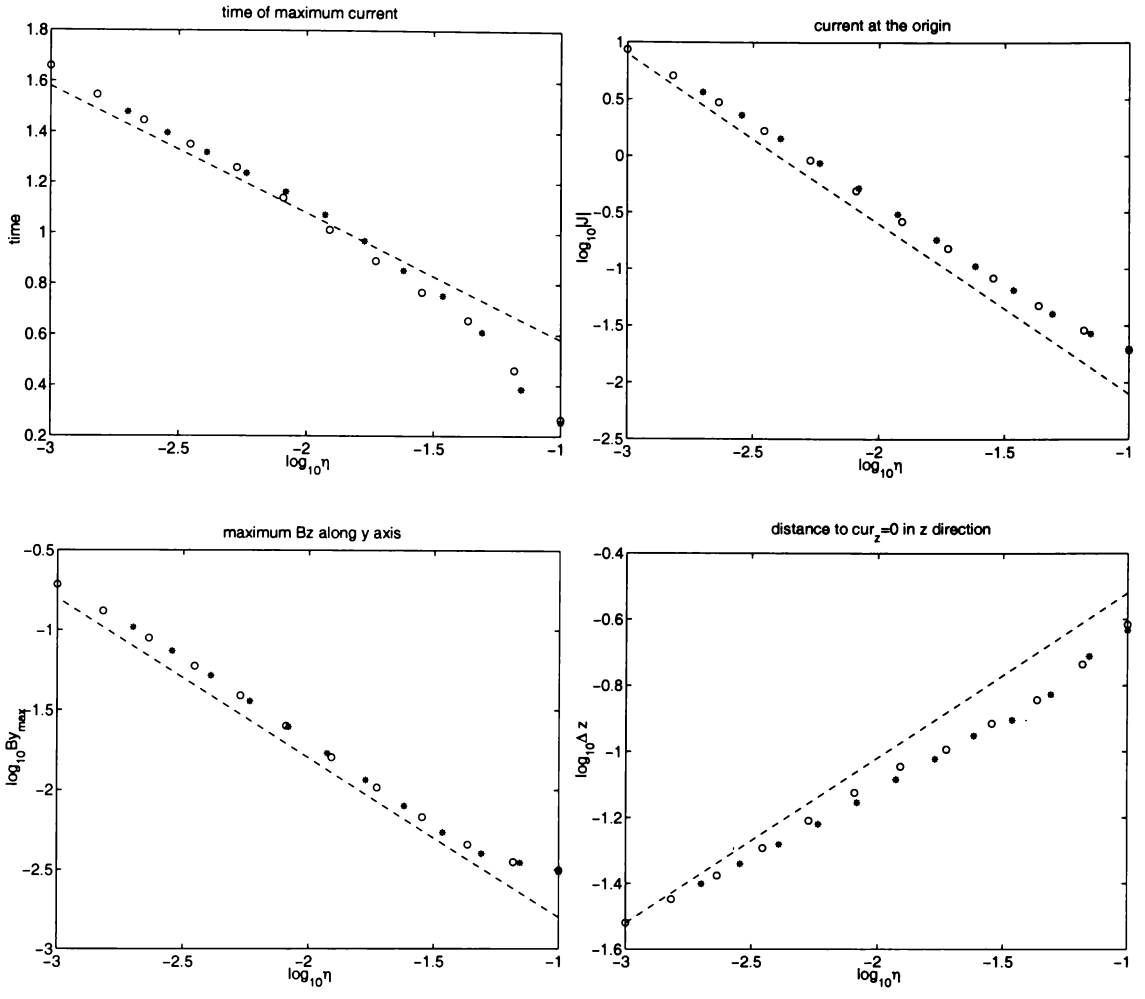

Figure 4.10: Scalings for the time of maximum current, maximum current, maximum field build up and sheet width for a spine reconnection simulation (4.17). The set of runs depicted by '' has* 2.5 *grid points within a* $\eta^{1/2}$ *length-scale, while the 'o' runs use only* 1.8. *The level of viscosity is fixed at* $\nu = 0.01$, $\beta = 0.1$ *and* $g_0 = 0.003$ *in all cases.*

It is clear, from Figure 4.10, that with viscosity fixed for all runs there is consistent agreement with the above scaling predictions. The localisation time appears to be consistent with an inflow amplitude $\alpha = 2$.

The final set of 3-D scalings is for the case of separator reconnection. As we discussed in Section 3.3.7, separator reconnection is a quasi 2-D process, and as such we expect the 2-D scalings to apply. For the present configuration, given by the initial conditions (4.18), we anticipate the following scalings.

$$t \sim -\frac{1}{2}\ln(\eta) \quad , \quad J_{\max} \sim \eta^{-1} \quad , \quad B_{\max} \sim \eta^{-1/2} \quad , \quad \Delta y \sim \eta^{1/2} \, . \tag{4.23}$$

The slopes of the reference lines in Figure 4.11 are set to the above predictions and again the numerical scalings are in excellent agreement.

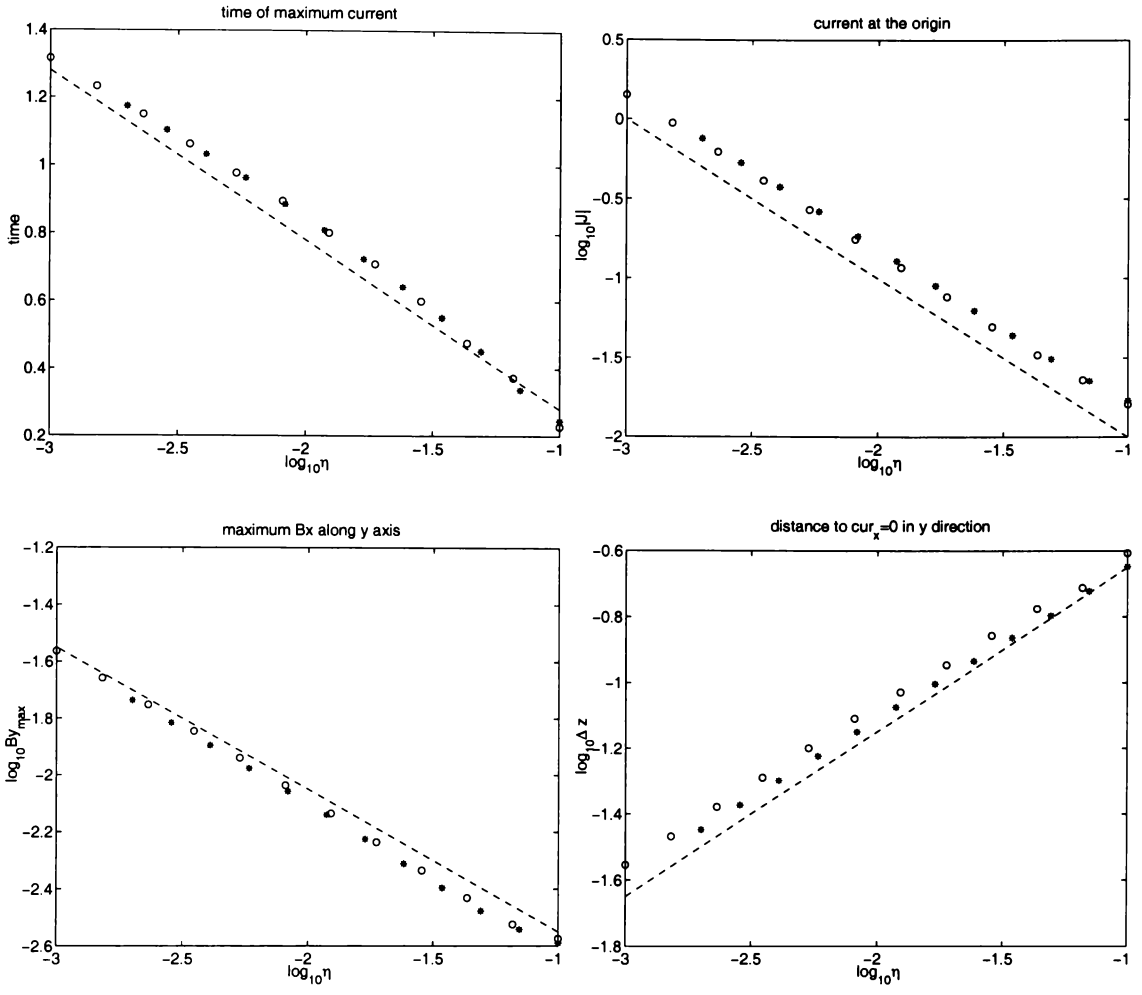

Figure 4.11: Scalings for the time of maximum current, maximum current, maximum field build up and sheet width for a spine reconnection simulation (4.18). The set of runs depicted by '' has* 2.5 *grid points within a* $\eta^{1/2}$ *length-scale, while the 'o' runs use only* 1.8. *The level of viscosity is fixed at* $\nu = 0.01$ *and* $g_0 = 0.003$ *in all cases.*

4.3 Summary

We have investigated numerical solutions to the incompressible time-dependent MHD equations in both two and three dimensions. Our aim was to verify whether the forms predicted by the analytic work discussed in Chapter 3 manifest from general initial conditions, with the least intrusive boundary conditions available (periodic). As such the Dawson profile of the transient magnetic field obtained from a global initial magnetic field (see Figure 4.2) represents a triumph for the C&H solution (3.19, 3.20). Of course we need to check that this is not a one-off fluke. As such we examined the current sheet properties for two different values of the shear parameter β and varied η over several orders of magnitude. We found

that these scaling results compare favourably to the analytic scaling predictions of Section 3.2.2.

The 3-D simulations are more limited, due mainly to their memory intensive nature. However, the predicted spine and fan current structures are easily reproduced. The scalings also correspond well to the predictions. The only puzzle is that, although both fan and separator scalings seem to be insensitive to whether viscosity is fixed or a scalar multiple of η, the spine scalings only appear to work for ν fixed. As we already stated, this may be a result of the periodic geometry, the diminutive dimensions of the spine current sheet, or simply that the planar analysis does not apply. This last observation is of course consistent with the fact that the fan and separator scalings do work both for fixed and varied ν, since their flow geometries are inherently planar. The effects of varying viscosity will be the subject of further work. The bulk of the 3-D numerical results appear to be in good agreement with the analytic solutions of Chapter 3. As such we expect the 3-D analytic solutions to capture the essence of neutral point magnetic merging in situations where the flow resembles a three dimensional stagnation point.

Chapter 5

Current sheet properties in two dimensions

In this chapter we will investigate some of the properties of two dimensional current sheets that have not been covered in Chapters 3 and 4. We begin by taking a detailed look at reconnection solutions incorporating shear flows and compare these with head-on merging situations. In our treatment of reconnection so far we have ignored or avoided certain subtleties which will also be addressed in this chapter. The stalling of the magnetic merging process due to excess pressure building up within the current sheet, for example, quickly manifests itself when time-dependent effects allow the magnetic pressure in the sheet to feed back on the flow. We have also ignored compressible effects thus far, which may play an important role. These two issues will be covered in Sections 5.2 and 5.3. Sections 5.4 and 5.5 will deal with field line osculation within a current sheet and the resistive tearing mode instability respectively.

5.1 Head-on versus sheared reconnection

In Chapter 4 we looked at numerical solutions to time-dependent reconnection. We found, in Section 4.1, that the properties of the analytic steady-state solution, of Section 3.2, are reproduced in dynamic simulations. The analytic solution has an arbitrary parameter β, which specifies the degree of shear in the magnetic and velocity fields. In fact the analytic reconnection solution degenerates to a pure annihilation solution when shearing is absent. Numerically we still expect this scenario to produce reconnection, due to our periodic flow profile. In what follows we will refer to simulations without shear as "head-on", and compare such solutions with those containing a high degree of shear.

We now compare sheared reconnection solutions with $\beta = 0$ head-on reconnec-

tion. To facilitate the analysis we use the diagnostic quantities of Watson *et al.* (1998), namely

$$\mathbf{v}_\perp = \frac{(\mathbf{E} - \eta\mathbf{J})}{B^2} \times \mathbf{B} \quad \text{and} \quad \mathbf{v}_f = \frac{\mathbf{E} \times \mathbf{B}}{B^2}. \tag{5.1}$$

The quantity $\mathbf{v}_\perp$ represents the component of the fluid velocity perpendicular to the magnetic field, while $\mathbf{v}_f$ gives the velocity of the field lines themselves. The difference between these two quantities is the field line slippage velocity, given by

$$\mathbf{v}_s = \mathbf{v}_f - \mathbf{v}_\perp = \frac{\eta\mathbf{J} \times \mathbf{B}}{B^2}. \tag{5.2}$$

5.1.1 Simulation results

The simulations of this section are an extension of the numerical work of Section 4.1. As such we employ the same 2-D periodic code to solve equations (4.9) and (4.10). We also use the same initial condition given by

$$\phi(x, y) = \alpha_0 \sin(\pi x) \sin(\pi y)/\pi, \tag{5.3}$$

$$\psi(x, y) = \beta_0 \sin(\pi x) \sin(\pi y)/\pi + g_0 \cos(\pi x)/\pi\ . \tag{5.4}$$

This initial configuration has only a small amount of current associated with it, but an intense sheet forms along the y-axis as magnetic field is washed into the neutral point. Figure 4.1, in the previous Chapter, shows a typical configuration at the time of maximum current.

Figure 5.1 shows a comparison of the head-on and sheared simulations at the time of maximum current. The initial conditions are the same for both runs except for the shear parameters ($\beta_0 = 0$ and $\beta_0 = 0.5$). The small arrows represent the field line slippage velocity, and as expected the slippage is greatest in the central high current region (shades of yellow). Notice the slippage in the exhaust region as the field lines are flung away from the neutral point. The sheared solution has a much larger exhaust region, which allows this configuration to transfer magnetic energy into kinetic energy at a faster rate.

The plots in Figure 5.2 compare some of the sheared and head-on current sheet properties. It is clear that the tendency for flux pile-up is relatively suppressed in the sheared solution. Correspondingly the current density is less intense when shearing is present. The bottom right plot of this figure shows that the magnetic field in the sheared outflow is considerably more intense. Extra field in the exhaust sector will give rise to a stronger magnetic sling-shot effect, which in turn will help to drive the reconnection. The fact that this curve is linear in both the sheared and head-on cases, demonstrates that the field lines reconnect at a finite angle and do not osculate—osculation would imply a cubic profile as discussed in Section 5.4.

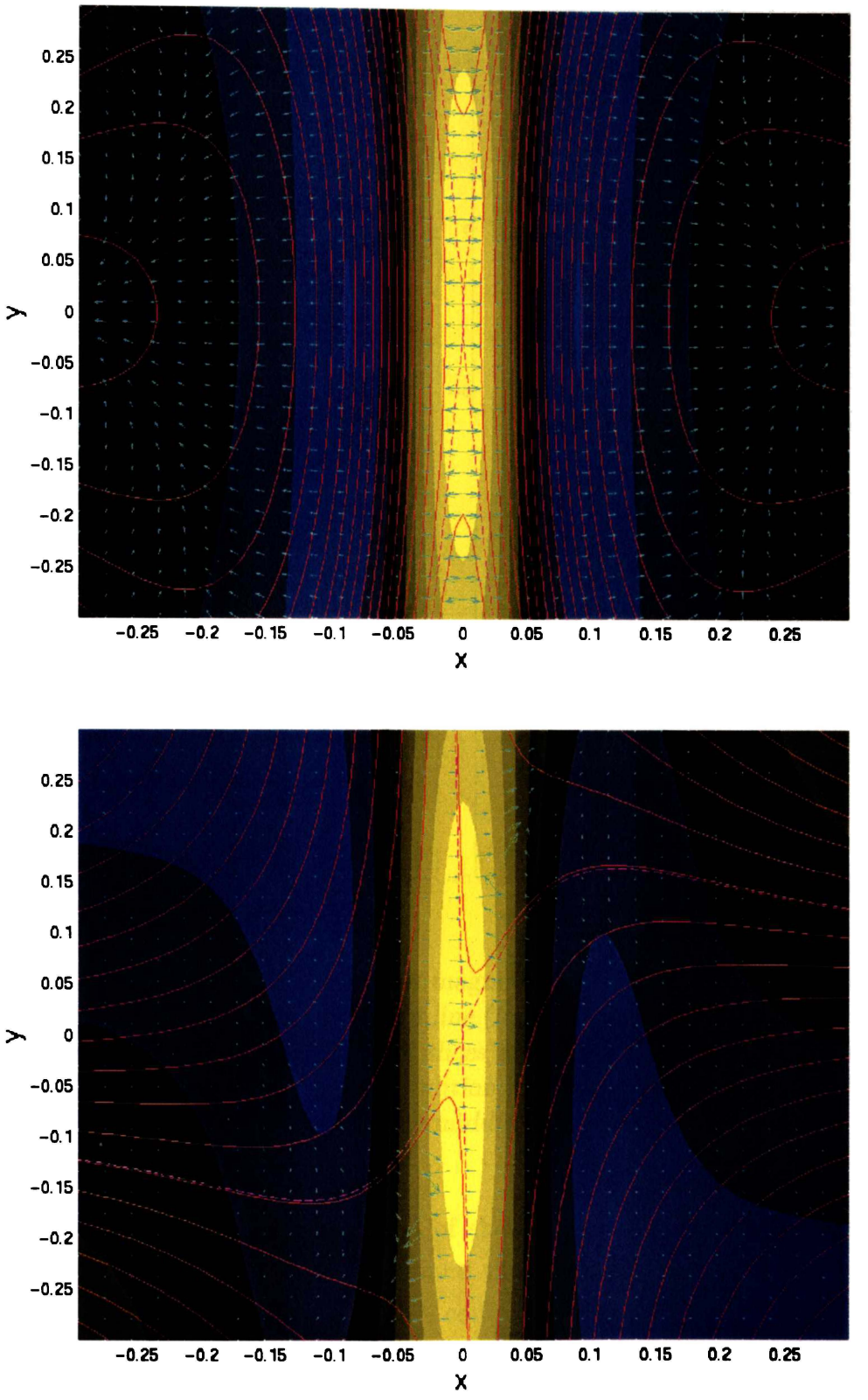

Figure 5.1: Dynamic head-on and sheared reconnection solutions at the time of maximum current. In both cases the initial conditions are the same as in Figure 4.1 except that for the head-on reconnection (top) $\beta_0 = 0$. The shades of yellow and blue represent positive and negative current, the magnetic field lines are drawn in red and the field separatrices are dashed purple lines. The small light blue arrows indicate the field line slippage velocity as defined in (5.2).

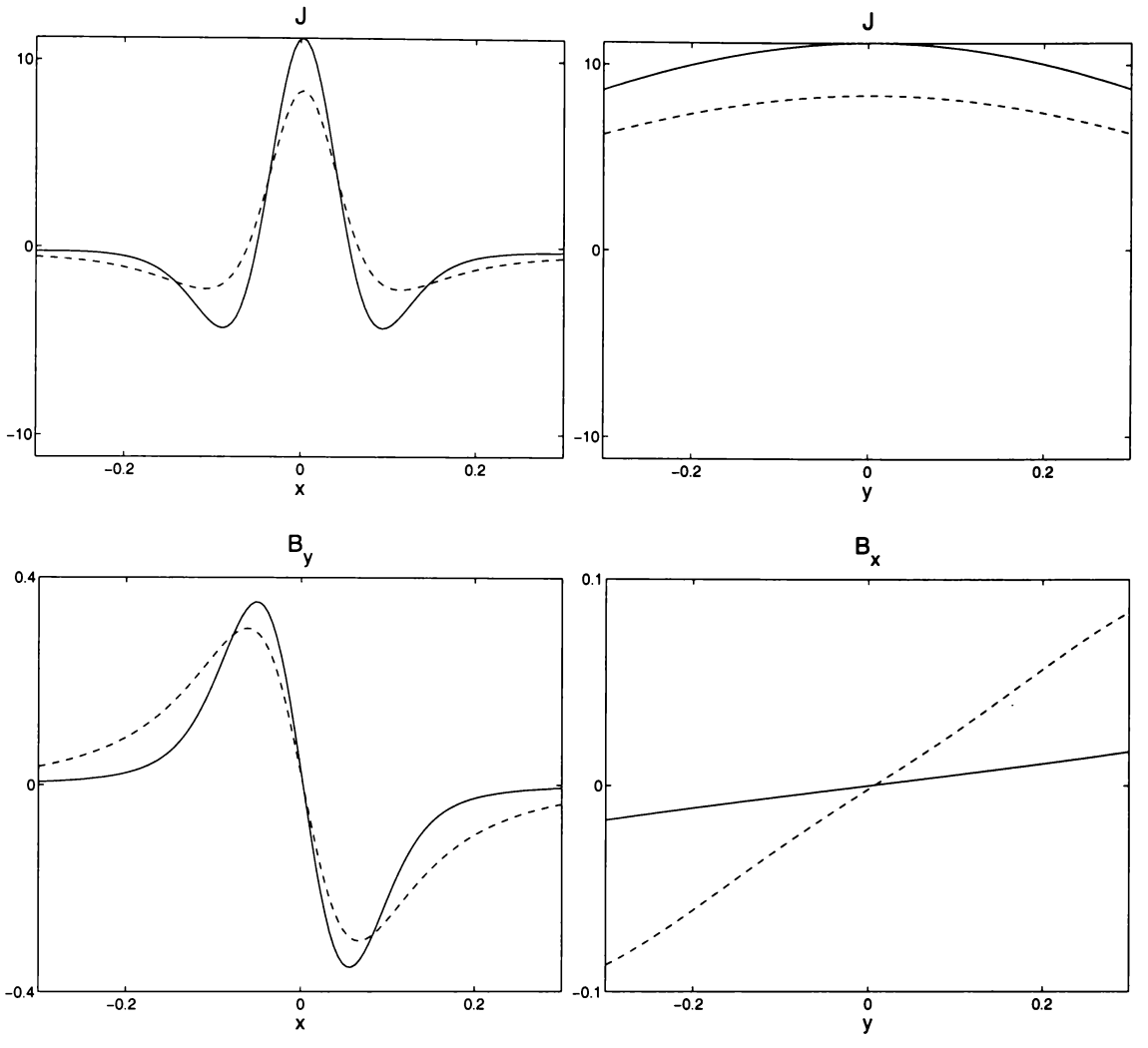

Figure 5.2: Slices of current (top) and magnetic field (bottom) taken across and along the sheets of Figure 5.1. The solid line (head-on) has $\beta_0 = 0$ while the dashed line (sheared) uses $\beta_0 = 0.5$. Note: all slices are taken along the coordinate axes, except for B_x with the sheared initial condition, where the slice is from $(-0.05, -0.3)$ to $(0.05, 0.3)$ so that it cuts through the middle of the separatrices.

We have investigated how the level of shear present in a solution affects the properties of the current sheet. We found that a highly sheared solution has a considerably wider outflow region when compared with a head-on configuration. We also found that the tendency for flux to pile-up was reduced in the case of shear flows. Since flux cannot accumulate unbounded, this last finding means that sheared solutions will ultimately release more energy when the effects of current sheet saturation are included. Saturation of the current layer is discussed in the next section.

5.2 Saturation of the current layer

In Section 3.2.2 we obtained analytic scaling predictions for a two dimensional current sheet and in Section 4.1.2 we verified these numerically. The way in which we expect various current sheet quantities to scale with resistivity can be summarised as follows:

$$l \sim \eta^{1/2} \quad , \quad B_{\max} \sim \eta^{-1/2} \quad , \quad J_{\max} \sim \eta^{-1} \quad , \quad W_{\eta} \sim \eta^{-1/2} \, . \tag{5.5}$$

The first thing to notice about these scalings is that they predict singular structures with unbounded dissipation in the limit $\eta \to 0$. Singular current structures occur naturally in ideal MHD and correspond to well defined current sheets when finite resistivity is introduced. In fact, we used this property in Section 3.3.3 to predict the current structures of spine and fan reconnection. What does not seem reasonable about these scalings, however, is the unbounded magnetic field due to the "flux pile-up" effect, for as the magnetic intensity increases, so does the associated magnetic pressure within the sheet.

We can define a total pressure in an incompressible magnetic configuration to be

$$P = p + \frac{1}{2}v^2 + \frac{1}{2}B^2 \, , \tag{5.6}$$

where p is the gas pressure. We find that P is approximately uniform over the entire domain, and will in practice reflect the "external" pressure driving the merging. What this means is that the hydromagnetic pressure, $v^2/2 + B^2/2$, cannot exceed a critical level determined by $P - p$, since the gas pressure must always be positive. It seems sensible, therefore, to limit the pressure within the current sheet to the same level it has on the inflow boundary (Craig and Watson, 2000b). Hence we must have

$$B^2_{\text{sheet}} < B^2_{\text{inflow}} + v^2_{\text{inflow}} \, , \tag{5.7}$$

where we have used the fact that v_{sheet} is small. These considerations suggest that the scalings (5.5) will hold with reductions in resistivity until B^2_{sheet} "saturates" when it becomes comparable to the hydromagnetic pressure of the inflow. If we continue to reduce η below this critical value, we expect to obtain scalings similar to the Sweet-Parker model (see Section 2.2.1) because within the current sheet the two models are now the same since B_{sheet} will be fixed with further reductions in η.

5.2.1 Hydromagnetic pressures of the inflow

Let us now explore the details of the saturation mechanism. Saturation occurs when the magnetic pressure in the sheet becomes comparable to the hydromagnetic pressures at the edge of the reconnection region. Since the total pressure is expected

to be near uniform in the vicinity of the neutral point—and the dynamic pressure of the inflow must be small close to the stagnation point—the build up in magnetic intensity effectively "drives a hole" in the gas pressure. It follows that the flux pile-up layer will be characterised by highly non-uniform conditions in which the plasma pressure varies out of phase with the magnetic field intensity.

Our equations do not have any explicit gas pressure dependence, since we use the curled form of the momentum equation. However, referring back to the primitive form allows us to formulate a Poisson equation for the gas pressure p. This in turn allows us to calculate the gas pressure a posteriori—at least to within an additive constant.

Figure 5.3 depicts two cross sections of the gas pressure taken along the inflow axis. The top plot is taken in the pre-saturation regime and shows only a modest pressure drop in the flux pile-up region. The lower plot is fully saturated and a deep well in the gas pressure has developed.

The fact that the gas pressure is minimum close to the magnetic peak provides a key predictor for the onset of saturation. This follows from the fact that the gas pressure at the neutral point p_0 must, by continuity, be of the same order of magnitude as the hydromagnetic pressure in regions external to the sheet. Thus if Π_E represents a characteristic hydromagnetic pressure in the advection region external to the sheet, we must have $\Pi_E > \frac{1}{2}B^2_{\text{sheet}}$ for all values of η. It follows that stalling occurs when the magnetic pressure of the sheet approaches Π_E (Craig and Watson, 2000b).

Although we have considered only incompressible merging, the previous arguments are valid in plasmas of arbitrary compressibility. In this case the gas pressure hole at the current sheet will lead to a hole in the density—a near vacuum region—close to the neutral point. This may well signal a breakdown of the collisional MHD approximation near the neutral point. To what extent such non-collisional conditions modify the detailed dynamics of the merging process is largely unknown. However, since the plasma resistivity in the sheet is likely to be enhanced by factors of 10^4 or more (Parker, 1994), we expect purely collisional models to be conservative in estimating the ultimate energy conversion rate.

5.2.2 Saturation scalings

Suppose some saturated level B^*_{sheet} is attained for a coronal resistivity $\eta = \eta_c$. If we use $W_\eta \simeq \eta B^2_{\text{sheet}}/l$ as an estimate for the Ohmic dissipation rate we find that

$$W_{\eta_c} \simeq \eta_c^{1/2} B^{*2}_{\text{sheet}}$$

determines the saturated rate in the case of a fixed inflow. However, this simple argument neglects the fact that the increasing field in the current layer can, under

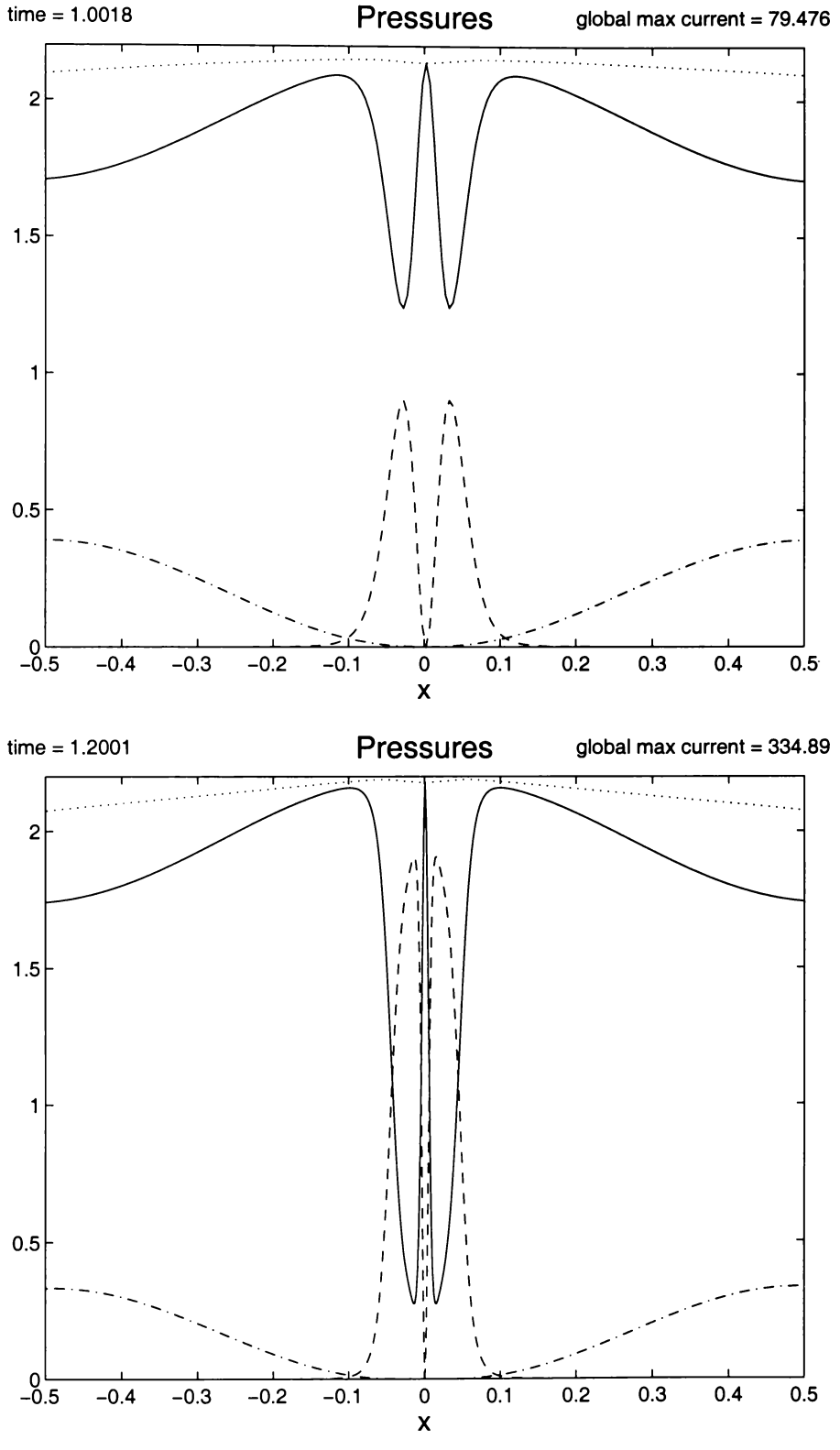

Figure 5.3: Plots showing the magnetic (dashed), hydrodynamic (dash-dot), gas pressures (solid), and the total pressure (dotted) at the time of maximum current. The gas pressure has been normalised with respect to the peak magnetic pressure. The top plot, $\eta = 10^{-3}$ shows a solution prior to the onset of saturation, while the solution shown in the lower plot is fully saturated with $\eta = 10^{-4}$. In both cases $g_0 = 0.19$.

quasi-steady conditions, drive enhanced exhaust flows in the sheet. Recent work (Litvinenko and Craig, 1999; Craig and Watson, 2000b) has investigated the effects of saturation and pressure equalisation on the energy dissipation rate. We will now summarise these results in the present context.

Consider the magnetic flux washed into a sheet by the flow $\mathbf{v} = \alpha(-x, y)$. On the inflow boundary ($x = 1$) we have

$$\mathcal{F} = \alpha B_1 \ , \tag{5.8}$$

where B_1 is the magnetic field on the inflow boundary. Regarding $\mathcal{F}$ as fixed, we balance the speed of inflow into the sheet αx_{sheet} with the rate of diffusion η/x_{sheet} at the edge of the current sheet. This gives

$$x_{\text{sheet}} \simeq \left(\frac{\eta}{\alpha}\right)^{1/2} \tag{5.9}$$

We also know that $B(x) \simeq B_1/x$ in the far field, from the asymptotics of the Dawson function solution (see Section 3.2.2). Hence at the edge of the sheet we have

$$B_{\text{sheet}} \simeq \frac{B_1}{x_{\text{sheet}}} \ . \tag{5.10}$$

The pressure equalisation condition now states that the inflow and outflow pressures have had time to equalise. In other words

$$\frac{\rho v_{\text{out}}^2}{2} = \frac{B_{\text{sheet}}^2}{2} \ ,$$

which is of course just the standard Sweet-Parker assumption (2.31). We satisfy the equalisation condition by setting

$$\alpha = B_{\text{sheet}} \ . \tag{5.11}$$

Equations (5.10) and (5.8) then imply

$$B_{\text{sheet}} \simeq \frac{\mathcal{F}}{\alpha x_{\text{sheet}}} \ .$$

Substituting for x_{sheet} and α from (5.9) and (5.11), this becomes

$$B_{\text{sheet}} \simeq \eta^{-1/3} \mathcal{F}^{2/3} \ . \tag{5.12}$$

Next we need to find x_{sheet}. Substituting (5.11) into (5.9) gives

$$x_{\text{sheet}} \simeq \eta^{1/2} B_{\text{sheet}}^{-1/2} \ .$$

Eliminating B_{sheet} from this using (5.12), we have

$$x_{\text{sheet}} \simeq \eta^{2/3} \mathcal{F}^{-1/3} \ . \tag{5.13}$$

We can now deduce the equalised Ohmic dissipation rate from

$$W_\eta \simeq \eta \left(\frac{B_{\rm sheet}}{x_{\rm sheet}} \right)^2 L^2 x_{\rm sheet} \ . \tag{5.14}$$

Thus for fixed flux we have the following scalings for equalised merging.

$$x_{\rm sheet} \sim \eta^{2/3} \ , \quad B_{\rm sheet} \sim \eta^{-1/3} \ , \quad W_\eta \sim \eta^{-1/3} \tag{5.15}$$

We can now saturate the field at some level $B^*_{\rm sheet}$ for $\eta = \eta_c$. From (5.12) it is clear that the saturated flux is given by

$$\mathcal{F}^* = \eta_c^{1/2} B^{*3/2}_{\rm sheet} \ . \tag{5.16}$$

Using (5.13) and (5.14) we can derive the equalised/saturated dissipation scaling

$$W_\eta \simeq \eta_c^{1/2} B^{*5/2}_{\rm sheet} \ . \tag{5.17}$$

Combining the above equalised result with the earlier non-equalised result, it follows that in general the maximum dissipation rate must satisfy

$$\eta_c^{1/2} B^{*2}_{\rm sheet} \leq W_{\eta_c} \leq \eta_c^{1/2} B^{*5/2}_{\rm sheet} \ . \tag{5.18}$$

For the "driven" simulations considered here and in Chapter 4, the lower bound seems appropriate, since the rapid formation of the current layer (on an Alfvénic time-scale) allows little possibility for pressure equalisation between the field and the flow. In other circumstances, for instance reconnection driven by the gradual emergence of the nonlinear coalescence instability, the upper bound can be attained (see Craig and Watson (2000a)).

5.2.3 Numerical scaling results

Numerical simulations, using the same periodic 2-D code as in Section 4.1, confirm the inequality (5.7). Figure 5.4 shows two sets of pile-up fields initially growing with reductions in η as predicted by (5.5). However, we can see that the peak magnetic fields saturate when $B_{\rm sheet} \simeq 1$, consistent with (5.7) since $B_{\rm inflow} \simeq v_{\rm inflow} \simeq 1$.

Given the above results for the saturation of the magnetic field, we would expect the Ohmic dissipation to change to the slow $W_\eta \sim \eta^{1/2}$ rate for small enough values of η. Figure (5.5) shows the results of two scaling runs where the Ohmic dissipation is "fast" for sufficiently large values of the resistivity, but the scaling tails over and becomes slow once η is reduced below a critical level.

Figure (5.5) also shows how the size of the magnetic disturbance field affects the level of resistivity at which saturation sets in. Clearly a large disturbance saturates

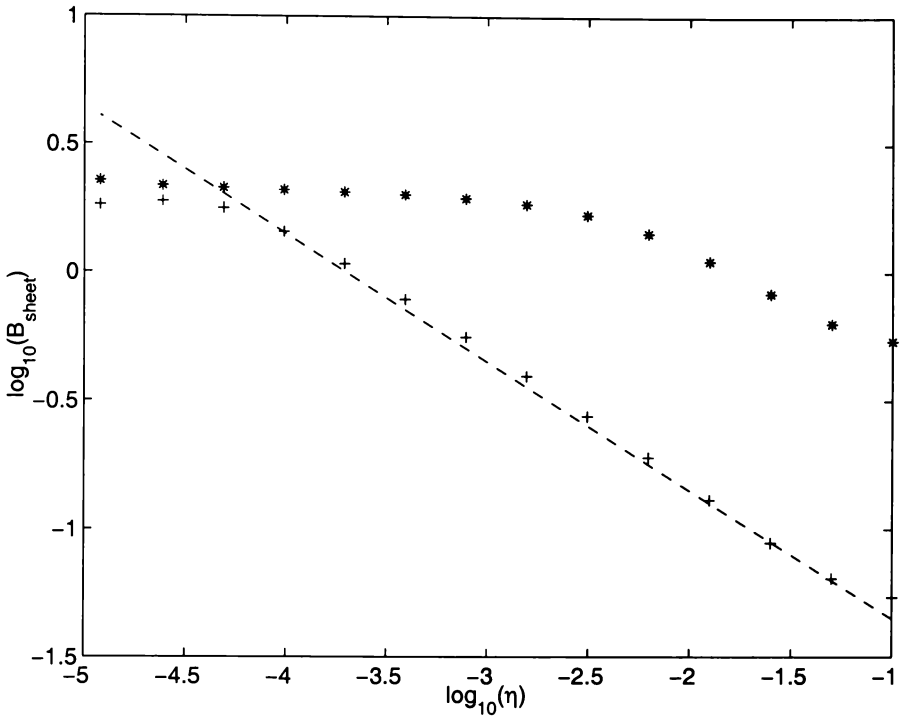

Figure 5.4: Two scaling runs for different values of the disturbance amplitude. The asterisks use $g_0 = 0.6$, while the pluses represent runs with $g_0 = 0.06$. Both runs represent a purely 1-D initial disturbance ($\beta_0 = 0$) and use a resolution which ensures at least 8 grid points reside inside the current layer for each value of η, except for the three smallest values of η for which resolution is compromised. All runs use $\nu = \eta$. Note that the $g_0 = 0.06$ runs correspond to those of Figure 4.3.

for a larger value of η than a comparatively small disturbance does, since the build-up rate is the same in both cases (see Figure 5.4). So by taking a sufficiently small disturbance field we can always ensure that we are in the "fast" regime for a given η. Conversely, given a disturbance we can always ensure "fast" reconnection by choosing a high level of resistivity. However, in terms of total energy liberation, maximizing the $W_\eta \sim \eta^{1/2}$ scaling appears to be the best we can do.

5.2.4 Saturation summary

At first sight it may appear that, due to saturation, the more sophisticated and analytically exact solutions of Sections 3.2 and 3.3 have no advantage over heuristic models such as Sweet-Parker when comparing saturated Ohmic dissipation rates. However, some flux pile-up will always occur. It should also be remembered that the pressure driving the merging will in general far exceed typical coronal pressures, since the driving source of the merging is likely to come from deeper down into the Sun. Hence a pile-up field of $B_{\text{sheet}} = 10B_{\text{inflow}} \simeq 1000\text{G}$ is quite plausible,

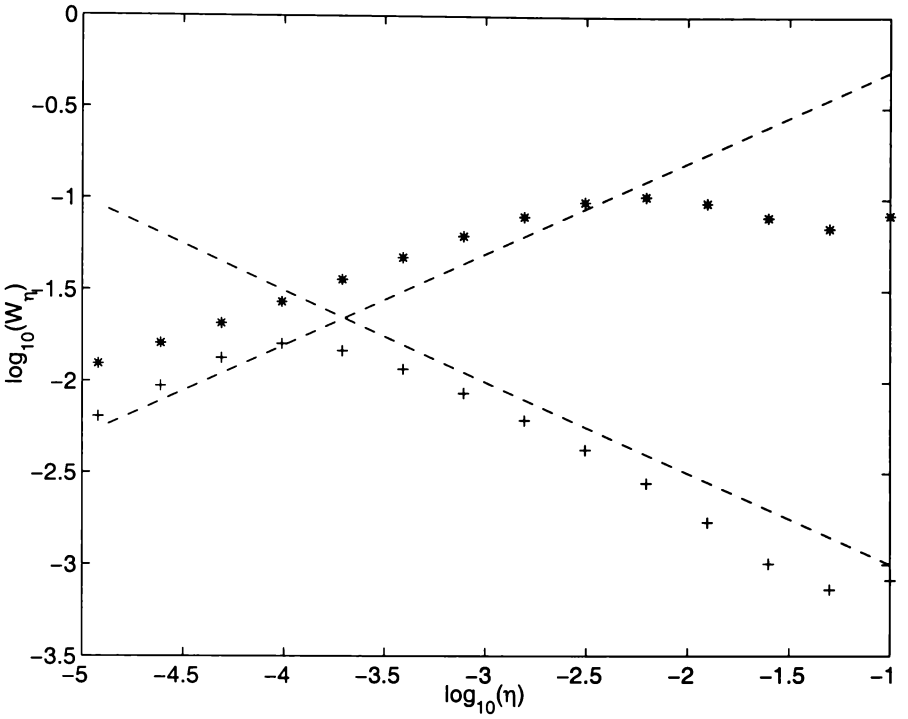

Figure 5.5: Plots showing how the Ohmic dissipation rate W_η (measured at the time of maximum current) scales with resistivity η for two disturbance field amplitudes. The dotted reference line of positive slope represents the Sweet-Parker scaling $W_\eta \sim \eta^{1/2}$, while the second dotted line shows the fast $W_\eta \sim \eta^{-1/2}$ scaling. Both runs represent a purely 1-D initial disturbance and use a resolution which ensures at least 8 grid points reside inside the current layer for each value of η, except for the three smallest values of η for which resolution is compromised. All runs use $\nu = \eta$.

since the pressure associated with sunspot fields ($\sim$ 3000G), which form the bases of coronal loops, is still an order of magnitude greater than the resulting sheet pressure. From the inequality (5.18) the Ohmic dissipation rate will then be 100 times greater than the corresponding Sweet-Parker rate (up to 3 times more if equalisation occurs). The other important factor to consider is that in the case of equalised merging the sheet width scales as $l \sim \eta^{2/3}$, considerably narrower than the standard $l \sim \eta^{1/2}$ scaling. This means that an anomalous resistivity, which arises when the sheet width approaches the particle mean free path, develops sooner. As we will discuss in Chapter 7, anomalous resistivity can enhance dissipation by many orders of magnitude. However, the sheet dynamics cannot really be understood in terms of the MHD analysis of this section once anomalous effects are present.

5.3 Compressibility

In this section we examine the effects of finite compressibility on the magnetic merging process. The previous work in this thesis, along with the vast majority of reconnection studies, has focused exclusively on the incompressible fluid approximation. The opposite assumption, that of arbitrary compressibility, has been studied in the past (Craig and Watson, 1992; Craig and McClymont, 1991). What this work shows is that when the density is sufficiently low, magnetic field tends to reconnect on an Alfvénic time scale. However this limit provides little insight into the nature of compressible reconnection since the field cannot "feed back" on the flow.

One aspect of finite compressibility, as opposed to incompressible and arbitrarily compressible approximations, is the presence of a multitude of wave phenomena. A magnetic field has waves associated with it due to magnetic tension in the field lines. These are known as Alfvén waves. When a compressible fluid is added, magnetic pressure forces will also generate waves. Such waves in general combine to give rise to slow and fast magnetoacoustic waves (see for example Priest (1984)). A compressible fluid of course has it's own wave structure. Small amplitude waves will travel at the sound speed (5.21), while finite amplitude disturbances generate shocks. In a conducting fluid these effects may couple together to give rise to slow and fast magnetoacoustic shocks.

The work in this section is mainly based around a 2-D time dependent numerical code which works with the velocity field, magnetic field, and density as its primitive variables. For the pressure we use the adiabatic approximation $p = \beta_p \rho^\gamma$, with $\gamma = 5/3$ and where the plasma beta β_p determines the level of compressibility. The major difficulty with numerical calculations involving finite compressibility is that shocks may now develop, as described above. The upshot of this is that numerical finite difference solutions with a spatial order of two or higher develop Gibb's overshoot phenomena.

5.3.1 Suppressing numerical overshoot

The Gibb's overshoot phenomenon is a problem common to all spatially second order and greater finite difference solutions of compressible fluid systems and appears as narrow spikes which will envelop the true solution if left unchecked. There are several ways to combat the inaccuracies generated by overshoot. The first is to use a scheme which is only first-order accurate. However, an ambiguity arises whether to take left or right derivatives. In advective problems it is important to take first order derivatives "upwind", since "downwind" schemes are unstable. Schemes exist (Thompson, 1986) which guarantee upwindedness in one dimension, however in the coupled systems we consider, they have limited success.

A second option is to use a standard 2-D second order scheme combined with a "pseudo-viscosity" which acts to dampen out the highly localised spikes associated with overshoot phenomena (see for example Richtmyer and Morton (1967) or Potter (1973)). Although the coefficient of pseudo-viscosity is of order unity, some experimentation is required to achieve satisfactory results. Unfortunately narrow current structures present in all our numerical experiments will also tend to be dampened, making it difficult to do self consistent runs.

A third method, which we utilise in our numerical simulations, is flux corrected transport (FCT) (see Zalesak (1979)). This method is by far the most sophisticated and involves calculating a "low-order" (or highly diffused) solution which is deemed to have the correct "shape". This solution is then "anti-diffused" towards a higher order solution in such a way that no new maxima or minima (spurious effects) are introduced. In practice we find that this method, as implemented, does not produce perfect results for the coupled system we consider. However, it produces the most reliable results out of the three methods considered here and all our numerical results were obtained using the FCT algorithm.

5.3.2 Numerical results

The numerical simulations considered here are very similar to the 2-D periodic calculations of Section 4.1. The initial configuration,

$$\phi(x,y) = \sin(\pi x)\sin(\pi y)/\pi, \tag{5.19}$$

$$\psi(x,y) = g_0 \cos(\pi x)/\pi\ , \tag{5.20}$$

comprises of four rotating velocity cells with anti-parallel magnetic field along the inflow axis and a uniform density. Allowing this configuration to evolve with time we see a current sheet forming along the y-axis, much the same as in the incompressible case (see for example Figure 4.1). The major difference is that we now have sound waves traveling through the box, with amplitude and frequency dependent on the plasma beta.

Figure 5.6 shows the configuration at the time of maximum current when $\beta_p = 1$. The results are very similar to the incompressible results of Section 4.1, except that there is now some density fluctuation. Figure 5.7 shows a similar run where we have used $\beta_p = 0.01$. The magnetic field localises sooner (see time diagnostics below) since the gas pressure does not have time to feed back on the inflow. The high compressibility of this configuration is evident by the large density accumulating at the fluid cell boundaries.

To allow a better interpretation of the dynamics of compressible merging, we track several diagnostic quantities over time from the starting configuration to well

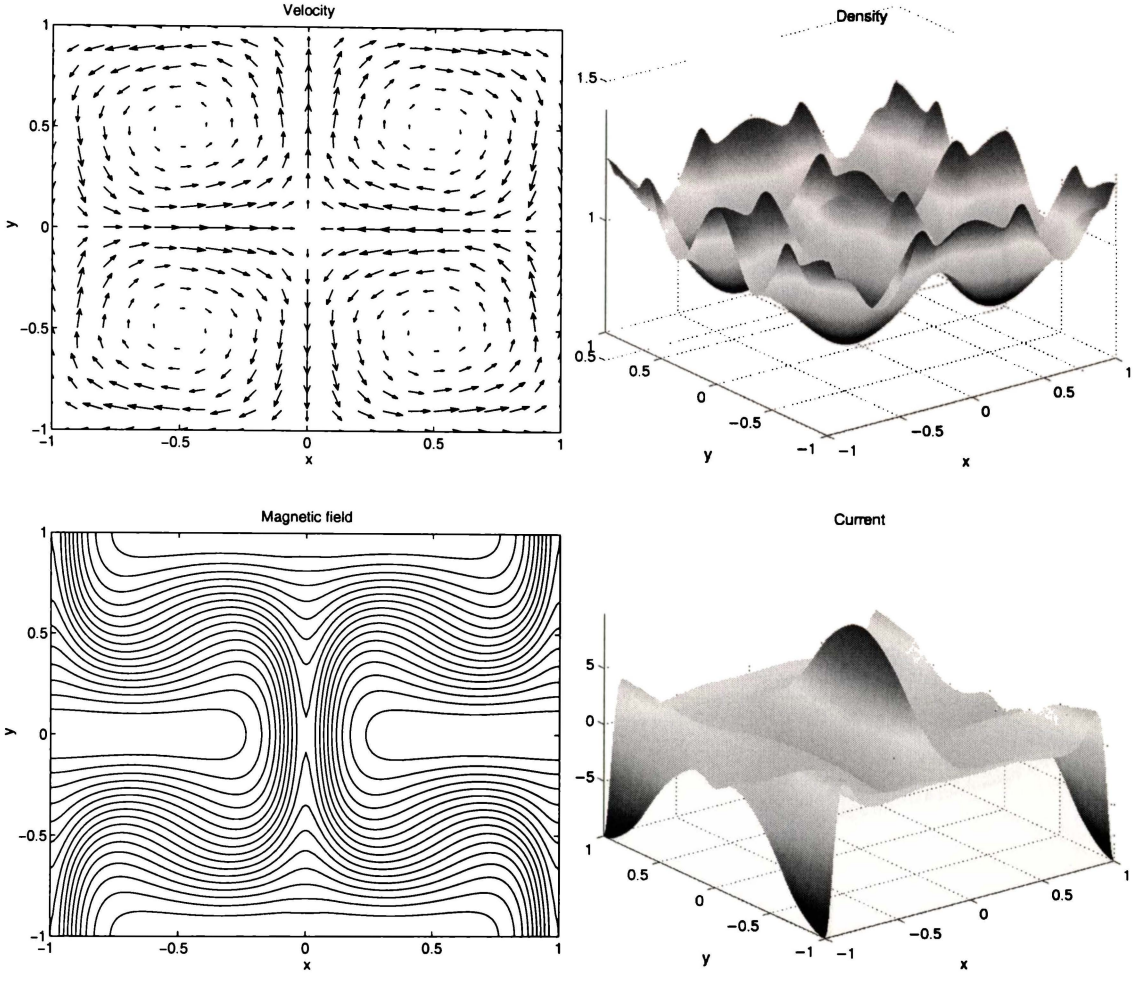

Figure 5.6: Results for compressible run with $\beta_p = 1$ and $g_0 = 0.2$.

after the central current sheet has dissipated. These quantities are: the Ohmic dissipation W_η (integrated over the entire box), current density at the center of the current sheet J_0, peak magnetic field at the sheet B_{sheet}, minimum and maximum density $\rho_{\min}$ and $\rho_{\max}$. In all runs we have used $\eta = \nu = 0.01$ and the disturbance amplitude $g_0 = 0.2$. Using $\beta_p = 100$ to approximate incompressibility we have the plot shown in Figure 5.8.

In Figure 5.9 we show the current trace for the equivalent run obtained from the 2-D incompressible code used in Sections 4.1, 5.1, 5.2 and 5.5, superposed with the $\beta_p = 100$ compressible results. The curves are almost indistinguishable and confirm that the code behaves as expected, at least in the weakly compressible limit.

Let us now systematically reduce β_p. Of interest is the "intermediate" phase between nearly incompressible and highly compressible solutions, where wave phenomena distort the diagnostic values measured. The frequency of these waves decreases with β_p and for $\beta_p < 1$ the anomalies disappear since the localisation time is

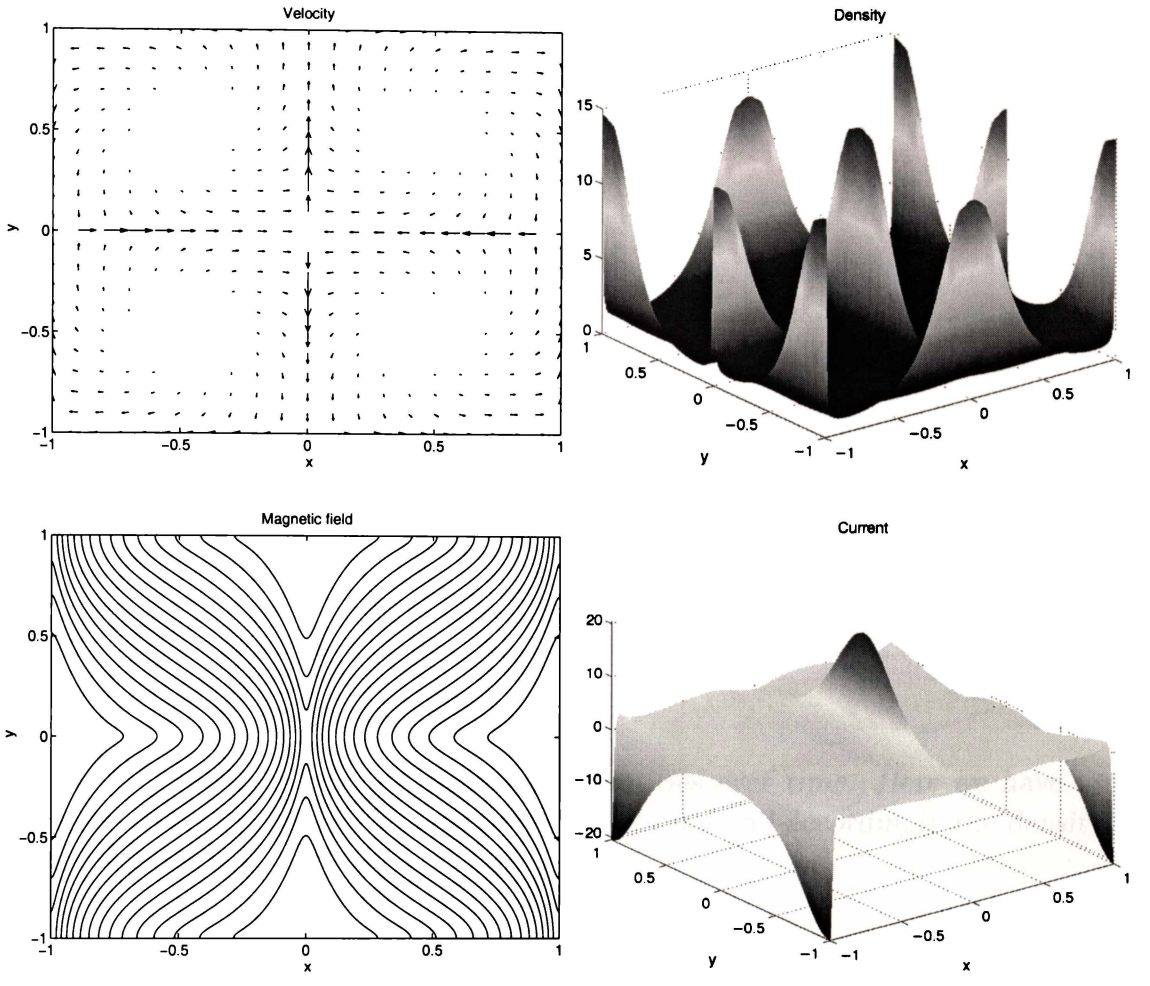

Figure 5.7: Results for compressible run with $\beta_p = 0.01$ and $g_0 = 0.2$. Note the huge density forming between the rotating fluid cells.

less than the time for a density wave to travel through the box. In other words, the sound speed exceeds the Alfvén speed (see equation (5.22) and discussion below). During the intermediate phase these waves cause distortions because their speed is comparable to the current sheet localisation speed and as such they compress and rarefy the sheet, generating higher or lower currents at these times than may otherwise be expected, depending on whether the sound waves reinforce or cancel out the localisation velocity. This effect makes it impossible to do unambiguous scaling runs with respect to β_p for plasma betas of order 1, since these density fluctuations alter the diagnostic quantities in unpredictable ways.

The wave phenomena present in all these runs are due to an equalisation of the pressure during the collapse. The speed at which "information" travels is equal to the sound speed given by

$$c_s = \left(\frac{\partial p}{\partial \rho}\right)^{1/2} \tag{5.21}$$

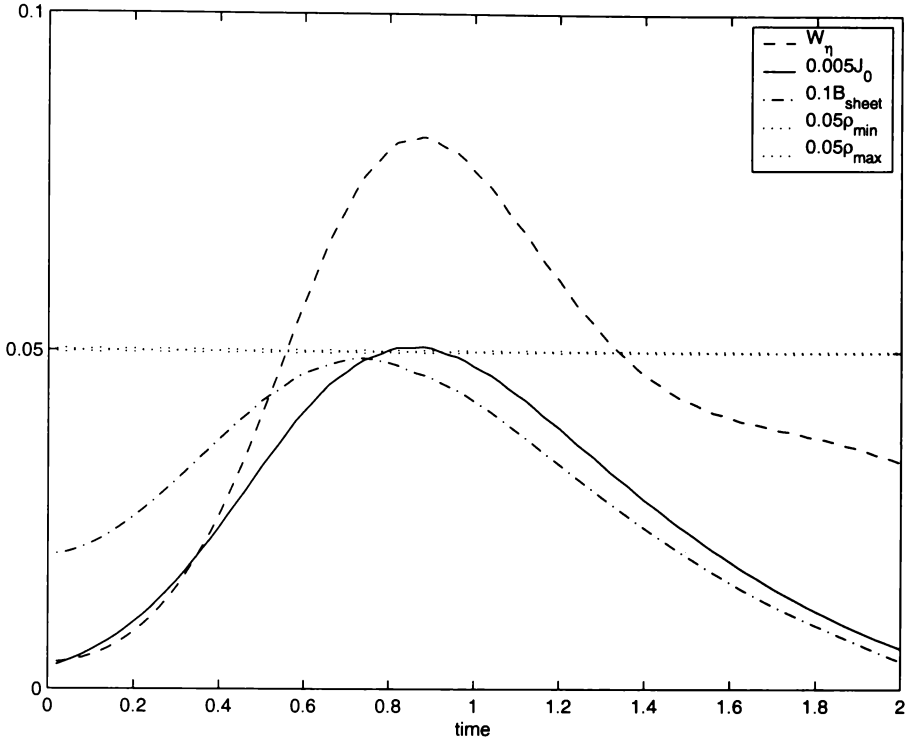

Figure 5.8: Traces of various diagnostic quantities over time. Here we have used $\beta_p = 100$ to approximate an incompressible solution and accordingly the density is almost constant.

In the present adiabatic approximation (using $\gamma = 5/3$), we expect the time for a density wave to traverse the distance from the boundary to the current sheet to be

$$t \simeq \frac{\bar{\rho}^{(1-\gamma)/2}}{\sqrt{\gamma \beta_p}}, \tag{5.22}$$

where $\bar{\rho}$ represents the average density. The frequency of the waves in the plots seems to agree with this prediction for large β_p where $\rho \simeq 1$, while for smaller values of plasma beta the times are less than the prediction (5.22) due to the density inhomogeneities.

The last few plots, with $\beta_p < 0.3$, represent runs where the current sheet forms and dissipates over a shorter time scale than the typical sound travel time. This has the effect of the current sheet forming without the rest of the plasma "knowing" about it. Over this time scale the plasma is effectively "arbitrarily compressible" and we may expect a thinner current sheet to result as gas inside the current sheet is compressed without "feed-back". Indeed the plots do show the current increasing as β_p is reduced. Since $J \simeq B_{\text{sheet}}/l$, and B_{sheet} remains roughly constant, we deduce that a thinning of the sheet, rather than a build up of the field, is responsible for the intensified current.

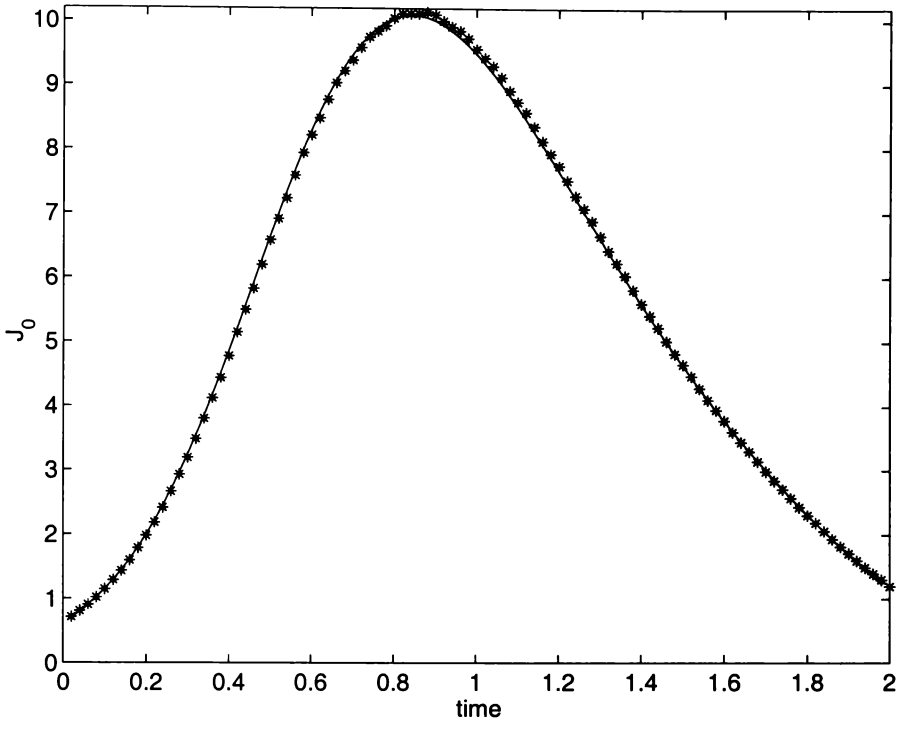

Figure 5.9: Maximum current trace obtained from incompressible code (solid), superposed with the current obtained from the compressible code (asterisks) using $\beta_p = 100$.

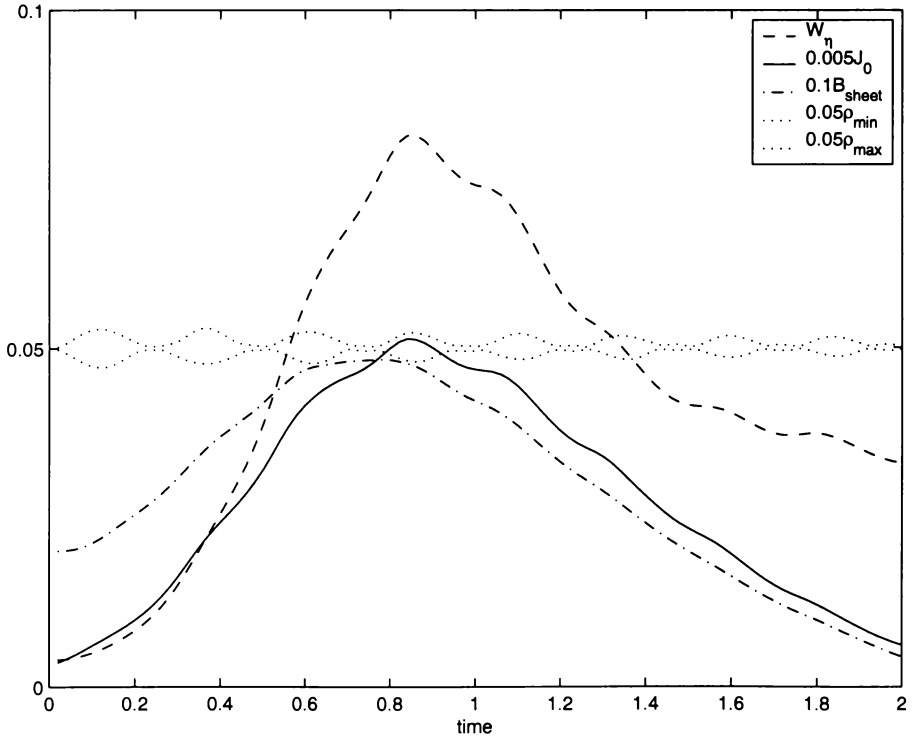

Figure 5.10: Traces for $\beta_p = 10$ *solved on a* 160×160 *grid.*

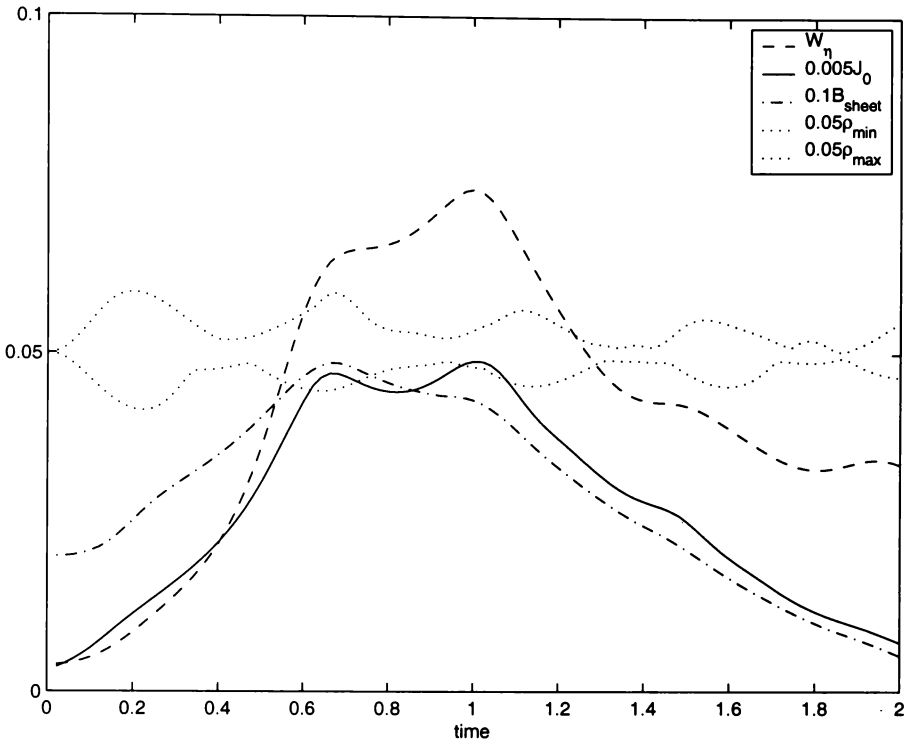

Figure 5.11: Traces for $\beta_p = 3$ solved on a 160 × 160 grid.

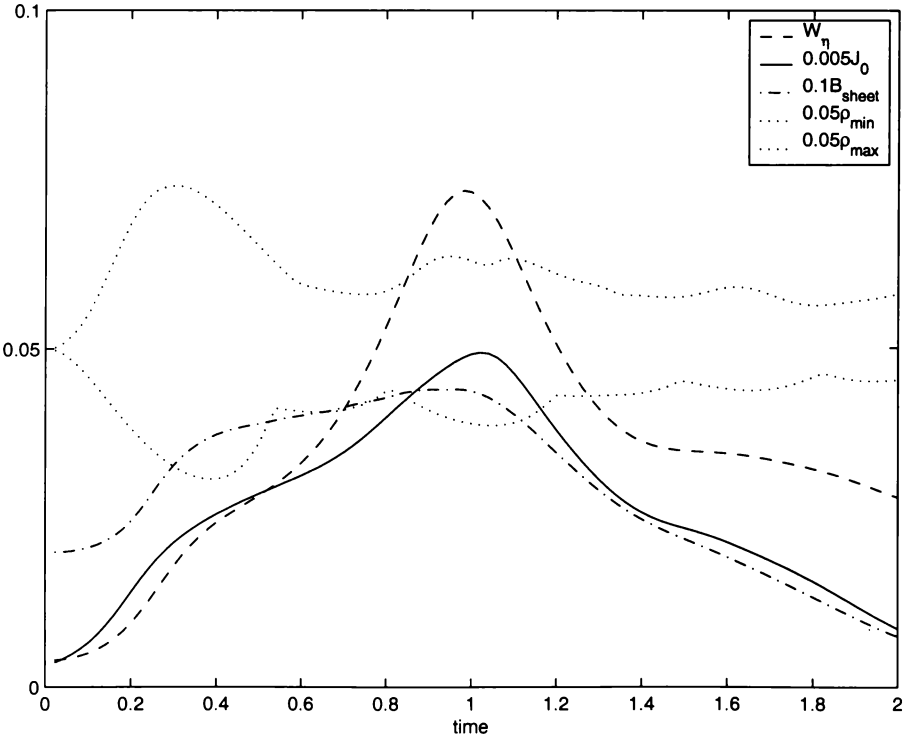

Figure 5.12: Traces for $\beta_p = 1$ solved on a 160 × 160 grid.

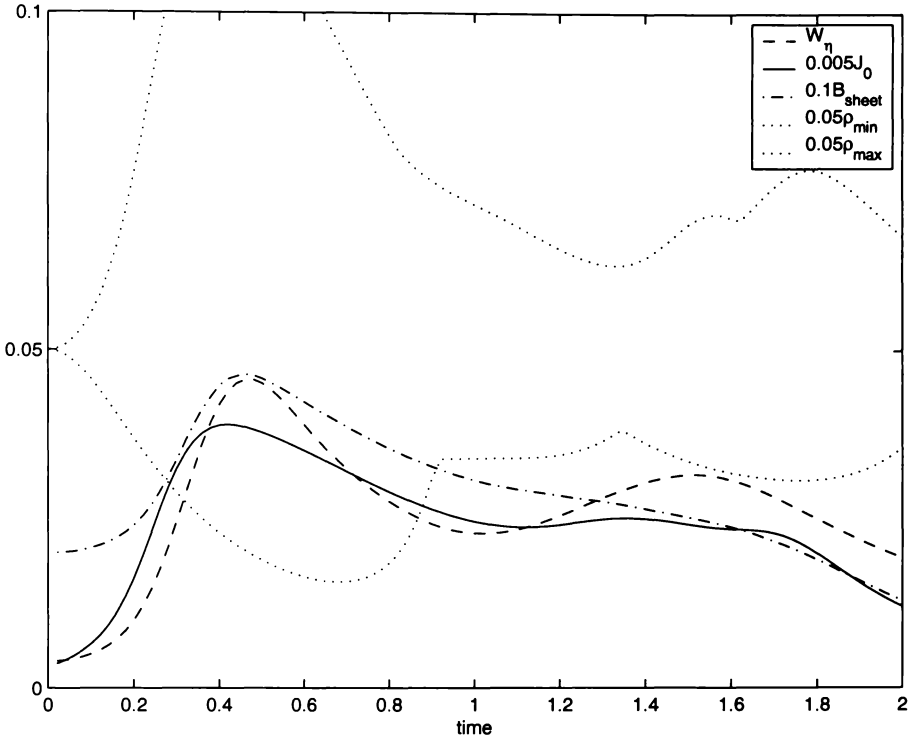

Figure 5.13: Traces for $\beta_p = 0.3$ solved on a 240 × 240 grid. Maximum density achieved is 2.4 (0.12 on this scale).

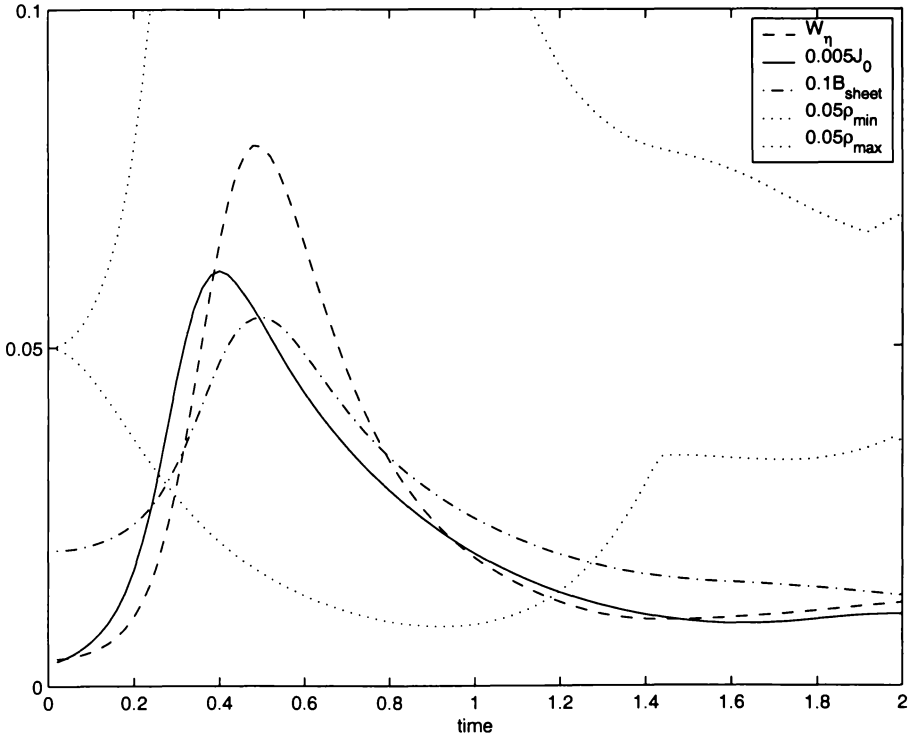

Figure 5.14: Traces for $\beta_p = 0.1$ solved on a 480 × 480 grid. Maximum density achieved is 4.3 (0.22 on this scale).

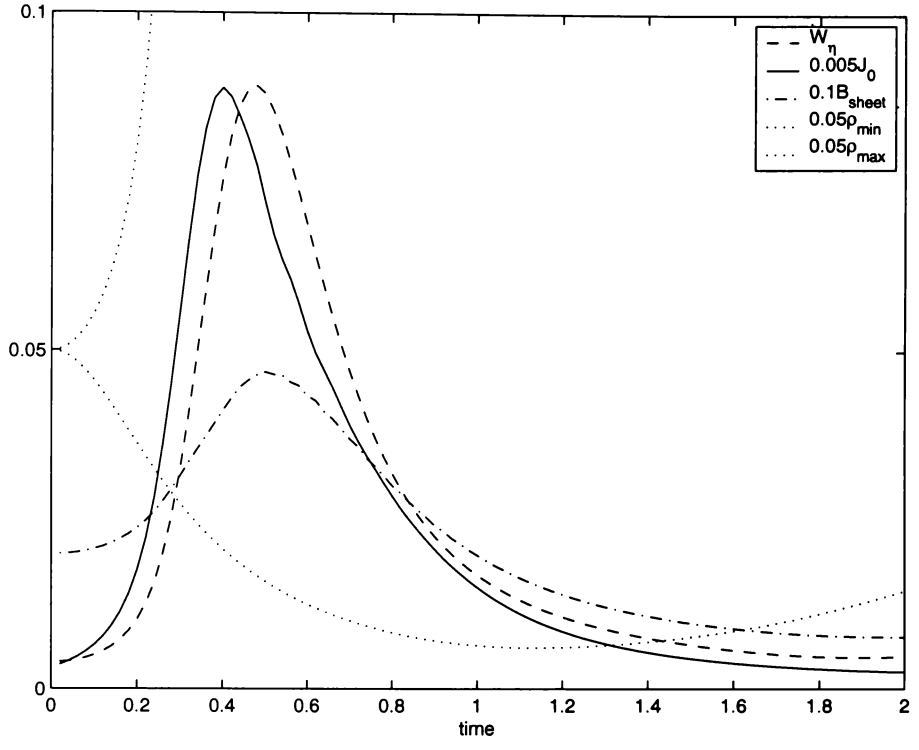

Figure 5.15: Traces for $\beta_p = 0.03$ solved on a 480 × 480 grid. Maximum density achieved is 9.0 (0.45 on this scale).

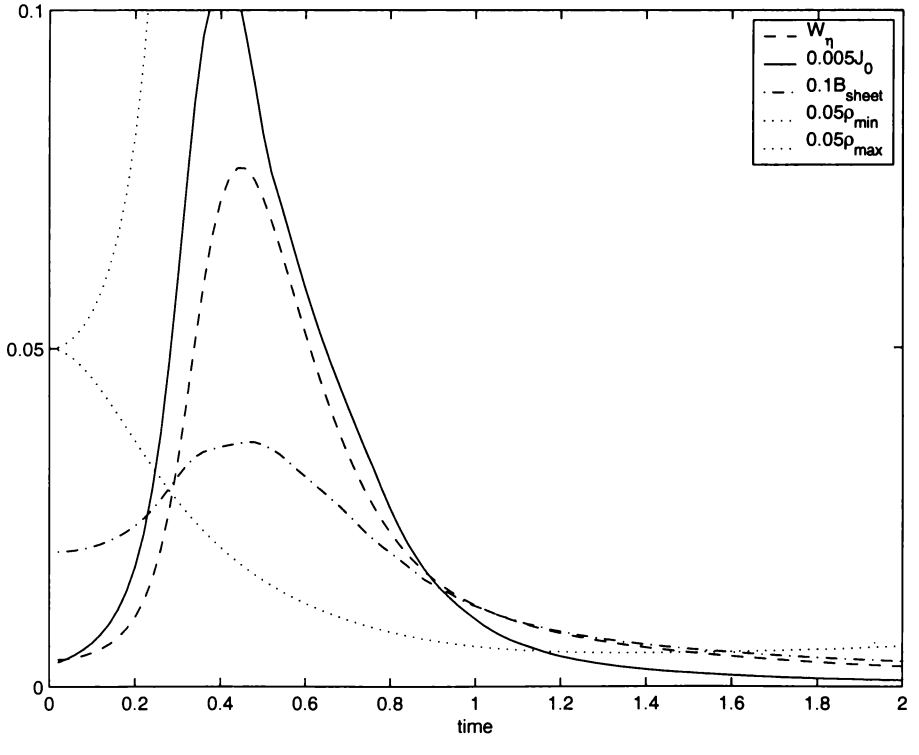

Figure 5.16: Traces for $\beta_p = 0.01$ solved on a 480 × 480 grid. Maximum density achieved is 17.6 (0.88 on this scale).

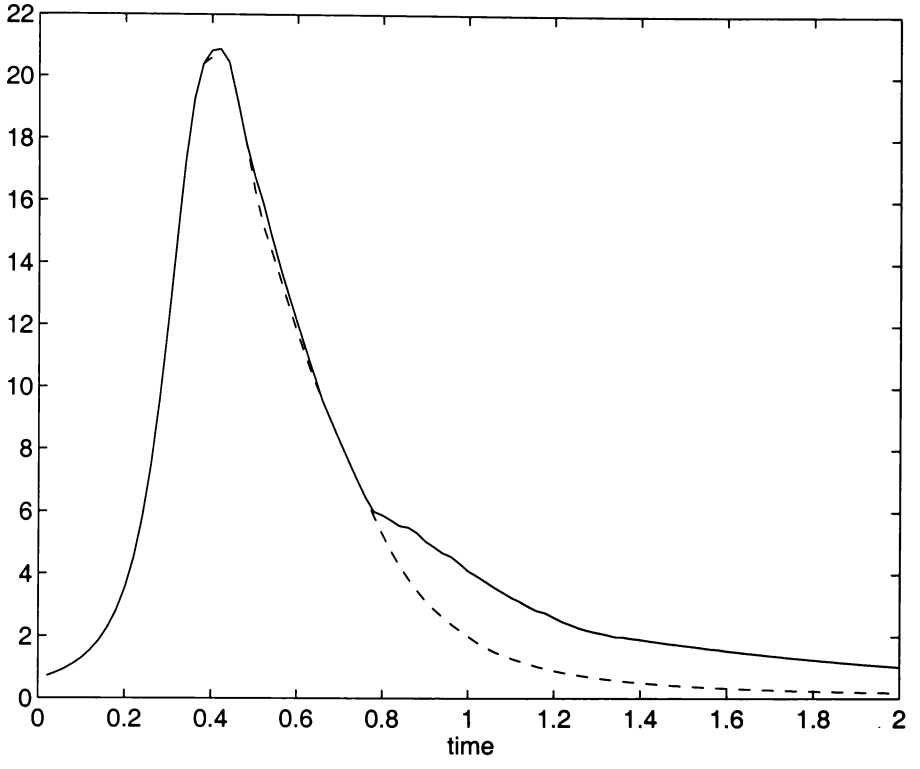

Figure 5.17: Traces of current density at the middle of the central sheet (dashed) and maximum current density over the domain. Here $\beta_p = 0.01$ and we solve on a 480 × 480 grid as in Figure 5.16. Note inconsistent behaviour of the maximum current as the sheet dissipates away (see text).

The work presented in this section gives only a flavour of what happens when the incompressible assumption is relaxed. The numerical difficulties are many and even the best version of the code seems unable to stop artifacts from contaminating the solution for sufficiently small β_p. Figure 5.17 shows a run for $\beta_p = 0.01$ where we trace the current at the origin and the global maximum current. Due to the symmetries present in the problem we would expect these to be identical until a new current sheet forms at $y = \pm 1$. The fact that they don't agree indicates that a non-systematic "spikiness" has developed in the solution, presumably due to numerical inaccuracy. Overall, the results show complicated effects related to density waves not present in the incompressible work. The key finding of this section is that the Ohmic dissipation (integrated over the entire domain) and the maximum pile-up field remain approximately constant as the plasma becomes more compressible. The results of this section show that the incompressible approximation captures the main features of moderately compressible merging in terms of field build-up and dissipation. In general, however, compressible current sheets will tend to be narrower and more intense than their incompressible counterparts. In practice this means that anomalous effects develop at lower values of resistivity than the incompressible results suggest, giving compressible solutions a greater capacity for energy liberation.

5.4 Osculation

Traditional reconnection studies have tended to concentrate only on head-on (strictly anti-parallel field) reconnection. In such cases it has been argued (Priest and Cowley, 1975; Biskamp, 1994) that separatrix field lines meeting at the neutral point should osculate rather than form a narrow X-point (see Figure 5.18). Since this means that the linear component of the magnetic field perpendicular to the sheet vanishes, we expect osculation to be signaled by a *cubic* profile of this field component.

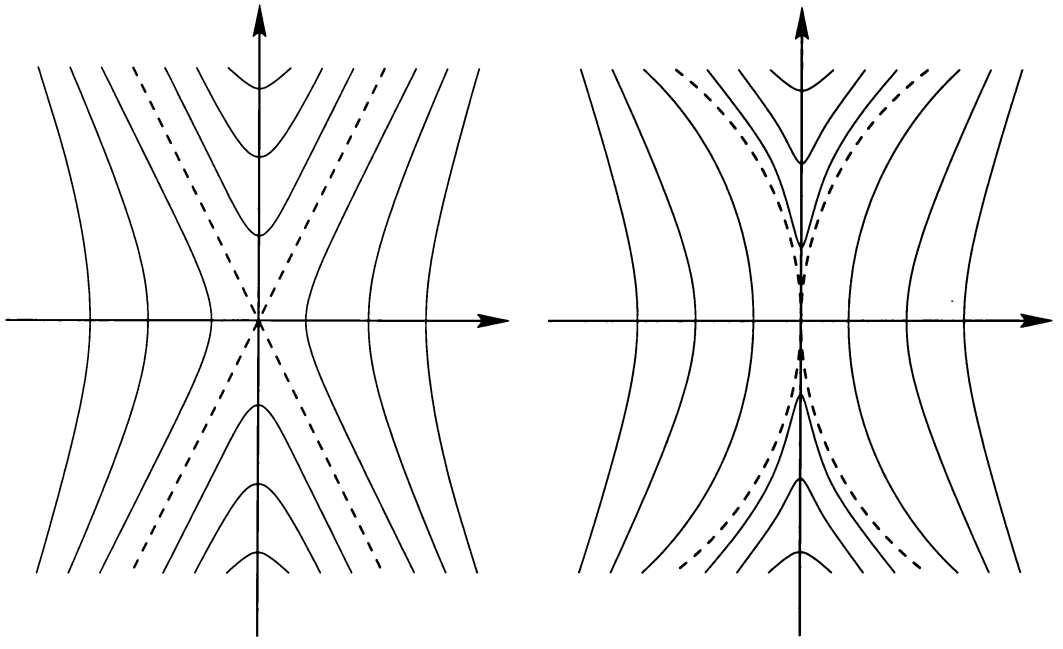

Figure 5.18: Schematics of a standard X-point on the left and a configuration where the separatrices (dashed) osculate on the right.

The argument is based on two-dimensional Taylor expansions for the stream function ϕ and flux function ψ about the stagnation/neutral point of the form

$$\phi(x,y,t) = \sum_{m,n} \phi_{2m+1,2n+1}(t) \frac{x^{2m+1} y^{2n+1}}{(2m+1)!(2n+1)!} , \tag{5.23}$$

$$\psi(x,y,t) = \sum_{m,n} \psi_{2m,2n}(t) \frac{x^{2m} y^{2n}}{(2m)!(2n)!} . \tag{5.24}$$

If we substitute these forms into the planar incompressible viscous MHD equations given by

$$\nabla^2 \dot{\phi} + [\nabla^2 \phi, \phi] = [\nabla^2 \psi, \psi] + \nu \nabla^4 \phi \tag{5.25}$$

$$\dot{\psi} + [\psi, \phi] = \eta \nabla^2 \psi , \tag{5.26}$$

we find that the induction equation (5.26) gives

$$\begin{aligned}\dot{\psi}_{00} &+ \dot{\psi}_{20}\frac{x^2}{2} + \dot{\psi}_{02}\frac{y^2}{2} + (\psi_{20}x)(\phi_{11}x) - (\psi_{02}y)(\phi_{11}y) \\ &= \eta\left(\psi_{20} + \psi_{02} + \psi_{40}\frac{x^2}{2} + \psi_{04}\frac{y^2}{2} + \psi_{22}\frac{y^2}{2} + \psi_{22}\frac{x^2}{2}\right) .\end{aligned}$$

Equating the various coefficients of x and y yields

$$\dot{\psi}_{00} = \eta(\psi_{20} + \psi_{02}) \tag{5.27}$$

$$\dot{\psi}_{20} = \eta(\psi_{40} + \psi_{22}) - 2\psi_{20}\phi_{11} \tag{5.28}$$

$$\dot{\psi}_{02} = \eta(\psi_{04} + \psi_{22}) + 2\psi_{02}\phi_{11} . \tag{5.29}$$

Repeating this for the momentum equation (5.25) we have that

$$\dot{\phi}_{31} + \dot{\phi}_{13} = \psi_{02}(\psi_{40} + \psi_{22}) - \psi_{20}(\psi_{04} + \psi_{22}) + \nu(\phi_{51} + 2\phi_{33} + \phi_{15}) , \tag{5.30}$$

which, on substituting for (5.28) and (5.29), gives

$$\eta(\dot{\phi}_{31} + \dot{\phi}_{13}) = \dot{\psi}_{20}\psi_{02} - \dot{\psi}_{02}\psi_{20} + 4\psi_{20}\psi_{02}\phi_{11} + \eta\nu(\phi_{51} + 2\phi_{33} + \phi_{15}) . \tag{5.31}$$

From this we can see that when time-dependence is eliminated we must have

$$0 = 4\psi_{20}\psi_{02}\phi_{11} + \eta\nu(\phi_{51} + 2\phi_{33} + \phi_{15}) . \tag{5.32}$$

Clearly $\nu = 0$ implies that either $\psi_{20} = 0$ or $\psi_{02} = 0$, since we want ϕ_{11}, our highest order flow term, to be non-zero. This then means that our X-point has collapsed and the field lines now osculate along the current sheet, so that the magnetic field perpendicular to the sheet should now increase cubicly (rather than linearly) with distance along the sheet. Alternatively we may take $\phi_{11} = 0$, however this does not fit in well with our driven merging models where strong flow drives weak fields together.

Although Biskamp (1994), on the basis of a viscous steady-state treatment, claims numerical evidence for osculation, we have found no numerical support for osculating current layers in the present time-dependent simulations. Typical head-on simulations (see Figure 5.2) confirm that the distribution of perpendicular magnetic field along the current sheet is linear rather than cubic. Given the numerical results of Biskamp, the natural assumption is that time-dependent effects are more damaging to osculation than finite viscosity. We have checked this interpretation by performing a series of simulations, for a range of resolutions, in which the level of fluid viscosity is systematically reduced. Figure 5.19 shows that the term $4\psi_{20}\psi_{02}\phi_{11}$ ($T4$) converges to a well defined limit of order unity as $\nu \to 0$, this term being balanced by the time-dependent terms ($T1$ and $T3$) of equation (5.31).

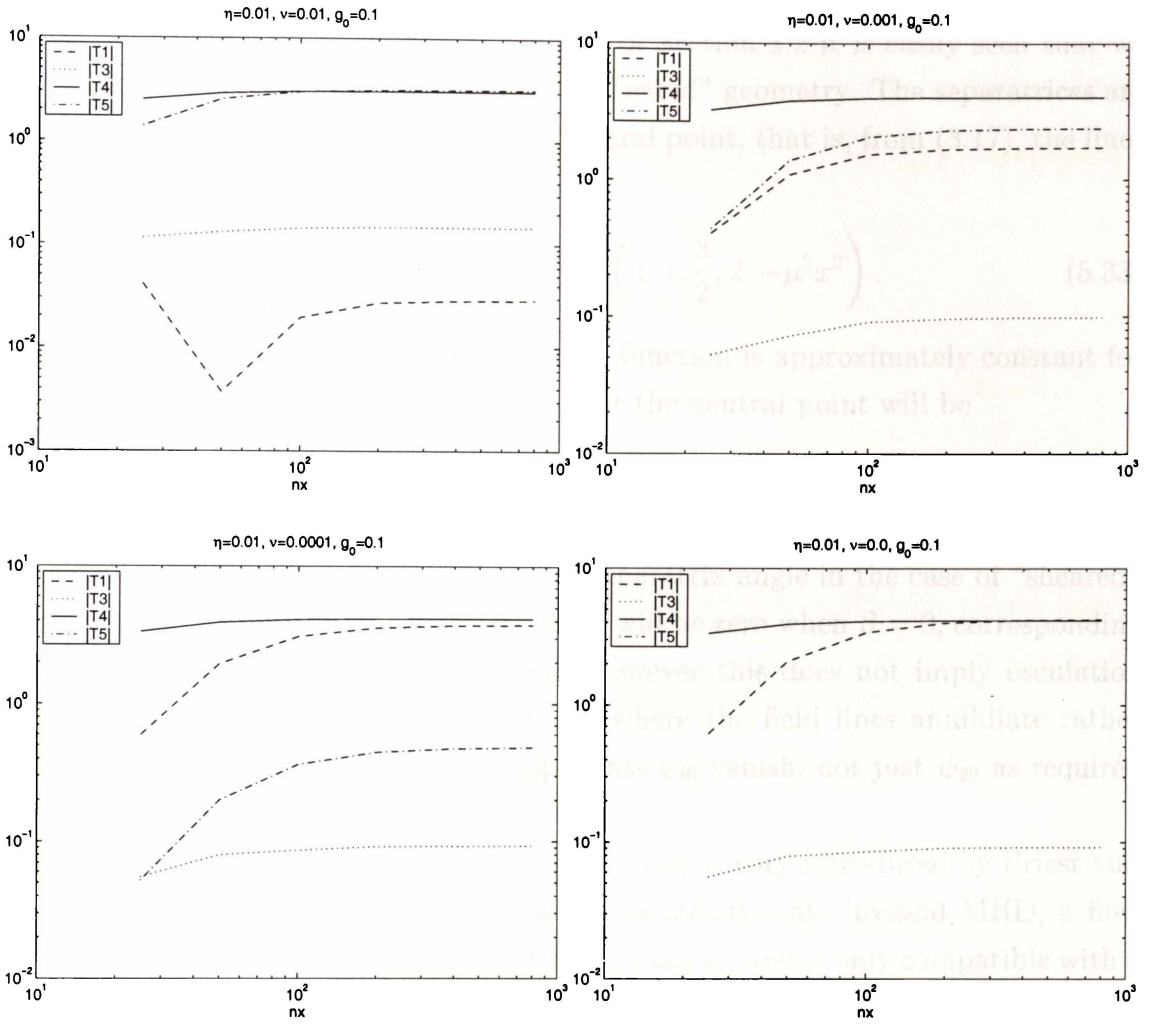

Figure 5.19: Numerical test for time-dependent osculation. Here we plot the absolute value of each of the terms in equation (5.31) for a range of numerical resolutions (nx is the number of grid points). It should be noted that term 2 is zero in all cases, at least to within the accuracy of the resolution used. Clearly as ν is reduced term 4 converges to a non-zero limit, determined by the time-dependent terms.

It is interesting to note the recent claim of Uzdensky and Kulsrud (1998) that the argument for osculation is theoretically flawed. They contend that for $\nu = 0$ the flow is no longer analytic at the neutral point and so the Taylor expansion (5.24) ceases to be valid. It seems likely, however, that their analytic and numerical analysis may be compromised by assuming *a specific form*, dictated by the Y-point Syrovatskii model (see Section 2.2.3), for the expansion close to neutral point. Certainly we know that well-behaved analytic inviscid solutions exist (Sonnerup and Priest (1975); see also Sections 2.2.4 and 3.2) for stagnation point flow ($\phi_{11} \neq 0$); however these do not include the higher order flow terms for which Uzdensky and Kulsrud find bad behaviour.

Finally we emphasise that osculation is generally a property of head-on merging. From the analytic Craig & Henton solution of Section 3.2 it is easily seen that we would not expect osculation to occur in a "sheared" geometry. The separatrices are given by the field lines which thread the neutral point, that is, from (3.17), the lines on which $\psi = 0$:

$$x = 0 \quad \text{and} \quad y = \frac{Ex}{2\beta\eta}\, {}_2\mathrm{F}_2\left(1, 1, \frac{3}{2}, 2, -\mu^2 x^2\right). \tag{5.33}$$

Using the property that the hypergeometric function is approximately constant for small values of x, the separatrix angle θ_{sep} at the neutral point will be

$$\theta_{\text{sep}} = \arctan\left(\frac{2\beta\eta}{E}\right). \tag{5.34}$$

The lower plot in Figure 5.1 shows a clear separatrix angle in the case of "sheared" reconnection. Of course the separatrix angle will be zero when $\beta = 0$, corresponding to the absence of the shear component. However this does not imply osculation since we now have an infinite neutral line where the field lines annihilate rather than reconnect, in other words all components ψ_{i0} vanish, not just ψ_{20} as required for osculation.

To summarise, we have revisited the osculation theory introduced by Priest and Cowley (1975). The analysis tells us that, for steady-state inviscid MHD, a flow which is of stagnation point form ($\phi_{11} \neq 0$) to leading order is only compatible with a magnetic field which is 1-D. We have shown, however, that including time dependent effects undoes this restriction, so that in general we would expect magnetic merging processes to generate a current sheet aligned to a finite angle X-point.

5.5 Tearing mode

Another feature of planar reconnection predicted by analytic theory is the appearance of the tearing mode instability in quasi-steady current sheets (Furth *et al.*, 1963; Finn and Sovinec, 1998; Priest and Forbes, 2000). The tearing mode produces small magnetic islands within the sheet that introduce further small length scales which lead to enhanced dissipation (see for example Spicer, 1977; van Hoven, 1981; Parker, 1979). Although the original analytic treatment suggests that the sheet becomes unstable when its aspect ratio exceeds about six to one, numerical simulations suggest much higher aspect ratios (Biskamp, 1994). Of course, reconnection simulations manifest phenomena not included in the original analytic theory of the tearing mode, for example the stabilising effect of strong shearing motions. The numerical evidence suggests however, that the tearing mode can develop in all current sheets with a sufficiently large aspect ratio (Biskamp suggests $\sim$ 100:1).

Biskamp (1993, 1994) performed a series of high resolution numerical experiments using a 2-D periodic spectral code to investigate MHD turbulence and the tearing mode instability. Our present aim is to provide an independent check using the finite difference code of Craig and Watson (1999), which we also used in Section 4.1, to verify the fragmentation of long current sheets.

5.5.1 Numerical results

We ran our code starting with the non-symmetric Orszag-Tang vortex initial condition

$$\phi(x,y) = \cos(\pi x + 1.4) + \cos(\pi y + 0.5) \tag{5.35}$$

$$\psi(x,y) = \cos(2\pi x + 2.3) + \cos(\pi y + 4.8) \tag{5.36}$$

and the parameter values $\eta = \nu = 5 \times 10^{-5}$ on a 2400×2400 mesh. These values mimic Biskamp (1994) except that whereas Biskamp claims to use a displacement of 4.1 in the second term of ψ, we find that only a displacement of 4.8 gives comparable results.

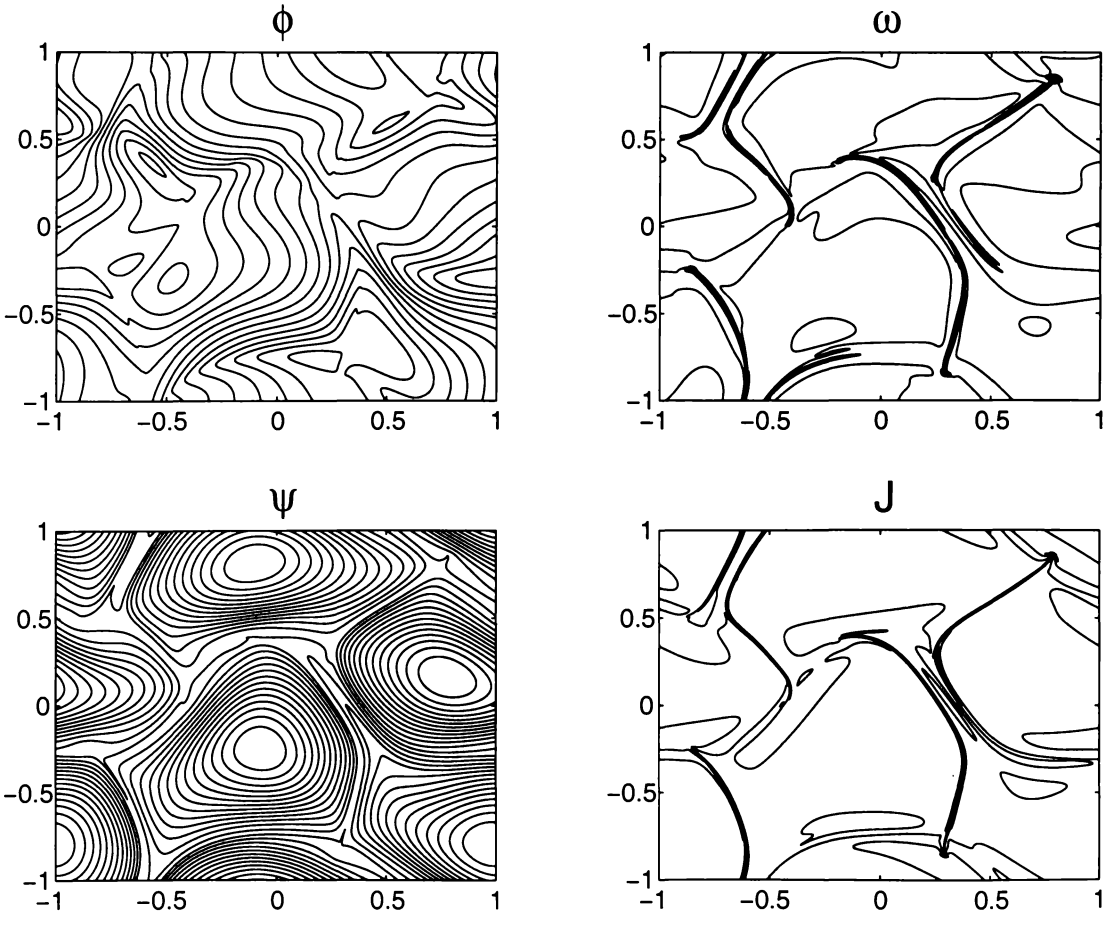

Figure 5.20: A simulation of the development of an asymmetric Orszag-Tang vortex (5.35). This plot corresponds to Figure 7.6 in Biskamp (1993). Here $\eta = \nu = 5 \times 10^{-5}$ *and the time is* 0.477.

Figure 5.20 matches Biskamp's results for $t = 1.5$. Since he works in the domain $[-\pi, \pi] \times [-\pi, \pi]$ and we work on $[-1, 1] \times [-1, 1]$ our times are a factor of π smaller. At this time the two simulations are in excellent agreement, however, at later times we observe different turbulent behaviour. Biskamp's simulations differ from ours in that he uses a "hyper resistivity" model, which replaces the term $\eta\nabla^2\psi$ with the term $-\eta_2\nabla^4\psi$ on the right hand side of the induction equation (4.10). This allows him to resolve his simulation for a much smaller value of the "resistivity" $\eta_2 = 10^{-8}$ and probably accounts for the differences that we observe in the later time evolution.

According to Biskamp, a tearing mode instability develops at $t = 2.1$ ($t = 0.668$ for our simulation) in the sliver of flux that lies to the right of the central flux cell of Figure 5.20. While Biskamp's simulation shows magnetic islands developing from this sliver, what we see is a uniform diffusion of the field in this region.

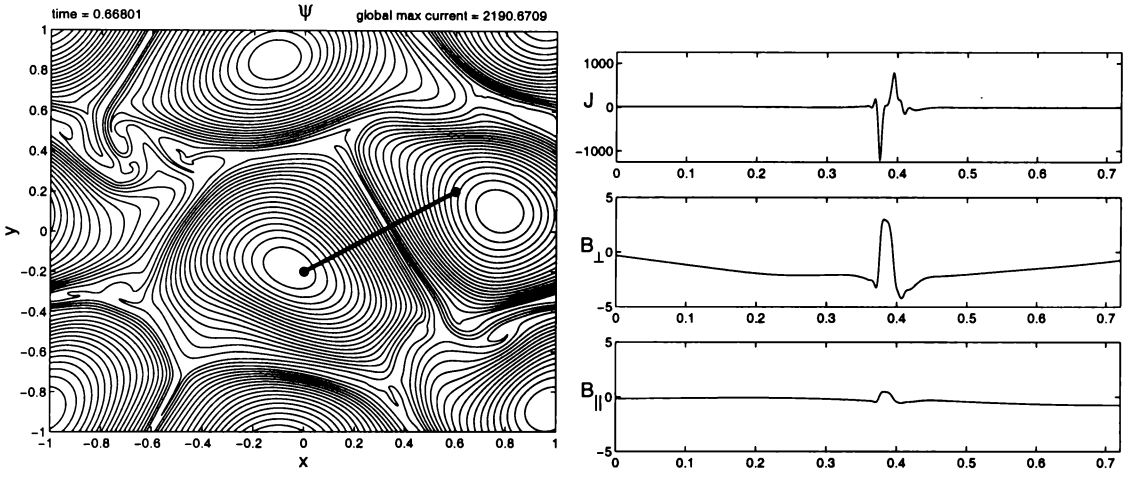

Figure 5.21: This is the configuration of Figure 5.20 at a slightly later time. The slices on the right clearly depict the sliver of "positive" flux trapped between the two large "negative" islands. These slices are taken along the line $(0, -0.2)$ *to* $(0.6, 0.2)$ *— the bold line shown in the contour plot.*

Figure 5.21 shows details of the magnetic field in our simulation at $t = 0.668$. Closer inspection of the field along a slice through the sliver shows that Biskamp's current sheet is in fact a region of reverse flux squashed between two cells of parallel magnetic field—in effect there are two oppositely directed current layers sandwiched together. Distortions of the field in this region evidently allow Biskamp to see the sliver being annihilated in such a way that magnetic bubbles form. However, the double current layer and lack of two clear regions of anti-parallel field are not characteristics of the classical tearing mode.

We also tried to find evidence of current sheet tearing by running high resolution head-on (no shear) simulations. Here we can exploit the four-fold symmetry of the

problem to solve it on the domain $[0,1] \times [0,1]$, allowing us to effectively double the resolution we used in Biskamp's run. Despite the high resolution, using values of η as low as 2×10^{-5} and achieving aspect ratios well in excess of 100:1, this approach did not allow even a glimpse of magnetic turbulence. It would seem that any turbulent behaviour, be it field line folding, small scale loop formation, or the tearing of current sheets, requires less uniform conditions than the idealised head-on model can provide.

With this in mind we tried several runs using a non-zero shear parameter β_0. These readily generate magnetic island structures for sufficiently small diffusion parameters. We used the familiar (see Sections 4.1, 5.1, 5.2, 5.4) 2-D initial conditions

$$\phi(x,y) = \alpha_0 \sin(\pi x)\sin(\pi y)/\pi \tag{5.37}$$

$$\psi(x,y) = \beta_0 \sin(\pi x)\sin(\pi y)/\pi + g_0 \cos(\pi x)/\pi \,, \tag{5.38}$$

with $\alpha_0 = -1$, $\beta_0 = 0.25$ and $g_0 = 0.1$. If simulations are performed with "large" values of the diffusion parameters, e.g. $\eta = \nu = 0.001$, smooth magnetic field structures are obtained (see Figure 5.22). Decreasing the diffusion parameters by

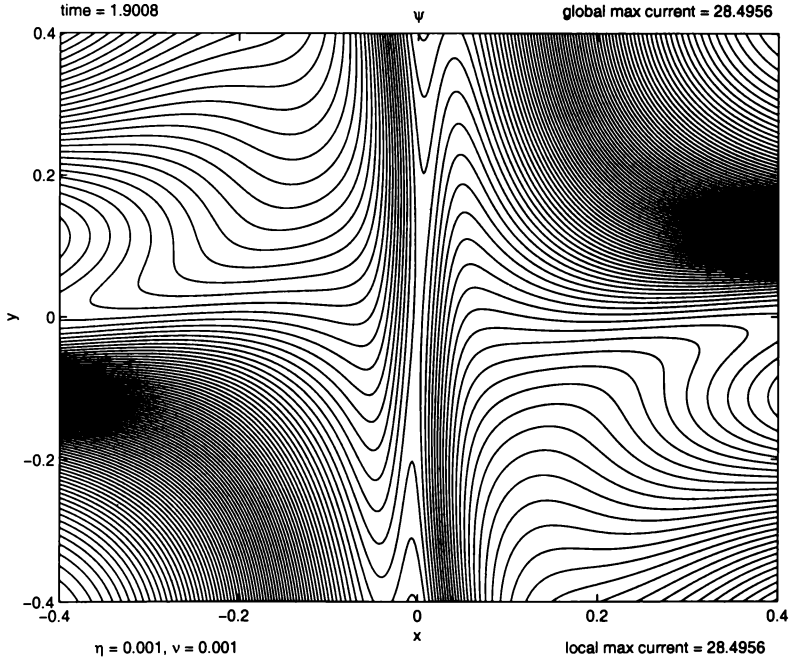

Figure 5.22: Magnetic configuration when the current sheet has almost dissipated for the sheared run $\alpha_0 = -1$, $\beta_0 = 0.25$ and $g_0 = 0.1$. The diffusion parameters in this case are comparatively large ($\eta = \nu = 0.001$) and turbulent effects are not present.

an order of magnitude, $\eta = \nu = 0.0001$, generates much richer magnetic structures. In Figure 5.23 we see three consecutive close-ups of the central current region. In the first one the magnetic field is smooth and there is a strong current sheet

approximately aligned with the y-axis. At a slightly later time two symmetric magnetic islands form near the center of the sheet. These islands then grow and move outwards as the sheet begins to dissipate. Notice, in the second frame, the concurrent formation of small length scale closed loop structures both inside and outside of the current sheet.

The top three plots in Figure 5.24 show clearly the anti-parallel nature of the field in the central current sheet. The set of plots on the right of this figure gives a horizontal slice at $y = 0.17$ that passes through the upper magnetic island. Although the current at the center of the sheet is still very high, the currents have died away significantly at the magnetic island. However, as the current is spread out across the width of the island, energy may still be rapidly dissipated in this region.

5.5.2 Summary

In searching for verification of the tearing mode instability we have repeated the numerical experiment of Biskamp (1994). We did not observe magnetic island formation in any of our Orszag-Tang initial configuration experiments, and it is not clear to us what features of the flow inhibit the appearance of the tearing mode in these simulations.

Our own search for the tearing mode instability began in the context of head-on reconnection, whose long, thin, straight current sheets would seem to provide the ideal location for magnetic island formation. Since our approach failed to find evidence of any turbulent behaviour, it would appear that the over restrictive symmetry of head-on reconnection precludes, or at least delays, the onset of turbulence.

Next we examined sheared reconnection, where we began to observe a variety of turbulent phenomena. Although magnetic island formation within current sheets was observed for certain initial configurations, we are not convinced that these are examples of the classical tearing mode, as only discrete pairs of islands are formed, rather than a whole chain. One possible explanation is that our dynamic sheets do not survive long enough for the instability to manifest itself properly. This certainly seems to be a factor in the simulation presented in Figure 5.23, where the current sheet is beginning to dissipate by the time magnetic islands form.

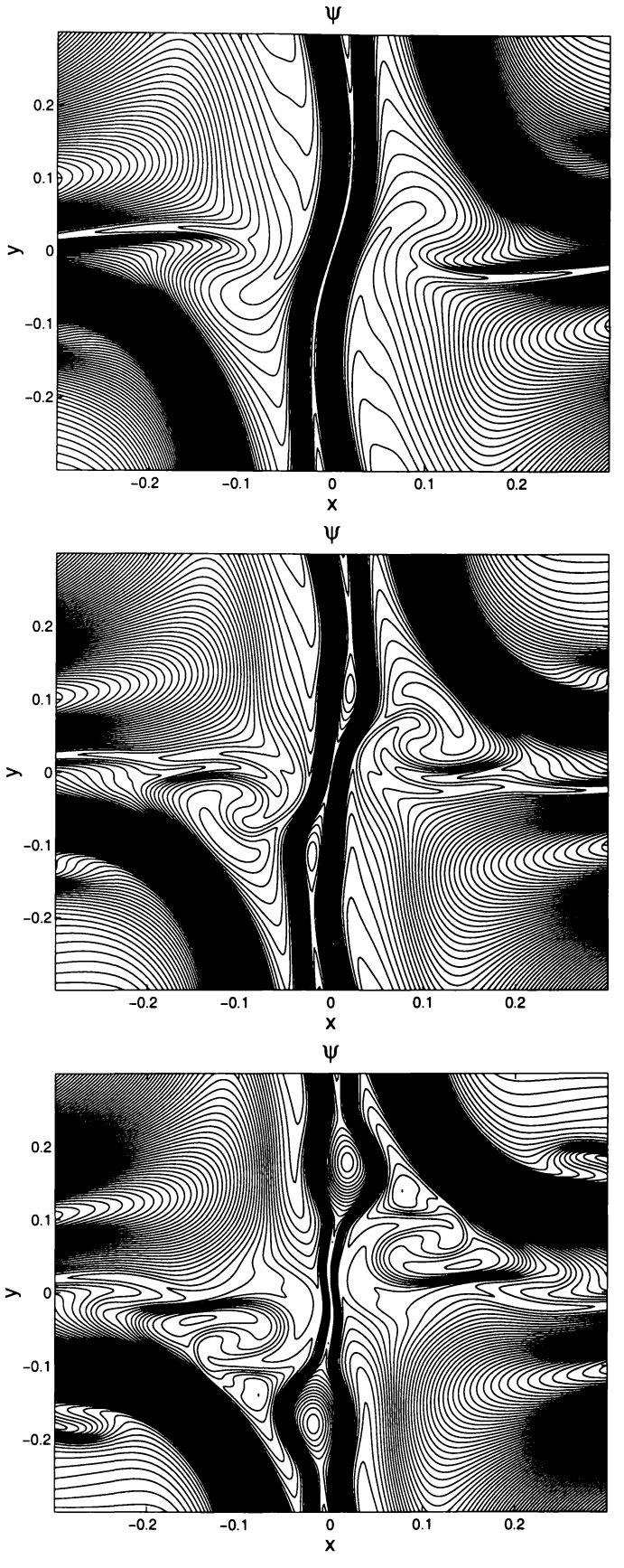

Figure 5.23: Three consecutive magnetic profiles showing the development of magnetic islands within a current sheet. Here $\alpha_0 = -1$, $\beta_0 = 0.25$ *and* $g_0 = 0.1$.

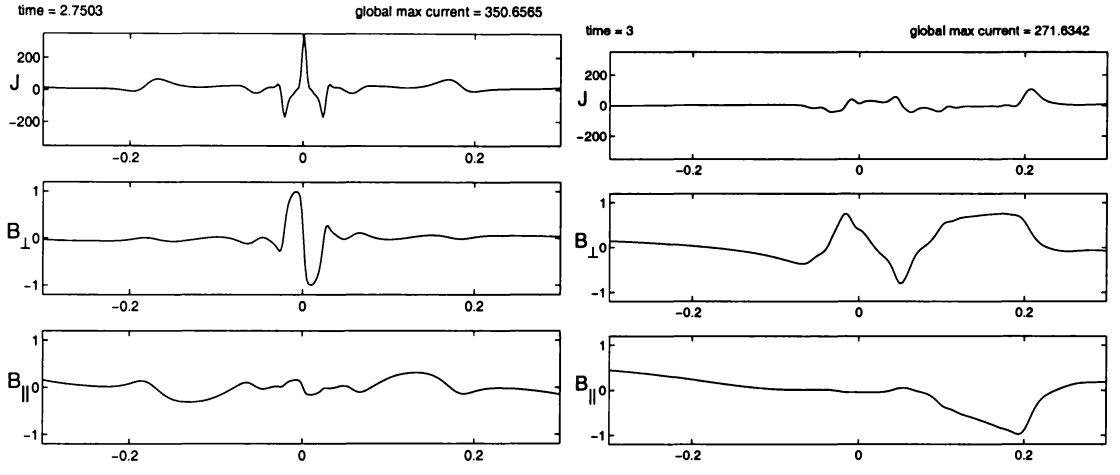

Figure 5.24: Slices along $y = 0$ (left) and $y = 0.17$ (right) of the middle and lower configurations of Figure 5.23 respectively showing the current density J and the magnetic components parallel ($B_{||}$) and perpendicular ($B_{\perp}$) to the cut.

Chapter 6

Solutions with multiple nulls

Thus far we have only considered analytic reconnection geometries involving a single magnetic neutral point. In this chapter we will investigate solutions involving multiple nulls. One of the inherent problems we have encountered so far in our analytic work is the infinite extent of current sheets. Introducing additional null points may overcome this restriction by providing an additional length scale over which currents can form. Also, configurations involving multiple nulls seem more realistic, given the complex jumbled field of the corona which we are trying to model. Finally, it is important to verify that our main results for single nulls are not undone when multiple nulls are present.

We will now attempt to extend the three dimensional analytic theory of Chapter 3 to incorporate multiple nulls. Recall our superposition argument of Section 3.3.1 in which we decompose the magnetic and velocity fields into background ($\mathbf{P}$) and disturbance ($\mathbf{Q}$) fields in the following way:

$$\mathbf{B}(\mathbf{x}) = \lambda\mathbf{P} + \mathbf{Q} \tag{6.1}$$

$$\mathbf{v}(\mathbf{x}) = \mathbf{P} + \lambda\mathbf{Q} \, . \tag{6.2}$$

Previously we used the simplest form of the background potential field

$$\mathbf{P}_X = \alpha \left[\kappa x, (1-\kappa)y, -z\right] \, , \qquad 0 \leq \kappa \leq 1 \, , \tag{6.3}$$

which gave rise to two generic forms (given by (3.35) and (3.36)) of the disturbance field $\mathbf{Q}$. These can then be combined with $\mathbf{P}_X$ to yield exact 3-D solutions for fan and spine reconnection respectively. Fabling (1997) has shown that the fan formulation does not extend naturally to incorporate multiple nulls, therefore in the remainder of this chapter we shall consider only the spine formulation

$$\mathbf{Q}_S(x,y) = Z(x,y)\hat{\mathbf{z}} \, , \tag{6.4}$$

and modify $\mathbf{P}$ to generate multiple neutral points.

For an *isolated* null, as given in (6.3), current accumulation about the neutral point requires outflow along the spine axis, that is $\alpha < 0$, corresponding to a positive null. As far as multiple null solutions are concerned, it is easy to verify, following Fabling (1997), that the fan formulation allows only trivial variants of the isolated X-point null (6.3). The spine models incorporate not only fully two-dimensional disturbance fields, but also in a certain sense, the fan solutions. This follows by noting that a single fan component $\mathbf{Q}_{\mathrm{F}} = X(z)\hat{\mathbf{x}}$ can be modeled by taking the restricted spine form $\mathbf{Q}_{\mathrm{S}} = Z(x)\hat{\mathbf{y}}$ and interchanging the x and z coordinates. Thus general fan models can always be constructed by the superposition of two one-variable spine solutions.

6.1 Cartesian spine equations

To confirm that the spine formulation admits multiple null solutions we substitute the forms (6.1) and (6.2) into the induction equation assuming the spine form (6.4) for $\mathbf{Q}$. The Cartesian components of $\mathbf{P}(\mathbf{x}) = \alpha(P_1, P_2, P_3)$ must satisfy

$$\begin{aligned} -P_{3,z}Z + P_1 Z_x + P_2 Z_y &= \bar{\eta}[Z_{xx} + Z_{yy}], \\ P_{1,z}Z &= 0, \\ P_{2,z}Z &= 0, \end{aligned} \tag{6.5}$$

where

$$\bar{\eta} = \frac{\eta}{\alpha(1-\lambda^2)}, \tag{6.6}$$

and subscripted letters indicate partial differentiation. The y and z components of the induction equation imply $P_1 = P_1(x, y)$ and $P_2 = P_2(x, y)$, which together with the x component of the induction equation and the chosen disturbance form $Z(x, y)$ implies that P_3 must be a linear function of z. These conditions, along with the constraints

$$\nabla \cdot \mathbf{P} = 0 \quad , \quad \nabla \times \mathbf{P} = \mathbf{0} \tag{6.7}$$

of the current free equilibrium field, yield

$$P_3 = -\sigma z, \quad P_{1,x} + P_{2,y} = \sigma, \quad P_{1,y} = P_{2,x}, \tag{6.8}$$

where σ is a global constant.

It is easy to see that the x and y components of $\mathbf{P}$ are not restricted to linear functions. By taking

$$P_1 = \gamma\sigma x + H_1(x, y), \quad P_2 = (1-\gamma)\sigma y + H_2(x, y), \tag{6.9}$$

with γ constant, we note that (6.8) reduces to Cauchy-Riemann equations for the conjugate harmonic pair H_1 and H_2. In other words $H_{1,x} = -H_{2,y}$, $H_{1,y} = H_{2,x}$ and $\nabla^2 H_1 = \nabla^2 H_2 = 0$, so that

$$\nabla^2 P_1 = \nabla^2 P_2 = 0\,. \tag{6.10}$$

This result is exploited in Section 6.2.1 when we consider the cylindrical coordinate representation of the spine equation (see equation (6.11) below).

Finally we mention that the limit $\sigma = 0$ has little physical interest. In this case the disturbance field Z is advected only by transverse components of the flow. Since flow components normal to the field cannot stretch the field lines and magnify the field, there is no possibility of fast resistive dissipation for $\sigma = 0$ (see Fabling and Craig, 1996). In fact, as we saw in Section 3.3.3, for an isolated null located at the origin (given by (6.3) say), the physically interesting case is $\sigma > \kappa > 0$ and α negative. For the multiple null solutions dealt with in the analysis to follow we can relax these assumptions somewhat and take $\sigma > 0, \alpha < 0$.

6.2 Multiple null solutions

To make further progress it is convenient to assume that the background field $\mathbf{P}$ comprises of a central null at the origin surrounded by satellite nulls in the plane $z = 0$. In this way we can exploit the rotational symmetry of the problem about the spine axis. We recall from (6.9) that departures from linearity in $\mathbf{P}$ involve the superposition of conjugate harmonic functions to the Cartesian components P_1 and P_2. Let us now formulate the general problem.

6.2.1 Cylindrical formulation of multi-null solutions

We replace (x, y) by (r, θ) coordinates

$$r = \sqrt{x^2 + y^2}, \qquad \tan(\theta) = \frac{y}{x},$$

and set

$$\mathbf{P} = \alpha \left(P_1(r,\theta)\hat{\mathbf{r}} + P_2(r,\theta)\hat{\boldsymbol{\theta}} - \sigma z \hat{\mathbf{z}} \right), \qquad \mathbf{Q} = Z(r,\theta)\hat{\mathbf{z}}. \tag{6.11}$$

The divergence and curl conditions (6.7) on the background field now imply

$$\frac{1}{r}(rP_1)_r + \frac{1}{r}P_{2,\theta} - \sigma = 0, \tag{6.12}$$

$$\frac{1}{r}(rP_2)_r - \frac{1}{r}P_{1,\theta} = 0. \tag{6.13}$$

From (6.9) we know that the background field components P_1 and P_2 represent a conjugate harmonic pair with an added linear component and must satisfy the above

equations. Hence solutions to these are of the form

$$P_1 = \frac{\sigma}{2}r + \sum_{k=2}^{\infty} \mu_k r^{k-1}\cos(k\theta), \qquad P_2 = -\sum_{k=2}^{\infty} \mu_k r^{k-1}\sin(k\theta). \tag{6.14}$$

The induction equation reduces to

$$\sigma Z + P_1 Z_r + \frac{P_2}{r} Z_\theta = \bar{\eta}\left(\frac{1}{r}(rZ_r)_r + \frac{1}{r^2}Z_{\theta\theta}\right), \tag{6.15}$$

where $\bar{\eta}$ is given by (6.6). The axisymmetric single null case is recovered by setting $\mu_k = 0$ for all k. In this case we can remove the explicit dependence on $\bar{\eta}$ from the induction equation by letting $r \to r/|\bar{\eta}|^{1/2}$. It follows that there exists a universal small length scale $r \sim |\bar{\eta}|^{1/2}$ in the disturbance field Z. We conclude that multiple small scales in Z may only be possible by the admission of nonlinear components in the background field (see Watson and Craig (1997)).

6.2.2 Simple nonlinear nulls

Let us consider the contribution of a single nonlinear component in the summation (6.14). Taking $\sigma = 1$, the explicit form of $\mathbf{P}$ is given by

$$\mathbf{P} = \alpha\left[\left(\frac{r}{2} + \mu r^{m-1}\cos(m\theta)\right)\hat{\mathbf{r}} - \mu r^{m-1}\sin(m\theta)\hat{\boldsymbol{\theta}} - z\hat{\mathbf{z}}\right]. \tag{6.16}$$

In Cartesian coordinates we have that

$$\mathbf{P} = \alpha\left[\left(\frac{x}{2} + \mu\mathrm{Re}(w^{m-1})\right)\hat{\mathbf{x}} + \left(\frac{y}{2} - \mu\mathrm{Im}(w^{m-1})\right)\hat{\mathbf{y}} - z\hat{\mathbf{z}}\right], \qquad w = x + iy,$$

and so, for $m = 2$, the background field reduces to $\mathbf{P} = \alpha((1/2+\mu)x, (1/2-\mu)y, -z)$. This is just the X-point field (6.3) with $\kappa = 1/2+\mu$ and $\sigma = 1$. Obviously we must take $m \geq 3$ to achieve nonlinear solutions.

As already mentioned, the separatrix structure of the background field $\mathbf{P}$ provides an indication of the nature of the reconnection. For nonlinear nulls we can linearise the field in the vicinity of each null and determine the resultant eigenstructure as we did for the single null solutions of Section 3.3.

In general the background field given by (6.16) possesses a central null at $r = z = 0$, as well as m satellite nulls lying in a ring determined by

$$\sin(m\theta) = 0, \quad r^{m-2} = -\frac{1}{2\mu\cos(m\theta)}, \quad z = 0. \tag{6.17}$$

Since $\sin(m\theta) = 0$ we must have $\cos(m\theta) = \pm 1$. Therefore, for $\mu > 0$ we require $\cos(m\theta) = -1$ and $\theta = (2j+1)\pi/m$, $j = 0, 1, 2, \ldots$ in order for r to be real. Alternatively if $\mu < 0$ we require $\cos(m\theta) = 1$ and $\theta = 2j\pi/m$, $j = 0, 1, 2, \ldots$. The eigenstructure of this field, for the case $\mu > 0$, is summarised in Table 6.1.

Location of null (r, θ, z)	Eigenvalues γ_i/α	Eigenvectors
$(0, 0, 0)$	$1/2, 1/2, -1$	$\hat{\mathbf{r}}, \hat{\boldsymbol{\theta}}, \hat{\mathbf{z}}$
$((2\mu)^{1/(2-m)}, (2j+1)\pi/m, 0)$	$1 - m/2, m/2, -1$	$\hat{\mathbf{r}}, \hat{\boldsymbol{\theta}}, \hat{\mathbf{z}}$

Table 6.1: The eigenstructure of the multiple null background field with cylindrical symmetry in the vicinity of the nulls. The background field possesses m satellite positive nulls evenly distributed about a central negative null located at the origin. Note that the eigenvalues have been normalised with respect to the field strength α.

Remember, from Section 3.3, that the eigenstructure of the field at the neutral point indicates the orientations of the fan surface and spine curve. This is because the eigenvalues are in general real and sum to zero. The fan surface is then generated by the eigenvectors of like sign, while the spine curve is aligned to the remaining eigenvector. It is clear form Table 6.1 that in the present case there is a special null at the origin whose spine extends along the z-axis with a corresponding fan in the plane $z = 0$. This central null has satellite nulls that lie in a ring determined by the equations

$$r^{m-2} = \frac{1}{2|\mu|}, \qquad \theta = \begin{cases} 2k\pi/m & \mu < 0 \\ (2k+1)\pi/m & \mu > 0 \end{cases}, \quad z = 0, \tag{6.18}$$

as shown in Figure 6.1. The satellite spines lie in the fan of the central null; their fans extend out of the $z = 0$ plane and intersect along the central spine axis $x = y = 0$. Adjacent nulls on the circle are separated by a radial field line (dashed line in the figure) that pierces the central null. Note the absence of mutual null-null lines for the satellites. A detailed field line plot is shown at the bottom of Figure 6.1.

6.2.3 Singular ideal solutions

We will now determine the form of the current structure by solving the induction equation (6.15) with $\eta = 0$, in the same way we did for the simple spine and fan solutions in Section 3.3.3. Let us focus on the lines of constant θ corresponding to the possible fan surfaces determined above (6.18) (see also figure 6.1). Near such rays we have $\theta = k\pi/m + \phi$, so that in this region

$$\sin(m\theta) \simeq (-1)^k m\phi, \qquad \cos(m\theta) \simeq (-1)^k,$$

and the corresponding characteristic quotients of the induction equation (6.15) with $\eta = 0$ are

$$\frac{\mathrm{d}r}{r/2 + (-1)^k \mu r^{m-1}} = \frac{-\mathrm{d}\phi}{(-1)^k \mu m r^{m-2} \phi} = \frac{-\mathrm{d}Z}{Z}.$$

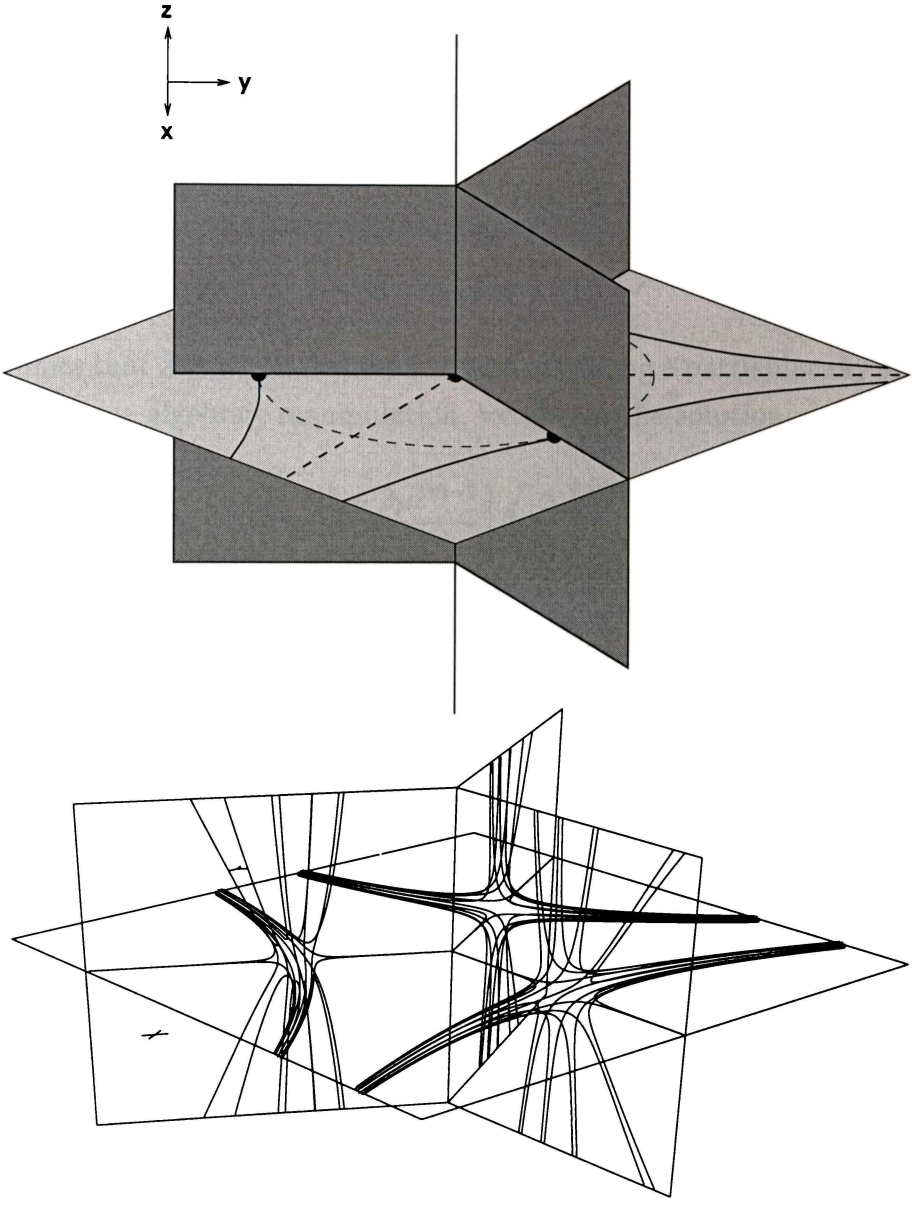

Figure 6.1: The upper figure shows the separatrix structure of a background potential field with cylindrical symmetry for $m = 3$. Fan surfaces are shown as solid planes, while the corresponding spine curves are solid lines. The lower figure shows the actual field line structure for the satellite nulls.

Performing the integrations (using the substitution $u = r^{m-2}/(m-2)$ for the ϕ-r integration) yields the characteristics

$$\xi_1 = \phi^{1/m}\left[\frac{1+(-1)^k 2\mu r^{m-2}}{(-1)^k 2\mu(m-2)}\right]^{1/(m-2)} \tag{6.19}$$

and

$$\xi_2 = Zr^2\left[\frac{1+(-1)^k 2\mu r^{m-2}}{(-1)^k 2\mu(m-2)}\right]^{2/(2-m)} \tag{6.20}$$

Next we impose the condition

$$\phi = \phi_c \tag{6.21}$$

$$Z = Z_0(r) \tag{6.22}$$

which assumes that Z is a well-defined function of r along a particular ray of constant θ. Following some algebraic manipulation, we obtain the solution

$$\begin{aligned} Z(r,\phi) &= Z_0\left(\left[\left[\frac{(-1)^k+2\mu r^{m-2}}{2\mu}\right]\left(\frac{\phi}{\phi_c}\right)^{(m-2)/m} - \frac{(-1)^k}{2\mu}\right]^{1/(m-2)}\right) \\ &\quad \times r^{-2}\left[r^{m-2}+\frac{(-1)^k}{2\mu}\left(1-\left(\frac{\phi_c}{\phi}\right)^{(m-2)/m}\right)\right]^{2/(m-2)} \end{aligned}$$

valid for small values of ϕ.

We can see from this solution that when $\phi = \phi_c$ we have our initial condition $Z = Z_0(r)$, as should be expected. We are interested in establishing where the solution is singular, since it is at these locations that we expect to see current sheets form once finite resistivity is introduced. Obviously we have a singularity at $r = 0$, the other singular regions take a little more interpretation. The bracket term on the right hand side is the $(m-2)$'th root of something squared, so this causes no singularities even if the interior of the bracket becomes negative. However, the ϕ_c/ϕ term does become infinite as $\phi \to 0$ since $m > 2$ is a positive integer. Hence this term gives us $2m$ evenly spaced singular radial lines. Looking at the Z_0 term, we have for $\phi \to 0$

$$Z_0(r) = Z_0\left(\left[\frac{(-1)^{k+1}}{(2\mu)}\right]^{\frac{1}{m-2}}\right),$$

so that

$$r^{m-2} = \frac{(-1)^{k+1}}{2\mu}.$$

At $\phi = 0$ we have $\theta = k\pi/m$, and so from (6.18) current forms only on the $\theta = k\pi/m$ rays along which the outer nulls lie.

6.2.4 Resistive solutions

Having established potential sites for current accumulation from the ideal ($\eta = 0$) analysis of the previous section we will now solve the fully resistive equations, focusing our attention on the current sheets which form at such sites. Due to the complexity of the induction equation (6.15), we must use numerical methods to explore the current build-up in the presence of resistive effects. The analytic problem has an open geometry but we must assume a finite region (here we take the unit square) in constructing a numerical solution. Since the behaviour of the solution on the boundary is unknown, we employ a numerical code that adopts boundary conditions based on the gross symmetries of the disturbance field. In all cases we find that an interior solution develops that is insensitive to the exact boundary values, except in a narrow transition layer close to the walls. The diagrams given below display only the interior solution.

Consider the $m = 3$ solution discussed above. As shown in Section 6.2.3, we expect strong currents to develop on the fan surfaces of the outer nulls. In general we expect (see Section 6.2.1) intense current structures to be associated with a small $\eta^{1/2}$ length scale (see also Section 6.3.3). If we specify anti-symmetry across the line $y = 0$, a special role is assigned to the satellite null on the shear line $y = z = 0$. As Figures 6.2(a) and 6.2(b) indicate, this null "attracts" more intense current structures than the two displaced nulls. Even so, the current density is strongest where the satellite fans meet—that is, along the spine axis of the central null.

These results are not surprising when we consider the separatrix structure of Figure 6.1. The disturbance field perturbs the fan of the central null and so we expect spine currents to develop near the origin. The null at the point $x = 1/(2\mu), y = 0$ has its spine perpendicular to the shear axis and so we anticipate strong fan currents in the region $x < 0, |y| \leq \eta^{1/2}$. By the same token, the remaining satellites develop somewhat weaker fan currents since their spines are not perpendicular to the axis of shear.

The resistive scalings for this configuration are dominated by the central spine-type neutral point at the origin. Current at the central null quickly builds up to levels where it far exceeds that of the satellite nulls, and thus "swamps" the solution. For this reason no significant improvement of energy dissipation occurs with this model over the simple isolated null spine solution. Next we will introduce a solution which incorporates more complexity and leads to more favourable dissipation rates than the single null model of Section 3.3.

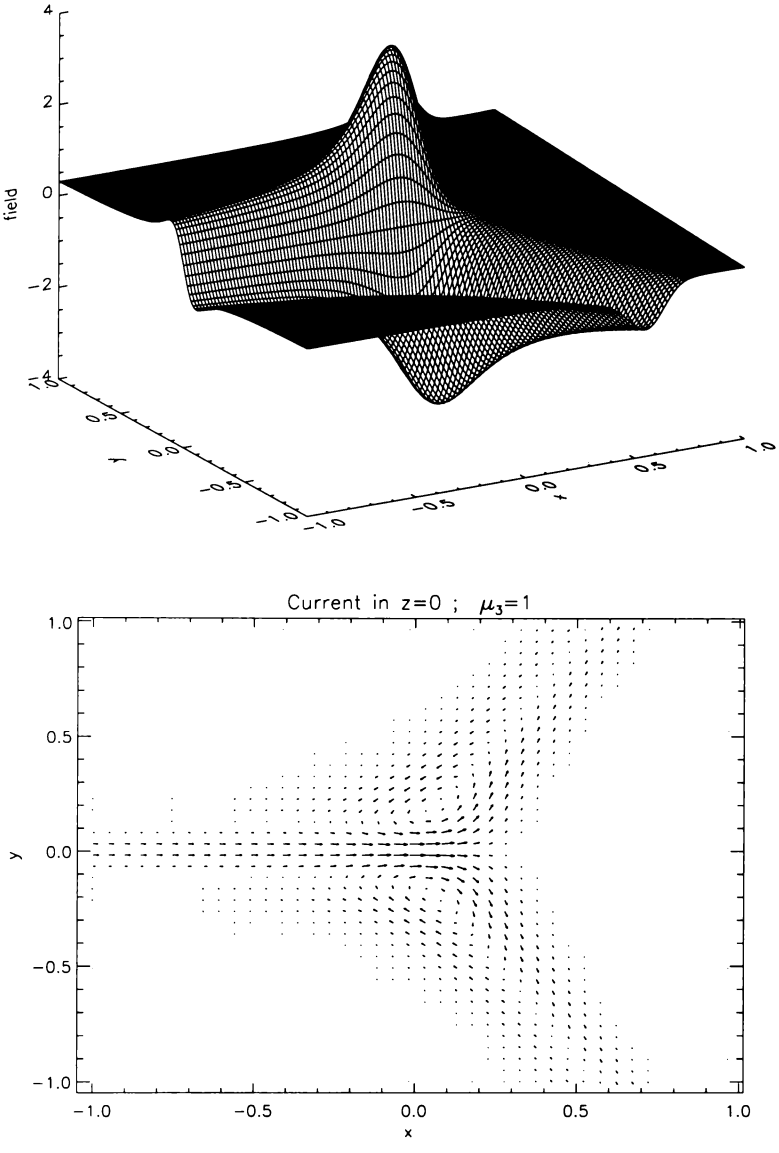

Figure 6.2: Field and current solutions for the background field (6.16) with $m = 3$ and $\eta = 0.01$. Note how despite the presence of three nulls a distance $r = 1/2$ along the arms, the majority of current still accumulates at the central spine.

6.3 An example of a more complicated multi-null model

6.3.1 Non-circular symmetric fields

It appears that the addition of a single higher order term in the background field equation (6.16), does not lead to significant departures from the resistive scaling laws of the isolated null spine current model discussed in Section 3.3.5. We will now

show that when the circular symmetry of the background field is relaxed, multiple null models can provide a range of solutions incorporating forms of fan, spine and separator reconnection. An interesting feature of these models is the tendency of the current to be localised to separatrix structures of finite extent. Of course, current sheets in single null models are always unbounded.

Suppose we eliminate the circular symmetry by combining the $m = 2$ and $m = 4$ background field components from (6.14). If we take

$$\begin{aligned} P_1 &= r/2 + \mu_2 r\cos(2\theta) + \mu_4 r^3\cos(4\theta), \\ P_2 &= -\mu_2 r\sin(2\theta) - \mu_4 r^3\sin(4\theta), \\ P_3 &= -z, \end{aligned} \tag{6.23}$$

the Cartesian form of the field is

$$\begin{aligned} P_1 &= \frac{x}{2} + x(\mu_2 + \mu_4 x^2 - 3\mu_4 y^2), \\ P_2 &= \frac{y}{2} + y(-\mu_2 - 3\mu_4 x^2 + \mu_4 y^2), \\ P_3 &= -z. \end{aligned} \tag{6.24}$$

We focus exclusively on the case $\mu_4 > 0$, when this field may contain as many as seven nulls. The parameter μ_4 then determines an overall scale for the problem, while the parameter μ_2 governs the number and structure of the nulls. The field morphology is illustrated in Figure 6.3.

We note that for $|\mu_2| > 1$ there are only three co-linear nulls, specifically, two outer nulls distributed symmetrically about the central null at the origin. When $|\mu_2| = 1$ each of the two outer nulls undergoes a pitchfork bifurcation generating an additional four satellite nulls to give a total of seven nulls. When $|\mu_2| = 1/2$ the two innermost satellite nulls coalesce with the central null (again in a pitchfork bifurcation) to yield a five null configuration — see the next section for the eigenstructure analysis. Note the appearance of separator field lines joining the three inner nulls in the seven null case $1/2 < |\mu_2| < 1$. Changing the value of the parameter $\mu_4 > 0$ has no effect on the structure of the nulls, but it does control the overall scale of the field. In what follows we choose μ_4 so that the innermost satellite nulls always lie at $x = \pm 1/2$. Figure 6.4 shows detailed field line plots for the three basic forms of background field in the plane $z = 0$.

6.3.2 Eigenstructure of the combined multi-null background field

Before we go on to solve for the disturbance field, let us analyse the eigenstructures of each of the nulls in the configurations depicted in Figure 6.3. Recall from Sections 3.3

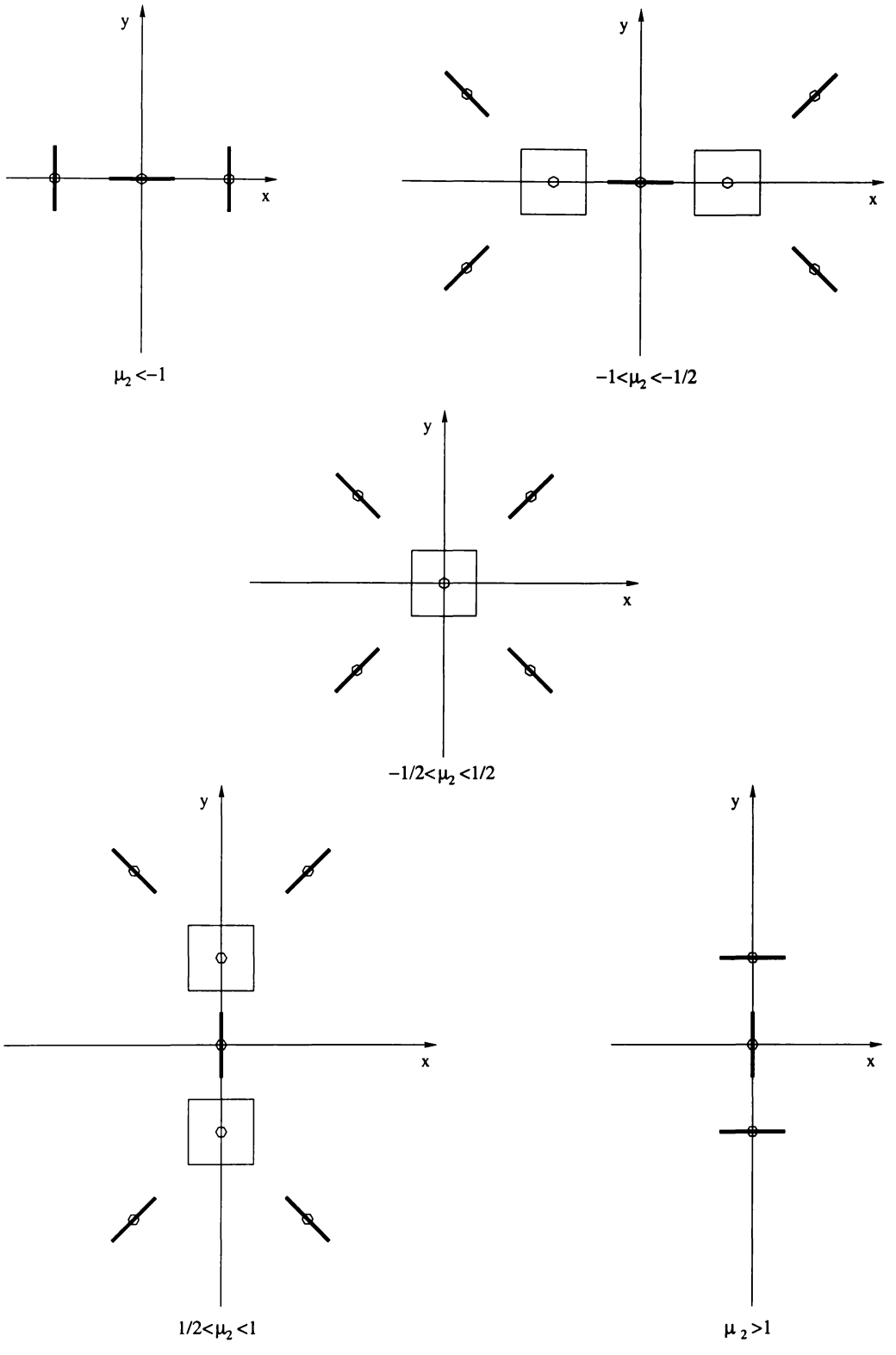

Figure 6.3: Schematic diagrams of the five different null topologies attainable by varying μ_2. The small hexagons represent the locations of the nulls, while squares and thick lines represent fan surfaces parallel and perpendicular to the page respectively (see Section 6.3.2 for eigenstructure analysis).

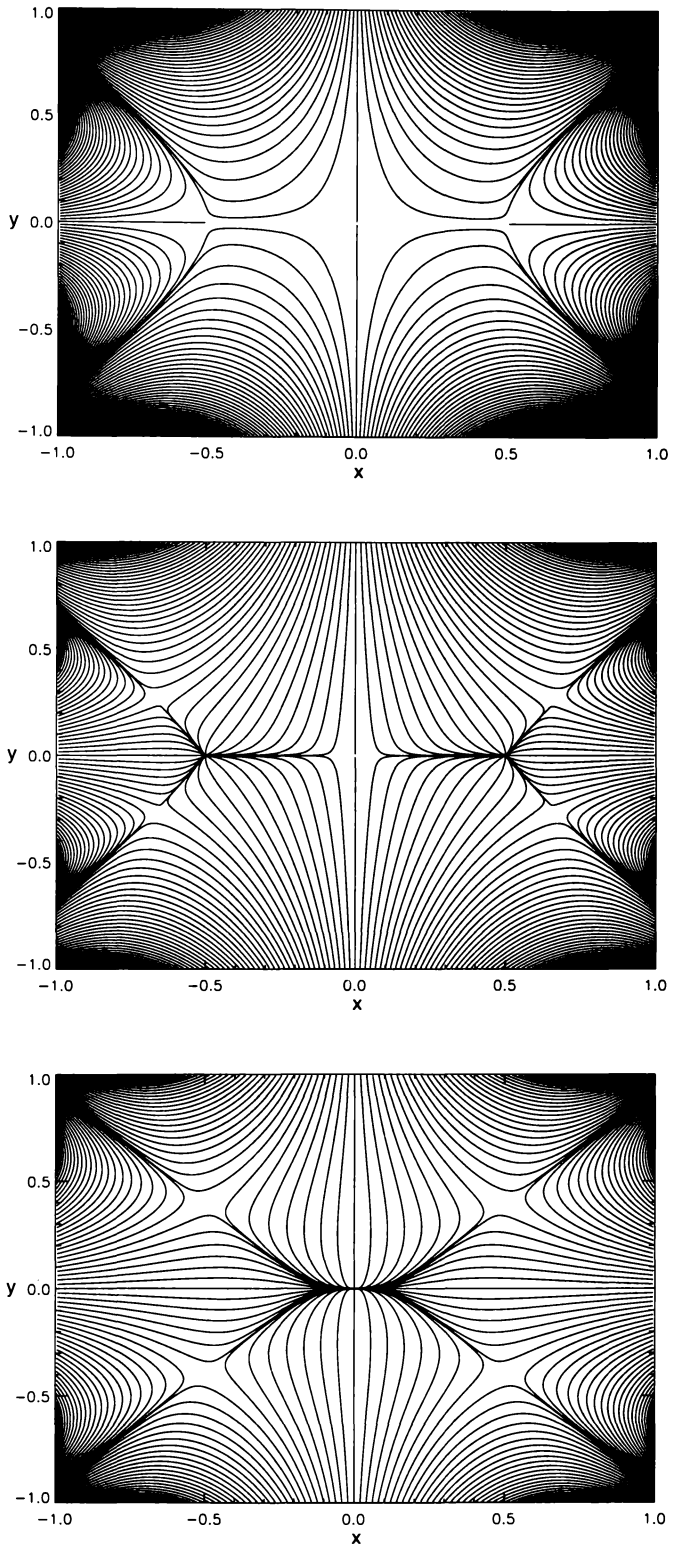

Figure 6.4: Diagrams of the field line structure in the $z = 0$ plane for the first three different null configurations shown in Figure 6.3. From top to bottom the values of μ_2 used are $-3/2$, $-3/4$ and $-1/4$ respectively.

and 6.2.2 that the eigenstructure of a three dimensional null tells us the orientation of its spine and fan. The eigenvectors of the matrix $\partial B_i/\partial x_j$ corresponding to the eigenvalues of like sign generate the fan surface, while the remaining eigenvector lies tangent to the spine.

For the background field given by (6.24) with $\mu_4 > 0$, there are nine possible locations for the nulls. These are given by $z = 0$ and the following ordinate pairs

$$\begin{aligned} x = 0 \quad &, \quad y = 0 \\ x = 0 \quad &, \quad y = \pm\sqrt{\frac{1+2\mu_2}{2\mu_4}} \\ x = \pm\sqrt{\frac{-1-2\mu_2}{2\mu_4}} \quad &, \quad y = 0 \\ x = \pm\sqrt{\frac{1-\mu_2}{4\mu_4}} \quad &, \quad y = \pm\sqrt{\frac{1+\mu_2}{4\mu_4}}. \end{aligned}$$

Note that a maximum of only seven nulls can exist for any fixed value of μ_2 (see Figure 6.3). The eigenstructure is summarised in Table 6.2. The fan planes of the

Location of null (x,y,z)	Eigenvalues γ_i/α	Eigenvectors
$(0,0,0)$	$\frac{1}{2}+\mu_2, \frac{1}{2}-\mu_2, -1$	$\hat{\mathbf{x}}, \hat{\mathbf{y}}, \hat{\mathbf{z}}$
$(0, \pm\sqrt{\frac{-1+2\mu_2}{2\mu_4}}, 0)$	$2-2\mu_2, -1+2\mu_2, -1$	$\hat{\mathbf{x}}, \hat{\mathbf{y}}, \hat{\mathbf{z}}$
$(\pm\sqrt{\frac{-1-2\mu_2}{2\mu_4}}, 0, 0)$	$-1-2\mu_2, 2+2\mu_2, -1$	$\hat{\mathbf{x}}, \hat{\mathbf{y}}, \hat{\mathbf{z}}$
$(\pm\sqrt{\frac{1-\mu_2}{4\mu_4}}, \pm\sqrt{\frac{1+\mu_2}{4\mu_4}}, 0)$	$\lambda_1, \lambda_2, -1$	$\mathbf{w_1}, \mathbf{w_2}, \hat{\mathbf{z}}$

Table 6.2: The eigenstructure of a combined multi-null background field. The sign of the primary and secondary nulls depends only on the magnitude of μ_2.

nulls given in the last row of the table do not coincide with the coordinate axes. The eigenvalues and eigenvectors corresponding to these nulls are given by

$$\lambda_1 = \frac{1+\sqrt{1+8(1-\mu_2^2)}}{2}, \quad \lambda_2 = \frac{1-\sqrt{1+8(1-\mu_2^2)}}{2},$$

$$\mathbf{w_1} = (1, A, 0), \quad \mathbf{w_2} = (-A, 1, 0)$$

and

$$A = \frac{\mu_2 + \sqrt{1+8(1-\mu_2^2)}}{\pm 3\sqrt{1-\mu_2^2}}.$$

6.3.3 The disturbance field

We consider only the simple case of a disturbance field $Z(x, y)$ whose amplitude is independent of x on the outer boundary. This corresponds to a global shearing of the background field across the x-axis. Since exactly the same results can be

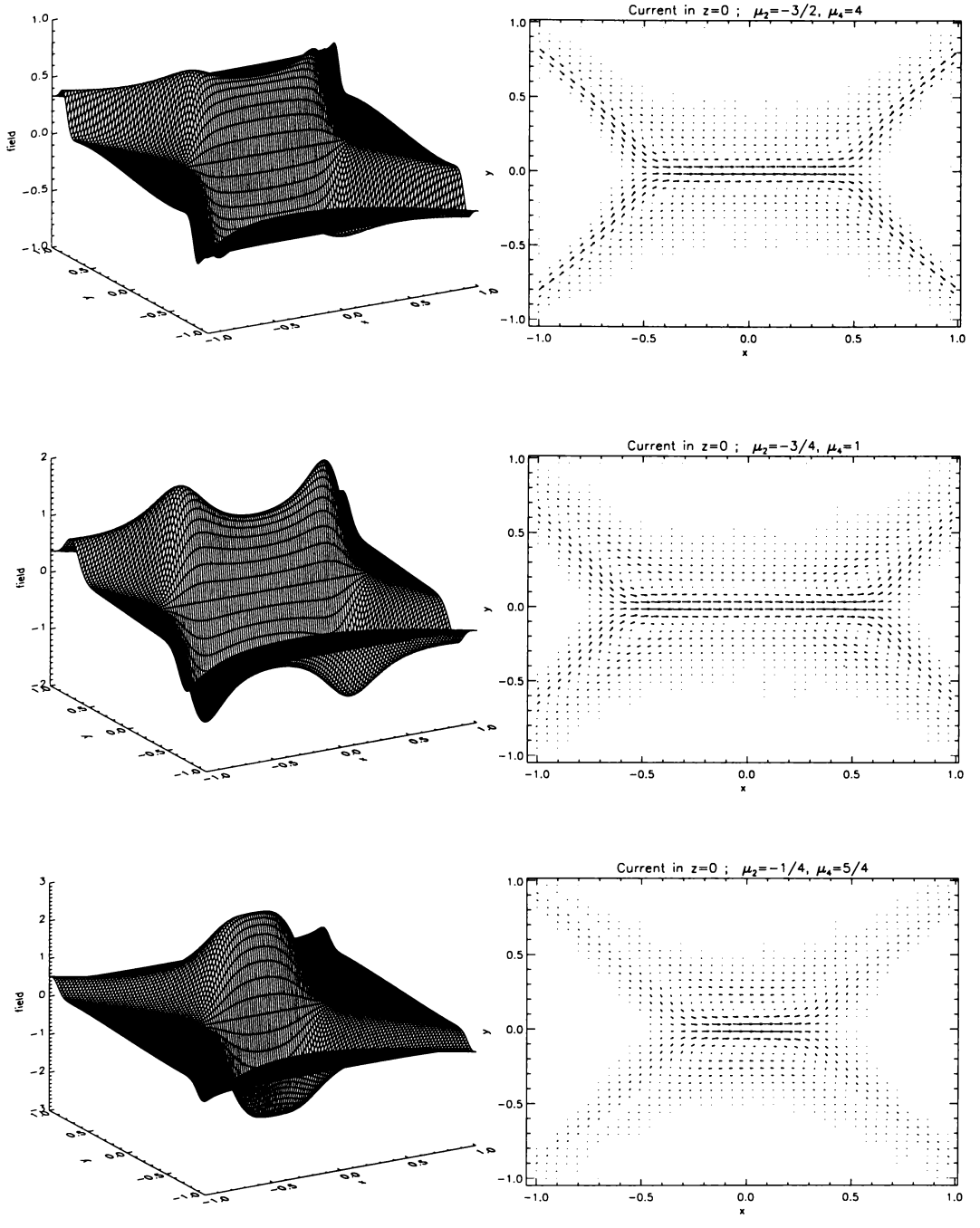

Figure 6.5: Numerical solutions of the induction equation (6.5). Field $Z(x, y)$ (left) along with corresponding current (right). Note the currents are only ever in planes of constant z since these are perpendicular to the disturbance field.

recovered by changing the parity of μ_2 and shearing across the y-axis it is clear that only the modulus of μ_2 is essential.

Figure 6.5 shows the form of the disturbance field Z and the resulting current density for the three, seven and five null background fields discussed above. The resistive scaling of the current density at the central null is shown in Figure 6.6.

Note that in Figure 6.6(b) we see current spikes forming around the spines of the two outer nulls, which clearly scale at a faster rate than the current at the central null. Although the resistive scalings reflect the spine and fan structures of the background field, there is always a strong current localization along the x-axis close to the central null. It is not difficult, as shown below, to predict the detailed current scalings by assuming that the disturbance field has the form $Z = Z(y)$ in the vicinity of the central null. These analytic predictions are shown by the dashed lines in Figure 6.6.

Finally it should be remembered that we are only solving for the disturbance field $\mathbf{Q} = Z(x, y)\hat{\mathbf{z}}$. This of course must be combined with the appropriate $\mathbf{P}$ to obtain the full magnetic and velocity fields (see equations (6.2) and (6.1)) via superposition. For example, to determine a separator reconnection model we should superpose the background field shown in Figure 6.4(b) with the disturbance field given in Figure 6.5(b).

6.3.4 Analytic scalings using boundary layer analysis

Here we use a boundary layer argument similar to Section 3.3.5 to determine the scaling of the peak field at the origin with respect to resistivity. Suppose we assume that $Z = Z(y)$ close to the central null. This assumption is based on the gross shear perturbation applied to the entire domain (see Section 6.2.4). The leading order terms in the Cartesian form of the induction equation (6.5) reduce to

$$\bar{\eta}Z'' - \left(\frac{1}{2} - \mu_2\right) yZ' - Z = 0, \quad Z = Z(y),$$

and we recover the presence of a small length scale $\Delta y \sim |\bar{\eta}|^{1/2}$. If we identify the region $y < \Delta y$ as a resistive current layer we can deduce resistive scaling laws based on a simple boundary layer treatment of the induction equation similar to that given in Section 3.3.5. In the analysis below μ_2 is taken to be negative. Identical results apply for positive μ_2 provided we take $Z \to Z(x)$ and apply the shearing across the y-axis.

In the far field $y \gg \Delta y$, where the resistive term is almost zero, we have that

$$\left(\mu_2 - \frac{1}{2}\right) yZ_o' \simeq Z_o,$$

and so

$$Z_o = y^{2/(2\mu_2 - 1)}, \tag{6.25}$$

on taking the normalization $Z(1) = 1$. An appropriate inner solution is simply $Z_i \sim y$ where the amplitude is chosen to match the outer solution at the edge of the

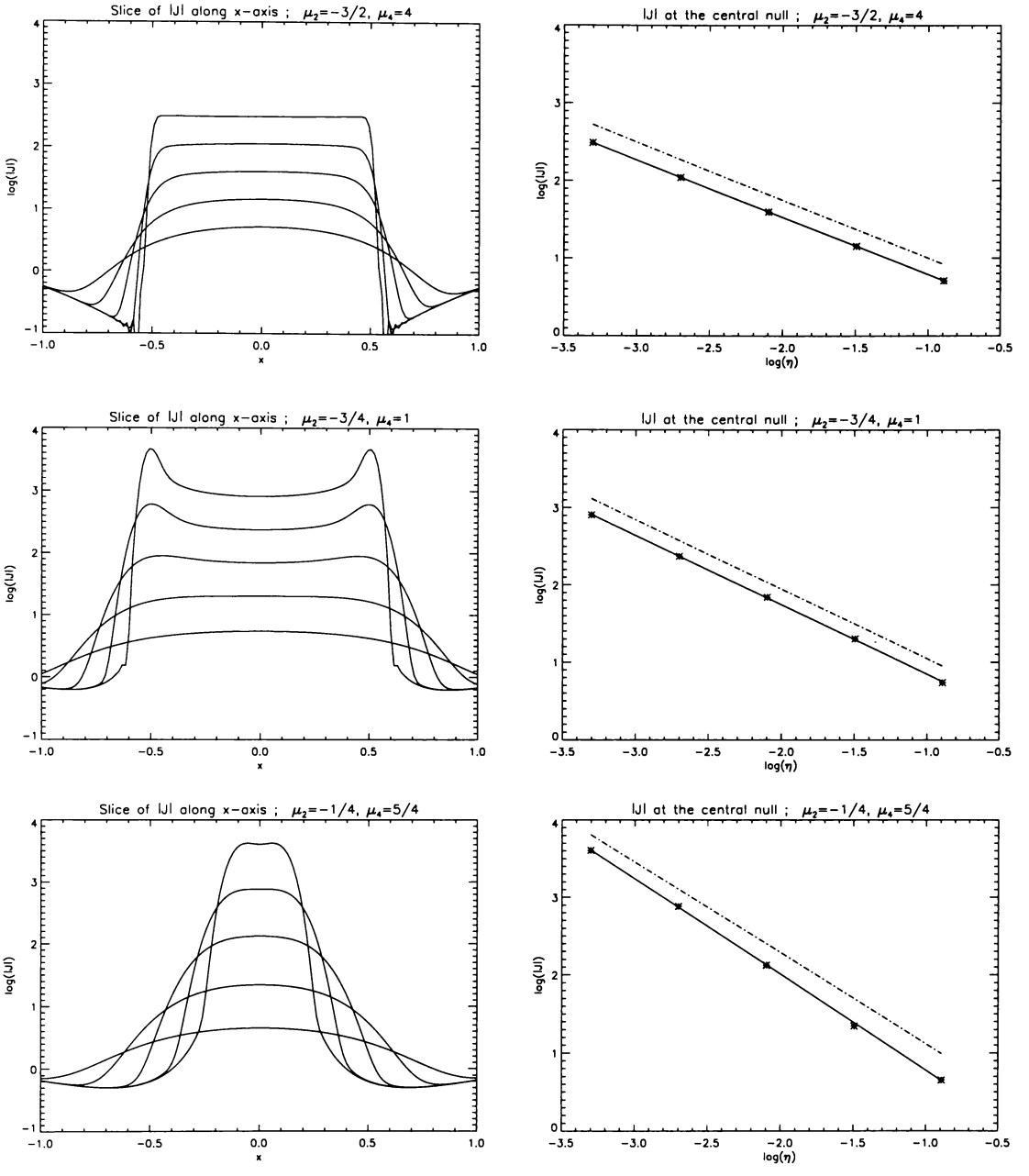

Figure 6.6: Montage of current magnitude along the x-axis (left), along with the scaling relation at the central null (right). The current plots are for η = 0.0005, 0.002, 0.008, 0.032 and 0.128, with smaller values of η generating larger currents. The dashed lines on the scaling plots represent the slope predicted by (6.26). Note the problem is slightly under resolved in the current plots for $\eta = 5 \times 10^{-4}$.

resistive current layer $y \simeq \Delta y \sim \eta^{1/2}$. The amplitude of the field and the current in this region then scale as

$$Z_{\max} \sim \eta^{1/(2\mu_2-1)}, \quad J_{\max} \sim \eta^{(3-2\mu_2)/(4\mu_2-2)}, \tag{6.26}$$

where we have used $J_{\max} \simeq Z_{\max}/\Delta y$. The dashed lines in Figure 6.6 confirm that

the predicted scalings of the current density accord very well with the numerical solutions.

6.3.5 Summary of resistive scalings

In Figure 6.7 we summarise the scaling results as a function of the topology parameter μ_2. Recall that the central null goes from having a fan-like current structure for $|\mu_2| > 1$, through a separator phase where a current ribbon is centered on the intersection of two fans, and finally a spine-like current phase when $0 < |\mu_2| < 1/2$. It is a remarkable fact that the scalings appear uncompromised by bifurcations in the null structure of the background field.

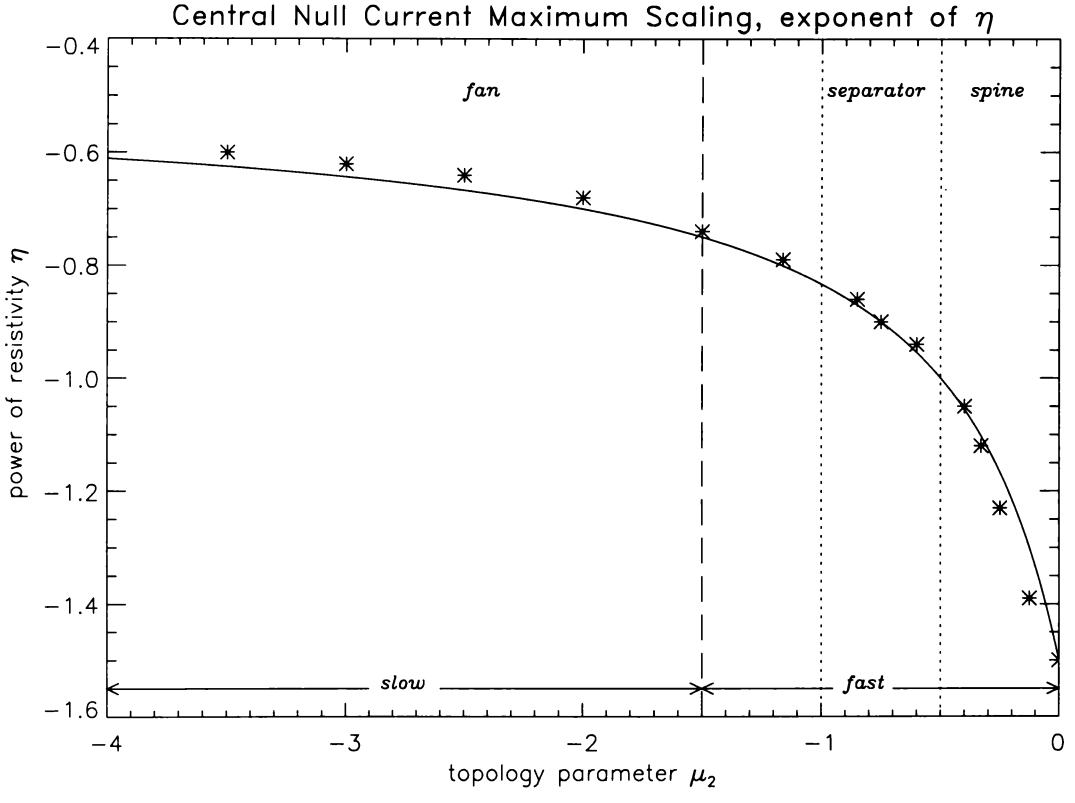

Figure 6.7: Summary of scalings for a range of μ_2 values. The solid line is the scaling law as predicted by (6.26), while the asterisks mark values obtained by solving (6.5) numerically. The fan, separator and spine regimes are separated by vertical dotted lines. Note that we have 'fast' reconnection for $\mu_2 > -3/2$.

We can determine which values of μ_2 correspond to fast reconnection by looking at the Ohmic dissipation rate (2.27)

$$W_\eta \simeq \eta J^2 \Delta V \sim l\eta^{(2|\mu_2|-3)(4|\mu_2|+2)} . \tag{6.27}$$

Here we use the volume element $\Delta V = lwL$, where l is the length in the x direction, w is the sheet width, and L is the length in the z direction. We know that the sheet

width $w \sim \eta^{1/2}$, while the sheet always spans the entire z length of the box. In this scaling we entertain the possibility that the x-length l may depend on η. Clearly W_η becomes independent of η when $|\mu_2| = 3/2$ and so models with $|\mu_2| > 3/2$ are associated only with slow ohmic dissipation. In fact the slow Sweet-Parker scaling $W_\eta \sim \eta^{1/2}$, is obtained only in the fan current limit $|\mu_2| \to \infty$. More generally, as shown in Figure 6.7, the region of potentially fast energy dissipation includes some fan current models, in the range $1 < |\mu_2| < 3/2$, as well as the totality of separator and spine solutions. However, this interpretation of the scalings assumes that the length of the sheet, l, remains fixed with reductions in η. From the forms of the spine solutions (see lower left plot of Figure 6.6) it appears that this assumption is not universally valid. Also, we would expect to recover the spine scaling $W_\eta \sim \eta^{-1}$ as $\mu_2 \to 0$, hence from (6.27) we must have $l \sim \eta^{1/2}$ in this limit. This point was not made clear in the corresponding paper (Craig *et al.*, 1999).

Can we claim that multiple null reconnection is more favourable than single null reconnection? On the basis of the present results we cannot claim any significant improvement on the energetic scalings of the isolated fan reconnection model (see Craig *et al.* (1997)). However, we believe the multiple null models are more realistic. The magnetic field solutions now display a higher degree of complexity—possibly more typical of the fields in the active corona. The current structures that develop in the new models are also better behaved: they are confined to localised ribbons, and no longer extend uniformly out to infinity as they do for an isolated null.

Finally, we mention that the fast resistive scalings of the present solutions are an artifact of flux pile-up in the disturbance field. As we saw in Section 5.2, flux pile-up can be avoided (as in the Sweet Parker limit $|\mu_2| \to \infty$) but only at the cost of slow dissipation. Either way, the solutions presented in this chapter should be combined with a saturation argument which limits the maximum field to a level determined by the inflow conditions (see Section 5.2).

6.4 Conclusions

We have demonstrated that a range of three-dimensional, multiple null, reconnection solutions can be constructed using the spine formulation of Section 6.2.1. The essential idea is that reconnection is associated with the superposition of finite amplitude disturbances on equilibria with multiple neutral points. An encouraging feature of the analysis is that it confirms—and provides a mathematical description for—many of the qualitative features of magnetic reconnection deduced using purely kinematic arguments (e.g. Lau and Finn (1990); Priest and Titov (1996)). There is also some evidence from X-ray observations that strong current ribbons localise on the intersections of fan surfaces and spine and separator lines (i.e. the

quasi-separatrix layers of Demoulin *et al.* (1996)). The implication is that current sheets, tubes and ribbons may provide universal signatures for all forms of magnetic reconnection.

Perhaps more surprisingly, it is possible to display the basic ingredients of fan, spine and separator reconnection using a simple multiple null model whose morphology is specified by a single structure parameter μ_2. The form the reconnection takes depends both on the properties of the background field $\mathbf{P}$—this comprises a maximum of seven nulls in the example given in Section 6.3—and the symmetries of the disturbance field $\mathbf{Q} = Z(x, y)\hat{\mathbf{z}}$. We have shown, however, that by systematically varying the bifurcation parameter μ_2, we can construct a continuum of reconnection solutions, characterised by distinct, analytically predictable, resistive scaling laws. Solutions in the range $0 \leq |\mu_2| \leq 3/2$ correspond to fast dissipation, that is $W_\eta \geq \eta^0$. Notably, the classical Sweet-Parker dissipation rate, namely $W_\eta \sim \eta^{1/2}$, is recovered only in the limit $|\mu_2| \to \infty$. This rate is formally the slowest available for the present multiple null solutions.

It should be stressed that we expect our findings to be largely independent of the idealisations and assumptions we introduce for analytic tractability. We know for example, that our formulation is robust to the inclusion of time-dependent and viscous effects (see Section 3.4 and Craig and Watson (1999)). Perhaps the most severe requirement is the presence of an ignorable coordinate in the disturbance field $Z(x, y)\hat{\mathbf{z}}$. One way around this is to employ, from the outset, a numerical treatment of the disturbance field. Although a numerical solution will undoubtedly lead to more complex reconnection models, the basic building blocks of such solutions will still include spines, fans and separators as regions of current accumulation in magnetic merging solutions.

It is unfortunate that the rich separatrix structure of the solutions in this chapter cannot be tested using the 3-D code of Chapter 4. This is because the 3-D code requires periodic boundary conditions, and there seems to be no obvious way to extend the present formulation to include periodicity.

Note: the solutions presented in this chapter have been extended by Ji and Song (2001) to include the effects of a partially ionized plasma.

Chapter 7

Particle acceleration

So far in this thesis we have looked at reconnection models with the aim of understanding the solar flare energy mechanism. Although reconnection itself can convert large quantities of energy to heat and kinetic energy of the plasma, energy may also be released in the form of accelerated particles. We know, from Ohm's law, that current sheets and electric fields are intimately related. And of course charged particles are readily accelerated by a direct electric field. It stands to reason then, that electron and proton acceleration will be efficient within a current sheet, since here the electric field is large while the magnetic field, which tends to stifle the acceleration through gyro-capture, is relatively weak.

Our approach will be to release a proton in a steady-state magnetic field configuration and trace its motion. Two magnetic configurations will be considered: the classic X-point structure (like that of Figure 1.4) and the planar Craig-Henton solution of Section 3.2.1. We will compare the acceleration properties of these configurations both with each other and with observational data.

7.1 Introduction

We saw in Chapter 1 that a solar flare event is characterised by several signatures. So far in this thesis we have concentrated on the flare energy released through strong Ohmic heating (which should manifest in the form of X-rays and γ-rays) and bulk plasma motion. Of course we also noted that flare events are accompanied by a large number of energised particles. Protons, in particular, can be accelerated to several GeV. The rate of energisation for protons above 1 MeV can reach 10^{34} s^{-1}, and their energy content can exceed 10^{30} ergs (see Miller *et al.* (1997) for a review). Observations of long-duration solar gamma-ray flares indicate the presence of continuously accelerated ions for several hours after the impulsive phase (e.g., Ryan (2000)). This result suggests that at least some portion of charged particles

are accelerated by the direct electric field associated with a current sheet, rather than by the shock wave of the initial implosion as was previously thought (Klein and Trottet, 2001).

A large body of research has been devoted to the study of particle orbits in the context of both solar flares and the geotail (e.g., Speiser (1965); Martens (1988); Zhu and Parks (1993); Litvinenko and Somov (1993); Litvinenko (1996); Litvinenko (1997)). In particular, studies of orbits in X-point magnetic fields have been applied specifically to the flare problem (Bulanov and Sasorov, 1976; Bulanov, 1980; Bruhwiler and Zweibel, 1992). Recent numerical simulations have concentrated on the properties of proton orbits in X-point fields (Mori *et al.*, 1998). The magnetic field in X-point current sheets plays a key role in particle acceleration: although the field cannot change the particle energy directly, it can limit the energy gain by changing the orbit and restricting the displacement along the electric field.

The magnetic configurations considered so far, however, have a major drawback. Although capturing the basic reconnection topology, they do not represent a quasi-steady reconnection solution. Some authors have tried to remedy this defect by tracing charged particles in magnetic field structures obtained by solving the MHD equations numerically (Schopper *et al.*, 1999). Such strategies are invariably compromised by numerical resolution, in fact particle gyro-radii can be significantly smaller than the computational mesh. Numerical MHD experiments are also limited by the unnaturally large resistivities required to resolve the steep field gradients that accompany rapid magnetic merging.

Motivated by these difficulties, the aim of this chapter is to investigate particle acceleration using an exact, analytic magnetic reconnection geometry. As we saw in Chapter 3 solutions are now available which describe steady-state, incompressible magnetic merging at arbitrary plasma resistivities, both in two and three dimensions. The numerical simulations of Chapter 4 confirm that the steady-state solution agrees remarkably well with the properties of time-dependent reconnective current sheets. Our goal in this chapter is to investigate test particle orbits in the current sheet associated with the Craig-Henton reconnection solution and apply the results to proton acceleration in solar flares.

Of related interest is the work of Kobak and Ostrowski (2000), who recently employed the Craig and Henton solution as a basis for a particle acceleration numerical experiment. Unfortunately, their work concentrates only on the slowly dissipating field components and neglects the physically more interesting "flux pile-up" field. Remember that the Craig-Henton solution of Section 3.2 has a slightly more general analogue given by (3.57) and (3.58) which includes a slowly dissipating non-planar error function component. More critically, the solution (3.57, 3.58) is valid only for two dimensional flows, while their choice of parameters implies a three-dimensional

velocity field. Although Kobak & Ostrowski's field configuration can no longer represent a solution of the MHD equations, it seems likely that their findings regarding turbulent particle acceleration are not seriously compromised.

7.2 Particle acceleration model

The model we consider is somewhat of a hybrid. On one hand we assume the MHD equations are a valid, so that the plasma is collision dominated. On the other hand we calculate individual particle orbits by assuming no collisions! In reality the MHD approximation breaks down for coronal values of collisional resistivity ($\eta \simeq 10^{-14}$), and an anomalous resistivity develops. However, in such situations we may employ an "effective" resistivity which is many orders of magnitude larger as will be discussed later. What this means is that the bulk current sheet properties are approximately valid, while within the current sheet, where the acceleration occurs, the collisionless assumption applies.

Let us now look at the equations governing the particle motion, before we state the magnetic field solution used.

7.2.1 Basic equations

The equation of motion of a test particle in a magnetic field $\mathbf{B}$ and electric field $\mathbf{E}$ is given by

$$\dot{\mathbf{p}} = q\left(\mathbf{E} + \frac{1}{c}\mathbf{v} \times \mathbf{B}\right) , \quad \mathbf{p} = \gamma m \mathbf{v} , \tag{7.1}$$

where $\mathbf{v}$, q, m, $\mathbf{p}$ are the velocity, charge, rest mass and momentum of the particle respectively, and γ is the relativistic Lorentz factor. Given the a fluid velocity field $\mathbf{u}$ and a magnetic field $\mathbf{B}$, the electric field responsible for the particle acceleration is easily calculated using Ohm's Law:

$$\mathbf{E} = \frac{\eta}{c}\nabla \times \mathbf{B} - \frac{1}{c}\mathbf{u} \times \mathbf{B} . \tag{7.2}$$

To allow easy implementation of the reconnection solution, we choose to use the same non-dimensionalisation as before (see Section 2.1.2). Non-dimensionalisation is done with respect to the following characteristic values:

$$n_c = 10^9 \mathrm{cm}^{-3} , \quad B_c = 100\mathrm{G} , \quad L_c = 10^{9.5}\mathrm{cm} , \quad v_A = 10^9 \mathrm{cm\ s}^{-1},$$

where n_c is the coronal number density and v_A is the Alfvén speed. In these units $c = 30$ and we have a non-dimensional charge to mass ratio for protons of 9.067×10^7. It should be pointed out that we have used a slightly lower characteristic density, so that the Alfvén speed is about three times larger here than in Section 2.1.2.

7.2.2 Exact magnetic field solution

In Section 3.3.6 we derived a general reconnection solution associated with planar flows. Although the solution given by (3.57, 3.58) allows a non-planar magnetic field component, for the present work we will take the strictly 2-D solution. Hence each slice of constant z has the same configuration described by the solution

$$\mathbf{u} = \left[\alpha x + \frac{\beta}{\alpha}\frac{Q_0}{\eta\mu}\mathrm{daw}(\mu y), -\alpha y, 0\right] \tag{7.3}$$

$$\mathbf{B} = \left[\beta x + \frac{Q_0}{\eta\mu}\mathrm{daw}(\mu y), -\beta y, 0\right], \tag{7.4}$$

where

$$\mu^2 = \frac{\alpha^2 - \beta^2}{2\alpha\eta}$$

and $\mathrm{daw}(x)$ is the Dawson function defined by (3.18).

Recall, from Section 3.2, that α determines the strength of the background flow while $0 < |\beta| < \alpha$ acts as a shear parameter that controls the angle of the X-point merging. Only one of the separatrices has magnetic field advected across it: the other lies along a coordinate axis (the x-axis) which is also the location of the current sheet (see Figure 7.2). Note that, although the dynamic numerical simulations of Section 4.1 have confirmed the overall veracity of the steady state reconnection solution, certain refinements are required (namely, equalisation and saturation as discussed in Section 5.2 and reviewed below) to obtain a physically realistic reconnection model.

Figures 7.1 and 7.2 provide a qualitative comparison of a classical X-point field with the sheared X-point solution discussed above. Given that the configurations have a superficially similar magnetic structure we might anticipate similar particle energy spectra to arise from both models.

7.2.3 Application of the reconnection model

Since the field and flow are strictly planar, the corresponding electric field will be aligned normal to the plane. From (7.2) we have

$$\mathbf{E} = -\frac{Q_0}{c}\hat{\mathbf{z}}\,. \tag{7.5}$$

One of the defects of the analytic reconnection model is that the magnitude of the reconnecting field component, Q_0, is decoupled from the amplitude of the plasma flow defined by α. A related difficulty is the apparently unbounded flux pile-up in the limit $\eta \to 0$. As we saw in Section 5.2, these defects can be remedied by assuming physically reasonable equalisation and saturation conditions.

The equalisation assumption determines the flow amplitude: α is chosen so that the exhaust speed of the material expelled from the current sheet is determined by

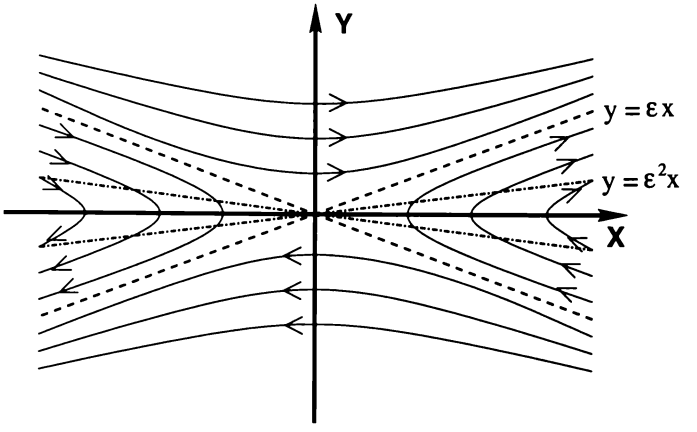

Figure 7.1: Schematic diagram of a typical X-point configuration (top) of the form $\mathbf{B} = B_0(y, \epsilon^2 x)$. *The separatrices (dashed) are given by the lines* $y = \pm\epsilon x$, *while dash-dot lines mark the region where* B_y *exceeds* B_x *and significant acceleration is possible. Current density is uniformly distributed over the entire domain.*

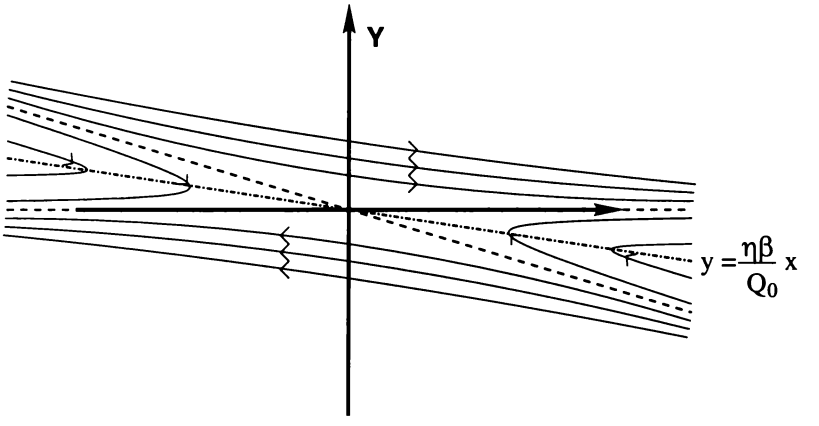

Figure 7.2: Schematic diagram of the Craig and Henton solution described in Section 3.2 showing the field lines (thin solid) and separatrices (dashed) within a narrow slice about the x-axis (see also lower plot of Figure 5.1). The dash-dot line represents the line along which B_x *vanishes and maximum acceleration occurs. Current is confined to a sheet of width* $\sim \eta^{1/2}$ *aligned to the x-axis.*

the local Alfvén speed based on the strength of the flux pile-up field. To prevent unbounded reconnection rates in the limit $\eta \to 0$ we also saturate the field at some physically appropriate level. In practice, this is achieved by choosing Q_0 so that the disturbance field in the sheet reaches a peak value corresponding to a dimensional value, say of $B_{\max} = 300$G. The equalisation condition is then imposed (Litvinenko and Craig (1999), Craig and Watson (2000b), Litvinenko and Craig (2000)) by setting $\alpha = B_{\max}/B_c = 3$. We must also choose a suitable value for β (remembering the restriction $0 < |\beta| < \alpha$), and for all our work we take $\beta = 2$. The value for Q_0

can then be determined from setting

$$\max\left[\frac{Q_0}{\eta\mu}\mathrm{daw}(\mu y)\right] = \alpha\ ,$$

which implies

$$Q_0 \simeq \alpha\eta\mu/0.541 \simeq 5\sqrt{\eta}\ , \tag{7.6}$$

since $\max[\mathrm{daw}(\mu y)] \simeq 0.541$.

The saturation and equalisation assumptions have the physically desirable effect of removing much of the arbitrary parameterisation from the reconnection model. Only the degree of shear, parameterised by β, remains free.

As we said earlier, the smallness of the collisional resistivity ($\eta \simeq 10^{-14}$) implies the sheet becomes so thin that the MHD approximation breaks down, leading to the development of an enhanced anomalous resistivity. In practice, resistive dissipation in the sheet could be enhanced, by a variety of factors, for instance by the development of a current-driven instability. In such cases it is useful to invoke an "effective" resistivity several orders of magnitude larger than the classical value (see Litvinenko and Craig (2000) and references therein). Although, the effective resistivity is almost certainly influenced by local factors such as temperature and density, we assume plausible values lie in the range $10^{-8} \leq \eta_{\mathrm{eff}} \leq 10^{-6}$.

7.2.4 Calculation of the particle orbits

Let us assume that we have constructed the magnetic field configuration according to the prescriptions given above. This field is to remain static and undisturbed as far as particle acceleration is concerned, consistent with the short acceleration times of the particles relative to the Alfvénic reconnection time-scale. Although the degree of shear determined by β is arbitrary, we must remember that β determines the angle of the X-point field and that an appreciable perpendicular field component must be present in the current sheet if particle capture is to be achieved (in practice we take $\beta = \frac{2}{3}\alpha$).

The numerical code used to calculate particle orbits utilises an embedded Runge-Kutta algorithm to integrate the equation of motion (7.1) forward in time. Each component is integrated to find $\mathbf{s} = \gamma\mathbf{v}$, from which γ and $\mathbf{v}$ can be extracted according to

$$s^2 = \gamma^2 v^2 = \frac{v^2}{1 - v^2/c^2}\ , \tag{7.7}$$

remembering that

$$\gamma = \left(\frac{1}{1 - v^2/c^2}\right)^{1/2} \tag{7.8}$$

We can then rearrange (7.7) to give

$$v^2 = \frac{s^2}{1 + s^2/c^2} \,. \tag{7.9}$$

From this we can find the updated γ, which in turn gives us the integrated velocity from $\mathbf{v} = \mathbf{s}/\gamma$.

The time-step size is determined by the local truncation error of the numerical scheme, which in turn is related to the local forces experienced by the particle. This adaptive time-step approach proved to be critical in achieving consistent results that did not require an unreasonable time to complete. Each particle trajectory typically comprises around a billion time-steps. Although there are formally more accurate methods for solving orbit problems, it should be remembered that the chaotic nature of the trajectories (Chen and Palmadesso (1986); Litvinenko (1993)) negates the benefits of such schemes, particularly as we are primarily interested in determining the associated energy spectrum.

7.3 Acceleration spectra

Although we have constructed a physically viable magnetic configuration that is an exact solution of the MHD equations, it is instructive to first look at some features of particle acceleration in a more basic X-point field. This will be a useful test of the code, and allow us to compare these with the results of the exact model.

7.3.1 X-point field models

Magnetic X-points are generally expected to produce well-defined particle acceleration spectra as we will now demonstrate. Consider a field of the form

$$\mathbf{B} = B_0(y, \epsilon^2 x, 0), \tag{7.10}$$

as illustrated in Figure 7.1. The spectrum is deduced by noting that an initial burst of acceleration due to the electric field is effectively cut short by the local magnetic field. As we discuss below, this occurs when the speed v_z has built up sufficiently for the Lorentz force ($\sim v_z B_\perp$) to gyro-capture the particle and thus limit the displacement along the z-axis and the energy gain.

Suppose a stationary particle is placed somewhere along the x-axis of the X-point field (7.10). In this case the equation of motion (7.1) reduces to

$$\dot{p}_x = -\frac{q}{c} v_z B_\perp \tag{7.11}$$

$$\dot{p}_z = qE + \frac{q}{c} v_x B_\perp \tag{7.12}$$

where $\mathbf{E} = E\hat{\mathbf{z}}$ and $B_\perp = B_\perp(x) = B_0\epsilon^2 x$ is the y-component of the field (7.10). If particles are distributed on $y = 0$ initially, all trajectories are limited to the $y = 0$ plane.

It is easy to see that the particle displacement along the z-axis is limited. Assume for simplicity that the perpendicular magnetic field $B_\perp$ does not change significantly over the particle orbit. The kinetic energy of the particle can be obtained by integrating the work done by the electric field. Hence the energy gain is given by

$$\mathcal{E} = qEz_{\max} \,. \tag{7.13}$$

This implies that the maximum energy occurs when $v_z = 0$. At this time $p_x = -qB_\perp z/c = p$ will be the total momentum, so that the displacement $z = z_{\max}$ must coincide with the gyro-radius

$$r_g = \frac{cp}{qB_\perp} \tag{7.14}$$

of the particle. It follows that in the non-relativistic case (Speiser, 1965)

$$\mathcal{E} = \frac{cpE}{B_\perp} = 2mc^2\left(\frac{E}{B_\perp}\right)^2 , \tag{7.15}$$

where we have used $\mathcal{E} = p^2/2m$. This result may also be deduced by noting that the electric field is transformed away in the reference frame moving along the x-axis with the speed

$$V = -\frac{cE}{B_\perp} , \tag{7.16}$$

a result which confirms that $2V$ is indeed the maximum speed achieved by the particle in the rest frame. In the moving frame the particle simply gyrates at the fixed energy given by $\frac{1}{2}mV^2$.

The above observations are reinforced by the exact non-relativistic solution to (7.11) and (7.12) given by

$$\begin{aligned} x(t) &= x_0 + \frac{V}{\omega}\sin(\omega t) - Vt \\ z(t) &= z_0 + \frac{V}{\omega}(1 - \cos(\omega t)) \,, \end{aligned} \tag{7.17}$$

where V is defined by (7.16), $(x_0,\, z_0)$ is the initial position, and

$$\omega = \frac{qB_\perp}{mc} \,. \tag{7.18}$$

An energy spectrum may be derived from the relation

$$\frac{\mathrm{d}n}{\mathrm{d}\mathcal{E}} = \frac{\mathrm{d}n}{\mathrm{d}x}\,\frac{\mathrm{d}x}{\mathrm{d}\mathcal{E}} \,, \tag{7.19}$$

(Martens, 1988) where n is the particle number density. Since $B_\perp = B_0\epsilon^2 x$, equation (7.15) gives the scaling

$$\mathcal{E} = Ax^{-2} \,, \tag{7.20}$$

where $A = 2mc^2E^2/(B_0^2\epsilon^4)$. If we assume a uniform initial distribution ($\mathrm{d}n/\mathrm{d}x =$ constant), then the energy spectrum should approximate

$$\frac{\mathrm{d}n}{\mathrm{d}\mathcal{E}} = KA^{1/2}\mathcal{E}^{-3/2}\,, \tag{7.21}$$

where K is a constant. This implies a characteristic power-law spectrum in the absence of any loss processes that might result in a steeper spectrum.

7.3.2 X-point relativistic particle spectra

It is interesting that the argument for a power law spectrum breaks down in the highly relativistic case. The kinetic energy, now manifested mainly as an increase in mass rather than speed, can again be derived by transforming away the electric field. Using the relativistic form for the kinetic energy, namely $\mathcal{E} = \sqrt{c^2p^2 + m^2c^4} - mc^2$, modifies (7.15) according to

$$\mathcal{E} = \frac{cpE}{B_\perp} = 2mc^2\frac{E^2}{(B_\perp^2 - E^2)} \tag{7.22}$$

for the case of a fixed perpendicular magnetic field (Alekseev and Kropotkin, 1970). Of course the magnetic field experienced by the particle is *not* fixed over the capture phase. The effect of the inhomogeneous magnetic field is particularly noticeable for protons released close to the neutral point, where even slight deflections in the x direction lead to the particle experiencing strong relative enhancements in $B_\perp$ (Bulanov and Sasorov, 1976). In spite of this limitation, equation (7.22) should remain qualitatively valid, indicating that the particles can gain very large energies in the vicinity of the X-point defined by the condition $B_\perp(x) < E$. Of interest is the fact that relativistic effects, which give rise to longer acceleration times for particles near the neutral point, will tend to negate the inhomogeneous $B_\perp$ which shortens the acceleration time. Hence these arguments suggest that the non-relativistic constant field approximation (7.15) can provide a good predictor for relativistic inhomogeneous magnetic field acceleration (see Figure 7.3 and discussion below).

It is a simple matter to verify these observations numerically for the reference X-point field (7.10). In order to provide a comparison, we set the X-point angle specified by ϵ to be the same as the corresponding separatrix angle in the exact reconnection solution given by (5.34). With this specification $B_\perp$ is not quite strong enough to capture the majority of particles and so, to obtain suitable test conditions, we adjust the level of magnetic field (by a factor of 10) independently of the electric field (this is of course equivalent to taking a larger X-point angle).

Figure 7.3 shows the computed relationship between initial position and maximum energy. The central straight line gives the scaling predicted by the non-relativistic approximation (7.15). This scaling is accurate until relativistic effects

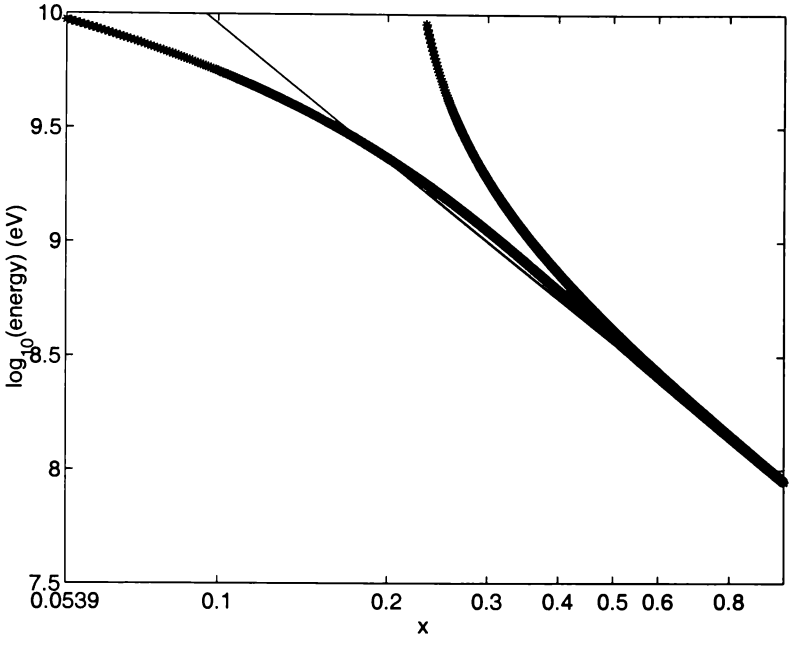

Figure 7.3: This figure shows the relationship between initial position and maximum energy gain for particles released along the x axis of the X-point configuration (7.10). The upper solid line represents the simpler case where $B_\perp$ remains fixed over a particle's entire orbit, while for the lower solid $B_\perp$ this simplification is not made. The thin straight line represents the non-relativistic scaling predicted by (7.20)

kick in at energies above $10^{8.5}$eV, which corresponds to $v/c \simeq 2/3$. The solid line above this represents a set of particle orbits for which, to maintain strict fidelity with the analytic scaling argument, $B_\perp$ is fixed to its initial value on each trajectory. This curve precisely coincides with the relativistic prediction (7.22). The lower solid line in Figure 7.3 represents the real X-point solution, in which $B_\perp$ increases according to the x-position of the particle. This effect clearly decreases the expected energy gain of relativistic particles started close to the neutral point where the initial $B_\perp$ is weak: prior to capture these particles experience ever increasing $B_\perp$ fields due to their motion in the x-direction.

To obtain a spectrum, we first calculate the final energy of 1000 particles distributed uniformly (to satisfy $\mathrm{d}n/\mathrm{d}x$ = constant) along half of the current sheet. Next we divide the obtained energy interval range into a given number of equally sized "bins". We then sort the particles into the bins and a spectrum is given by the number of particles in each energy range.

Figure 7.4 shows the spectrum obtained from the lower plot of Figure 7.3. The reference line represents the prediction (7.21), and it is clear that the theoretical power-law scaling is quite well reproduced. A slight steepening is evident at higher energies ($\sim 10^{9.5}$eV) corresponding to $\mathcal{E}(x)$ becoming less steep (see Figure 7.3).

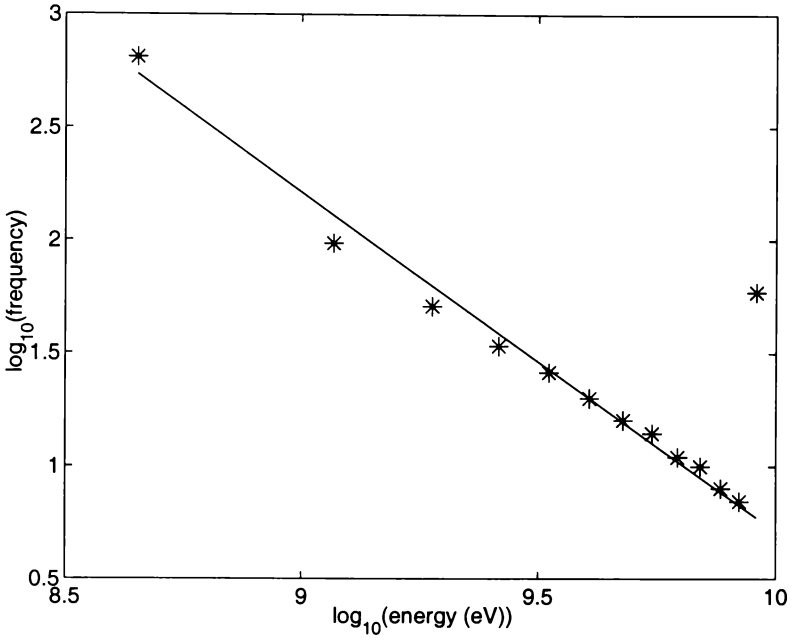

Figure 7.4: Spectrum obtained from the lower line of Figure 7.3, corresponding to the maximum energy attained by distributing 1000 *particles uniformly along the x-axis and releasing them from rest in the X-point field (7.10).*

The high energy end point which lies well above the reference line corresponds to the maximum energy acquired by all uncaptured particles.

7.3.3 Results for the reconnecting current sheet

Since the exact reconnection solution due to Craig and Henton provides a model for X-point reconnection, we might expect to achieve a spectrum in accordance with prediction (7.21). There are however, two key assumptions in the analytic argument which could compromise the energy scaling. In the first place, the calculated distribution is based on particle capture: if the Lorentz force is too weak to halt the acceleration before the particle exits the region, then such a particle will acquire the maximum energy $\mathcal{E}_{\max} = qEL_c$ defined by the size L_c of the computational box (see equation (7.13)). This situation will always apply for some interval close to the neutral point. In fact situations could arise where this interval covers the entire region and no spectrum would be achieved.

The analytic argument also assumes that initial conditions are chosen so that there is immediate downward acceleration in the weak field region where $B_\perp > B_x$. In fact this assumption, although unrealistic, may not be too critical since any particle placed near the current sheet will migrate into the weak field region due to the electric drift associated with the dominant reconnecting magnetic field

component B_x outside the current sheet (see Figure 7.2) and the constant electric field in the $-\hat{\mathbf{z}}$ direction. In this case a slow inward drift phase should precede the rapid **E**-field acceleration within the sheet.

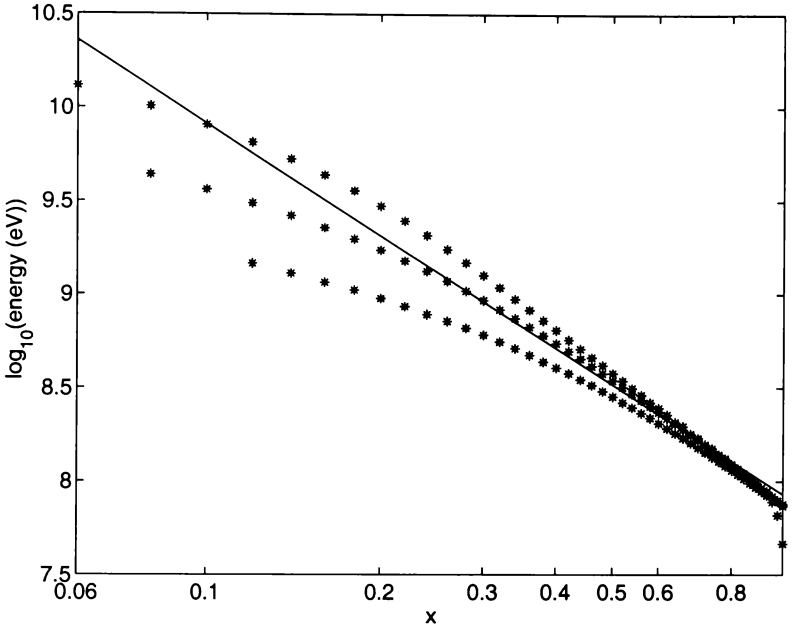

Figure 7.5: Final energy with initial position for 50 particles evenly distributed along the positive x axis of the Craig and Henton field of Section 3.2 and started from rest. The three lines represent, from top to bottom, $\eta = 10^{-6}$, $\eta = 10^{-7}$ and $\eta = 10^{-8}$ respectively. The solid line gives the scaling prediction (7.20). Note that we have only plotted the energy of the particles which are captured within our $-L_c$ to L_c cube.

Figure 7.5 shows the energy versus x-position diagram for the exact MHD solution. Three values of the resistivity are plotted. There is close agreement with the analytic non-relativistic scaling at low energies—here the individual curves are almost indistinguishable—but significant departures at relativistic energies are present. Note, however, that each curve represents a close approximation to the X-point model in the lower plot of Figure 7.3. The upper cut-off in each $\mathcal{E}(x)$ plot reflects the maximum energy gain (7.13) of a non-captured particle, and since $E \sim \eta^{1/2}$ the maximum energy gain must also scale in this way.

To interpret these results, first note that the low energy scaling is consistent with the capture condition, being invariant with η. That is, in the saturated solution, both E and $B_\perp = B_y$ (at fixed x) scale as $\eta^{1/2}$. Thus for a given initial position, the energy should remain invariant with η, at least provided that x is large enough for $B_\perp$ to be effectively constant prior to capture. At high energies, the scalings must separate to reflect the increased direct field acceleration of non-captured particles.

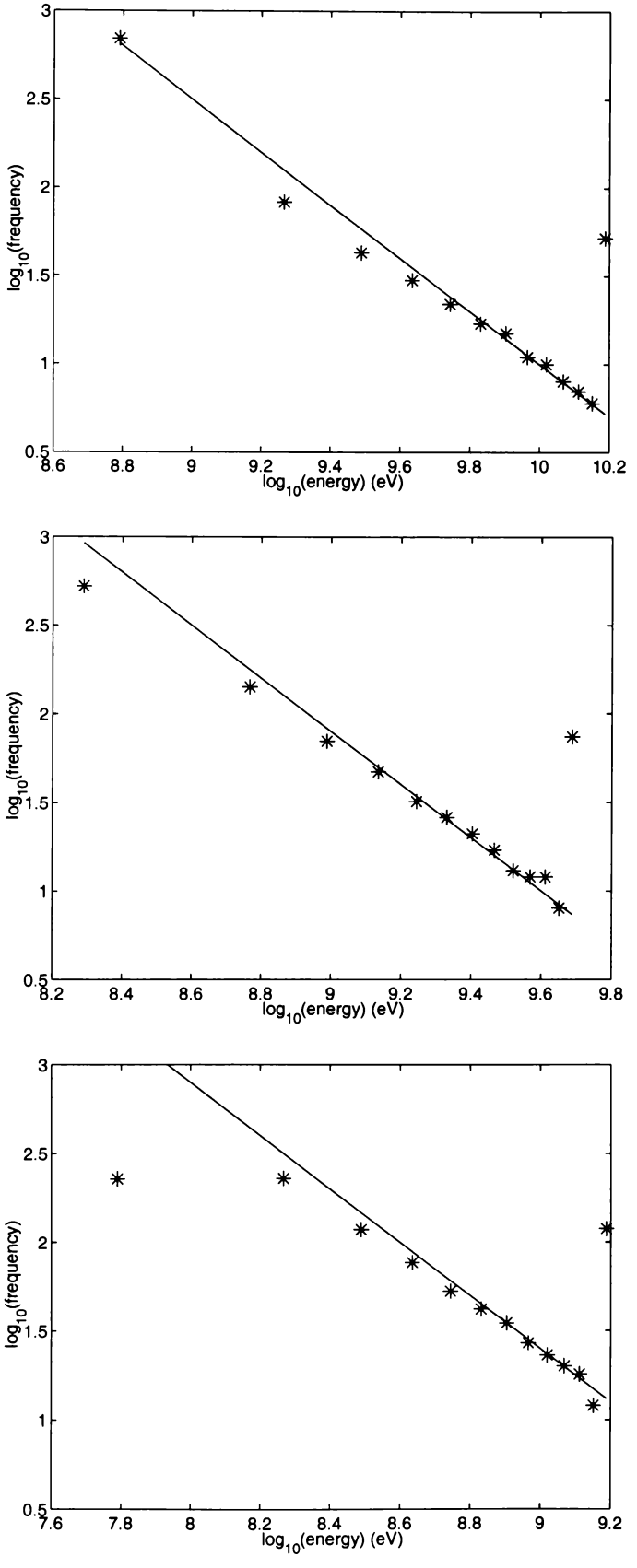

Figure 7.6: Spectra corresponding to the final energy of 1000 *particles distributed uniformly along the center of the current sheet of the Craig-Henton field. The plots represent three different runs with* $\eta = 10^{-6}$, 10^{-7} *and* 10^{-8} *from top to bottom. In all cases we have used* $\alpha = 3$, $\beta = 2$ *and each particle was given an initial speed* $0.1v_A$ *in a random direction.*

In turn each energy curve has to be consistent with the form of Figure 7.3.

Figure 7.6 shows the spectrum computed from the exact Craig-Henton solution. The spectrum, comprising 1000 particles released with a small random thermal energy of $0.1v_A$, is strikingly similar to the X-point spectrum of Figure (7.4). Again there is slight steepening at around $10^{9.5}$eV due to $\mathcal{E}(x)$ becoming less steep (see Figure 7.5) and a spike at the upper energy cut-off corresponding to non-captured particles. The low energy data point for $\eta = 10^{-8}$ is much smaller than expected because some of the low energy particles near the $x = 1$ end of the sheet escape the region without completing the acceleration phase.

The fact that the heuristic X-point spectrum manages to reproduce the main features of the steady-state reconnection solution confirms the assumption of previous studies, that X-point current sheet models can provide a useful platform for particle acceleration investigations. It should be remembered however, that the advantage of the exact solution used here is that the analysis is unambiguous, in the sense that it is uncompromised by extraneous parameterisations.

7.3.4 Resistive scalings

How does the maximum kinetic energy scale with resistivity? Note that the non-dimensional electric field saturates according to $E = \eta^{1/2} B_{\max}^{3/2}$ (Craig and Watson (2000b), and also Section 5.2). Thus using $\mathcal{E} = qEz_{\max}$ with $z_{\max} = L_c$ yields the limit

$$\mathcal{E} \simeq 3 \times 10^{12}\, \eta^{1/2}\, B_{\max}^{3/2}\ \text{eV}. \tag{7.23}$$

This suggests that inverse Lundquist numbers as small as 10^{-10} could be sufficient (taking $B_{\max} = 10$ corresponding to localised sheet fields of 10^3 gauss) to produce GeV protons. Such fields are in fact capable of producing flare-like Ohmic decay rates of 10^{28} ergs per second (Litvinenko and Craig, 2000).

Turning now to the acceleration time of a particle captured in the sheet, we recall that the acceleration length is simply the gyro-radius $cp/qB_\perp$. For non-relativistic motion the acceleration time is one half the gyro-period (the time to deepest electric field penetration from (7.17)) :

$$\tau_{\text{acc}} = \frac{\pi mc}{qB_\perp} \sim \eta^{-1/2}. \tag{7.24}$$

Note that, although the gamma factor must be included in the case of relativistic motion,

$$\tau_{\text{acc}} = \frac{\pi mc}{qB_\perp} \frac{B_\perp^2 + E^2}{B_\perp^2 - E^2}\ , \tag{7.25}$$

the (formal) scaling with resistivity due to $B_\perp(x)$ is not undone. However, the relativistic factor does alter the scaling coefficient. This result is confirmed by the

acceleration times plotted in Figure 7.7 for the Craig-Henton model. The weaker **E**-field acceleration at low resistivities leads to longer acceleration times.

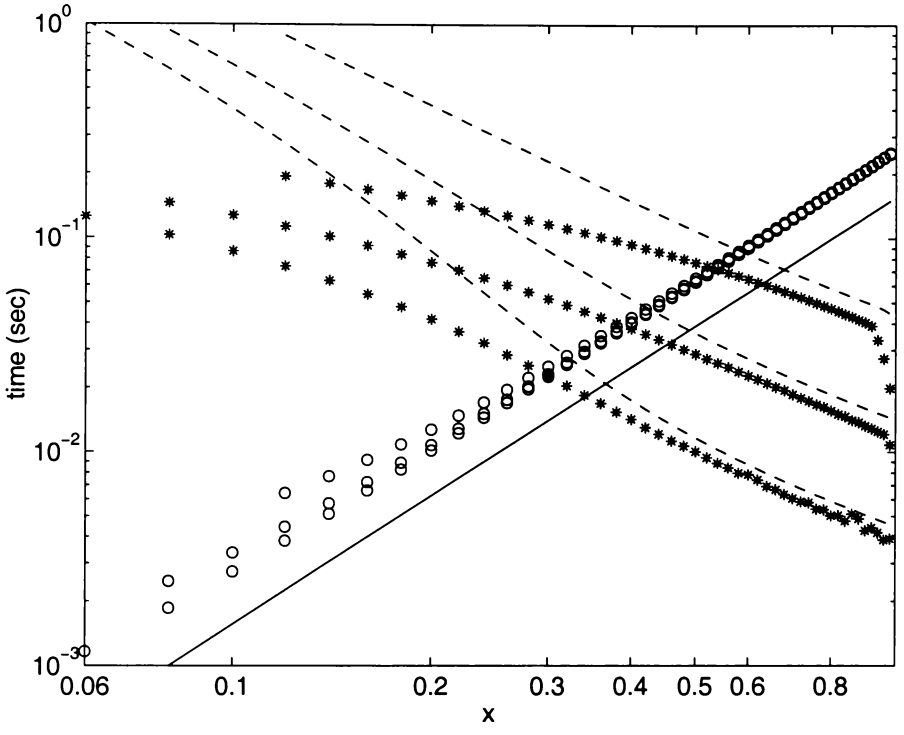

Figure 7.7: Drift time (o) and acceleration time (*) for three sets of particle simulations for $\eta = 10^{-6}$, 10^{-7} and 10^{-8}. The drift time is the same for all three runs (some slight error at small values of x is due to the error in estimating when the drift phase has finished), and is approximated by (7.26) which is plotted as the solid line. The dashed lines represent the analytic prediction (7.25).

Of course particles initially along the center line of the sheet (x-axis) must first drift into the weak field region before being accelerated. An estimate of this drift time can be made by taking the drift distance $\beta\eta x/Q_0$ (see Figure 7.2) and dividing by the initial drift speed $v_{\text{drift}} \simeq Q_0/(\beta x)$ to give

$$\tau_{\text{drift}} \simeq \frac{\eta\beta^2}{Q_0^2}x^2 \,. \tag{7.26}$$

The predictions (7.25) and (7.26) are plotted along with the observed values for $\eta = 10^{-6}$, 10^{-7} and 10^{-8} in Figure 7.7. The acceleration time prediction (7.25) agrees reasonably well for particles started away from the neutral point, since for these the implicit assumption of constant $B_\perp$ is approximately valid over the acceleration phase of each particle. The drift time prediction (7.26) is much simpler, but clearly still a consistent measure over the entire sheet.

The flux spectrum is of interest observationally. The flux of protons into the

acceleration region will be given by

$$\mathcal{F}_{\rm in} = 2L_z \int_{x_{\rm min}}^{x} v_{\rm in} n_{\rm in}\, {\rm d}x\ , \tag{7.27}$$

and will be the same as the outward flux of accelerated particles. Using $v_{\rm in} = v_{\rm drift} \simeq Q_0/(\beta x)$, $\mathcal{E}_{\rm in} = mv_{\rm in}^2/2$ and a uniform particle density $n_{\rm in}$, the flux may be written as

$$\mathcal{F}(\mathcal{E}_{\rm in}) = \frac{L_z n_{\rm in} Q_0}{\beta} \int_{\mathcal{E}_{\rm in}}^{\mathcal{E}_{\rm max}} \mathcal{E}^{-1} {\rm d}\mathcal{E}\ .$$

However, we are interested in the outward flux in terms of the final energy of the particles. We know, from (7.15) and the expression for $v_{\rm in}$ used above, that the inward and outward energies are related in the following way.

$$\mathcal{E}_{\rm out} = \frac{4Q_0^2}{\beta^2 \eta^2} \mathcal{E}_{\rm in} \tag{7.28}$$

Hence the particle flux in terms of the final energy will be

$$\mathcal{F}(\mathcal{E}) = \frac{L_z n_{\rm in} Q_0}{\beta} \ln\left(\frac{\mathcal{E}_{\rm max}}{\mathcal{E}}\right)\ , \tag{7.29}$$

where $\mathcal{E}$ is the final kinetic energy of each particle.

It is easiest to interpret this equation non-dimensionally by taking $L_z = 1$, $n_{\rm in} = 1$, $Q_0 = 5\sqrt{\eta}$ and $\beta = 2$. Concrete numbers are then obtained by taking $\mathcal{E}_{\rm max} = qEz_{\rm max} \simeq 2\sqrt{\eta} \times 10^{13}$ eV and the reference flux $n_c v_A L_c^2 = 10^{37}\ {\rm s}^{-1}$ to give

$$\mathcal{F}(\mathcal{E}) \simeq 2.5 \times 10^{37} \sqrt{\eta}\ \ln\left(\frac{1.6\sqrt{\eta} \times 10^{13}}{\mathcal{E}}\right)\ {\rm s}^{-1}, \tag{7.30}$$

where $\mathcal{E}$ is also measured in eV. From this we can see that the expected flux for protons above 1MeV will be about $1.8 \times 10^{34}\,{\rm s}^{-1}$ for $\eta = 10^{-8}$, with about 7% of these being above 1GeV. These numbers compare favourably with those mentioned in the introduction.

7.3.5 Orbit properties

The interpretations in the previous sections are reinforced by studying individual particle orbits. Figure 7.8 shows part of a typical particle orbit, comprising well defined inward drift, acceleration in the reconnection region, and capture phases. The particle starts from rest at $(0.4, 0, 0)$ and initially drifts slowly in the $-\hat{\mathbf{y}}$ direction, gyrating around the relatively strong reconnecting field B_x. When the particle reaches the weak field region where $B_x \approx B_\perp$, it is accelerated rapidly downwards by the strong **E**-field. This phase ends when the particle speed is sufficient for the Lorentz force to recapture the energised particle. In the final phase the particle exits the source volume, spiraling in the yz-plane, through the surface $x = 1$.

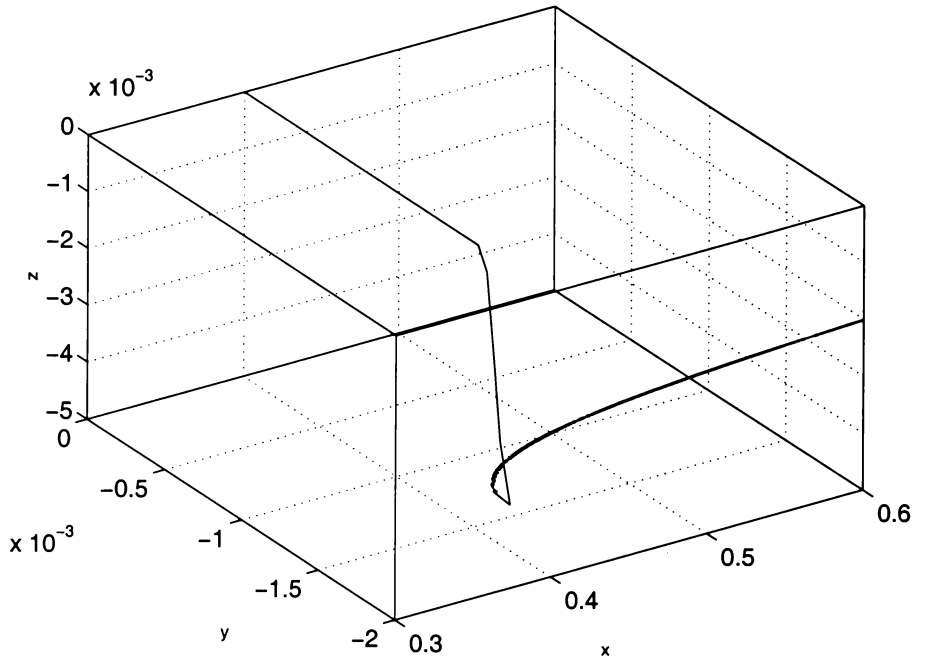

Figure 7.8: Orbit of particle started from rest at $(0.4, 0, 0)$. *Note the initial drift phase (motion in* y*), followed by the acceleration phase (motion in* z*), and concluded by the exit phase (motion in* x*).*

It should be noted that in all steady-state planar reconnection solutions, the electric field is constant everywhere (see equation 7.5). This begs the question, "is it possible to acquire significant acceleration outside the current sheet?". We have argued that significant acceleration is only possible if test particles can gain entry, if not by in situ placement then by slow drift, into the weak field exhaust of the reconnection mechanism.

More specifically, test particles placed well outside the current sheet will either drift into the exhaust region, and get accelerated in much the same way as particles placed inside the sheet, or simply drift out of the domain without a significant energy gain. Figure 7.9 shows the projection of such orbits in the xy-plane (there is little motion in the $\hat{\mathbf{z}}$ direction). As expected, the particles drift in the $\mathbf{E} \times \mathbf{B}$ direction and attain little energy outside the current sheet where the magnetic field is comparatively large. Only the particles which drift into the current sheet (originating in the lower left and upper right quadrants) will achieve significant acceleration.

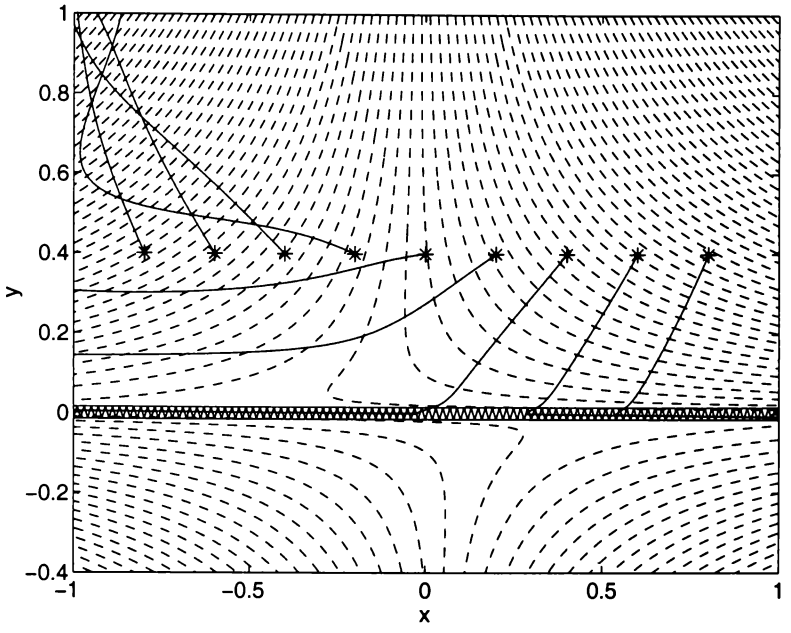

Figure 7.9: Trajectories of 9 particles started well outside the current layer (central jagged region). The dashed lines depict magnetic field lines. We find that only those particles which encounter the current sheet achieve significant acceleration.

7.4 Application to solar flares

Observations of events in the solar corona have led to the conclusion that the bulk of accelerated protons have energies within the range 0.1MeV to 10MeV. Earth based detectors now and then record protons coming from the sun with energies in the 1GeV to 5GeV range (Ryan, 2000). The particles with the highest energies typically come from the large gradual events which are most likely a consequence of magnetic field relaxation following a coronal mass ejection (CME). The CME is likely to generate a shock wave that contributes to particle acceleration. Significant observational evidence, however, suggests that at least some particles are energised in the current sheet formed in the wake of the CME (Klein and Trottet, 2001).

It has previously been shown (Litvinenko and Craig, 2000) that the Craig–Henton reconnection solution provides a physical model which seems capable of meeting the bulk flare energy requirements, assuming a realistic turbulent resistivity which corresponds to the inverse Lundquist number of order $\eta \sim 10^{-8}$. The analysis of the present paper demonstrates that the same current sheet may be the source of energetic protons in large solar flares. In particular, energies of order $\eta^{1/2}10^{13}$ eV are possible using flux pile-up fields of order 300 Gauss (Figure 7.5). Another prediction of the model is that the direct electric field acceleration in the current sheet provides not only the required proton energy but also the rate of energy gain. Equation (7.25) indicates that a typical proton acceleration time-scale is

of order 10^{-2} s, assuming a transverse magnetic field in the sheet of a few Gauss or smaller (Litvinenko, 1996). This compares favourably with time-scales $0.01 - 0.1$ s of rapid variation of flare gamma-radiation produced by energetic protons.

Solar observations also indicate the existence of an energy spectrum with a power-law or Bessel-function shape (Miller *et al.*, 1997). Traditional models, using relatively weak X-point fields account for such a spectrum via the magnetic field component perpendicular to the current sheet. Such models do not however, represent quasi-steady solutions to the MHD equations, nor do they possess the physical features—such as Alfvénic shear flows, magnetic sling shots and rapid Ohmic dissipation—expected of a plausible reconnection mechanism. It is encouraging therefore that the present model generates a power law spectrum which can be understood in terms of X-point acceleration, for which $\mathrm{d}n/\mathrm{d}\mathcal{E} \sim \mathcal{E}^{-3/2}$.

In analyzing particle spectra, we have noted that predictions obtained by using a non-relativistic approximation and assuming constant perpendicular magnetic field accord reasonably well with simulations in which we make neither assumption. From this it is clear that the relativistic effects and inhomogeneity in $B_\perp$ cancel each other out to some degree. We should also emphasise that although simple X-point models provide qualitatively similar results to the steady-state reconnection solution, these contain a number of arbitrary factors which cannot be interpreted in terms of the physical properties of reconnecting current sheets. For example, it is not clear how the field strength should be normalised, or what X-point angle should be used. We have shown here that detailed quantitative predictions can be made, unhindered by extraneous parameterisations, using an exact reconnection model.

Since the field model considered is essentially two dimensional, we can expect more refined three dimensional solutions to provide richer acceleration spectra. It is expected, in particular, that electrons can be easily magnetised by the non-planar magnetic field component $B_z \approx 0.1 B_x$ (Litvinenko, 1996), resulting in efficient electron acceleration to energies corresponding to X-ray and gamma-emission. Hence the reconnecting magnetic field geometry may be responsible for the electron-to-proton ratio as a function of energy. Another possible extension of this approach is through relaxing the steady-state assumption, using the available time-dependent generalisations of the Craig-Henton (Craig and Watson, 1999) model to investigate whether the accelerated particle spectra and composition can be a signature of time-dependent reconnection.

To conclude, we have studied test particle orbits in realistic reconnecting current sheets, described by an exact MHD solution for the magnetic fields and plasma flows. As an application, we considered proton orbits in two-dimensional geometries and demonstrated that non-thermal protons observed in solar flares can indeed be generated in a large-scale current sheet.

Chapter 8

Final summary

8.1 Discussion and conclusions

In this thesis we have looked at a range of magnetic reconnection models with the aim of understanding the current sheet mechanism thought to power a solar flare event. Although the corona was our focus, it should be remembered that reconnection also plays an important role in the Earth's geotail and man-made tokamak fusion devices.

We began by reviewing some of the early magnetic energy release models. Although these have various problems, their primitive nature means that they often utilise fundamental ideas. The Sweet-Parker model in particular, uses an order of magnitude analysis which captures the bulk features of any general merging model. For example, we saw in Section 5.2 that when saturation of the current layer is taken into account, the crude Sweet-Parker energy release rate scaling emerges from a far more sophisticated model.

Chapter 3 reviewed a family of exact two and three dimensional reconnection solutions. We started off deriving the 2-D reconnection solution of Craig and Henton (1995), which incorporates the earlier annihilation solution of Sonnerup and Priest (1975) in the limit of purely anti-parallel magnetic field. We then introduced the 3-D reconnection solutions of (Craig and Henton (1995); Craig, Fabling, Henton and Richard (1995); Craig and Fabling (1996)). These are formed from a superposition, in which a background potential field and a disturbance field are combined linearly to obtain the magnetic and velocity field solutions. This principle of superposition proved to be useful in the analytic work of Chapter 6, as well as in the numerical simulations of Chapters 4 and 5. Kinematic considerations (Lau and Finn, 1990), suggest that 3-D reconnection in general occurs with "spine" and "fan" structure, and these do indeed exist in the analytic solutions as expected.

Having introduced two and three dimensional steady-state analytic reconnection

solutions in Chapter 3, we went on in Chapter 4 to test these numerically using detailed merging simulations. We found that the Dawson function profile of the 2-D steady-state solution forms dynamically from general initial conditions. The analytic solution also predicts certain scalings with respect to the small resistive parameter η. By performing a sequence of runs at varying levels of resistivity we were able to verify that the scaling properties of 2-D analytic current sheets are reproduced from general initial conditions by the time-dependent code. Since we know from Section 3.3.6 that the 2-D solution extends naturally to include three dimensions and time-dependence, the 2-D simulations show that even the least refined model predicts current sheets whose forms manifest naturally in dynamic simulations. Note also that the analytic current sheets are infinitely long. What the 2-D simulations confirm is that the infinite extent of the analytic current sheet is not a fundamental requirement, since the finite length numerical sheets behave physically as predicted by the analytic model.

Three dimensional simulations were performed in Section 4.2. The main set-back with any 3-D numerical calculation is the excessive storage requirement. One way we tried to overcome this difficulty was to use finite differences with a high order of accuracy, so that less data points are required to resolve a given solution. The 3-D simulations show that spine and fan current structures, predicted analytically from the eigenstructure of the field at the neutral point, manifest time dependently from general initial conditions. Also ribbon current structures can be generated which correspond to separator currents predicted kinematically. As with the 2-D simulations, we also checked the scaling properties of the current layer. The scalings agree well with the analytic predictions of Chapter 3. The only puzzle is the need to keep viscosity fixed while resistivity is varied in the case of spine scalings.

Chapter 5 dealt with five different aspects of two dimensional merging not covered by the 2-D work of Sections 3.2 and 4.1. Section 5.1 represents a comparison of numerical reconnection solutions both with and without sheared flow profiles. The results of Section 3.2 and 4.1 tell us that the scalings of the current sheet do not depend on the degree of shear determined by β. However, the individual solution properties will depend on β. We found that the tendency for flux pile-up is reduced in the sheared case and correspondingly the current density is less intense. As Figure 5.1 shows, however, the exhaust region of the sheared configuration is much larger, which allows material to be more readily evacuated from the reconnection zone. Also, since the flux pile-up effect is reduced, we would expect sheared solutions to saturate for smaller values of η.

The idea of pressure saturation within the current layer was discussed in Section 5.2. We showed that the total pressure within the current sheet cannot exceed some maximum value determined by external conditions. Numerically this limit is

reflected in the magnitude of the hydromagnetic pressure on the inflow boundary. This implies that the peak magnetic field will tend to increase with reduction in resistivity until it reaches a saturated level, after which it remains constant if η is further reduced. We then showed that the Ohmic dissipation rate goes from a "fast" scaling in the pre-saturation regime, to a "slow" scaling post saturation. The dissipation rate results also showed that although the size of the disturbance amplitude determines at what value of η a given solution will saturate, consecutive W_η maxima conform to the slow $\eta^{1/2}$ Sweet-Parker rate. One of the important analytic findings, however, was that in general we will have an amplification factor $B^2_{\max}$ as part of the dissipation rate, giving rise to 100 times more dissipation than the corresponding Sweet-Parker solution if the pile-up field saturates at 1000G. More importantly, if we assume some pressure equalisation of the inflow and outflow (as Sweet-Parker does) the scalings are modified from the values given in Section 3.2.2 to yield a thinner current whose width scales as $\eta^{2/3}$. Not only does equalisation give rise to an even greater amplification factor, but the fact that the sheet is thinner means that anomalous effects (which are expected to greatly enhance dissipation) set in at a higher values of η.

In Section 5.3 we investigated the effects of finite compressibility on the form of the 2-D solutions considered so far. Due to the presence of various wave phenomena, we were forced to employ a flux corrected transport algorithm as part of the numerical code. We found that the basic form of the solutions was unchanged and that the incompressible results were recovered as the plasma beta became large. In order to investigate the dynamic ramifications of finite compressibility, we did a sequence of runs with varying levels of compressibility. In each run we traced several diagnostic quantities from the initial condition to well after the central current sheet had dissipated. We found that there are essentially three regimes for values of β_p. When $\beta_p \gg 1$ the solution behaves almost incompressibly, localising in around 1 Alfvén time similar to the solutions in Section 4.1. When $\beta_p \simeq 1$ the sound speed and Alfvén speed are comparable. In this case diagnostic quantities may be increased or decreased, depending on whether a sound wave is reinforcing or canceling the magnetic localisation. As β_p is reduced below 1 the plasma behaves very much as though it is arbitrarily compressible, since the average sound speed is now slower than the localisation speed. The key result of all these runs, however, is that the Ohmic dissipation rate (as integrated over the entire region) is approximately the same for all values of β_p. This suggests that the incompressible dissipation rate results are equally valid in the case of compressible reconnection.

In Section 5.4 we discussed field line osculation within a 2-D current layer, modifying the analysis of Priest and Cowley (1975) to include time dependence. This showed that even when the level of viscosity is set to zero, osculation will be avoided

due to the time dependent terms in the expansion. As numerical evidence we performed several runs at varying levels of viscosity and at a range of resolutions. These confirmed that the term required to vanish for osculation in fact converges to a well defined value even when viscosity is absent, this term being balanced by the time dependent terms. We conclude that in general osculation is a strictly steady-state effect.

The final section of Chapter 5 focuses on the tearing mode instability. This section concentrates mainly on finding numerical evidence of tearing. As such we performed an independent check of one of Biskamp's (1994) runs in which he appears to see the fragmentation of a current sheet. Our results compared very well to Biskamp's at early times. However at later times we did not see the same fragmentation. This discrepancy could be due to the fact that Biskamp uses a more diffusive "hyper resistivity" instead of the ordinary resistivity we employ. Closer inspection of the current sheet in question, however, revealed that it is generated by a sliver of reverse flux being squashed between two cells of like flux. We concluded that this configuration does not represent the classical idea of a tearing instability which develops between layers of anti-parallel magnetic field. We then went on to search for sheet fragmentation in the context of head-on reconnection. These results were negative and so we turned our attention to sheared geometries. Here we found a pair of magnetic islands forming within current sheets that have nearly dissipated. The islands only formed for sufficiently low values of η, consistent with the tearing mode requirement of a thin current sheet. We conclude, however, that since the islands form when the sheet has almost dissipated, we are unclear if the tearing instability is the cause.

In Chapter 6 we extended the analytic forms of the background and disturbance fields to incorporate multiple nulls. The prime motivation was to obtain solutions which include multiple length scales, so that more current structures may form on null-null lines. Working with a spine-type disturbance, we found that in general the cylindrical background field may contain an arbitrary number of rings of nulls. We then investigated the properties of a configuration with a single null at the origin, surrounded by a ring of three satellite nulls. We found that, despite the presence of current sheets along null-null lines, the spine scaling of the central null dominates the solution and as such has little dissipatory advantage over the single null models of Chapter 3. We then went on to examine solutions which involve multiple rings of satellite nulls. These do show current structures confined between two neutral points. Looking at a specific example, we showed that, by altering one of the free parameters, a variety of field structures can be generated, while keeping the overall length scale fixed using the second free parameter. We found that the central null exhibits aspects of spine, fan and separator reconnection as this free parameter is

varied. We conclude that the multiple null analysis provides an analytic prescription for the three basic types of reconnection and that the presence of multiple nulls does allow current sheets of finite length to form (though they are still infinite in the ignorable direction).

In Chapter 7 we investigated particle orbits in X-type magnetic fields, representing a departure from the MHD focus of the other chapters. The aim was to calculate the energy spectrum of protons, assuming a magnetic configuration corresponding to the Craig-Henton solution of Chapter 3. We began by investigating the properties of orbits arising from the classic X-point field. These types of fields have been studied in the past, but obtaining consistent energy figures is difficult since such fields are not physically realisable so that there is no clear way to set the field strength or X-point angle. The aim of our X-point calculations was to enable qualitative comparisons with Craig-Henton results while at the same time providing a suitable test for the code. We ran our code keeping the magnetic field fixed over the entire orbit. These results agreed exactly with the relativistic analytic prediction and showed that the energy gain of particles becomes unbounded when the level of magnetic field drops below that of the electric field. When the magnetic field was allowed to vary with position in the natural way, the results far away from the neutral point remained unchanged, while particles started close to the neutral point were captured much sooner due to them experiencing increasing fields over the orbit. The X-point spectrum showed good agreement with the non-relativistic prediction which assumes fixed magnetic field over each orbit. We conclude that this agreement is due to the relativistic effects being canceled out to some extent by the field inhomogeneities.

We then turned our attention to proton acceleration in the exact Craig-Henton field solution. To make this solution physically consistent we incorporated the ideas of saturation and equalisation introduced in Section 5.2. The energy gain results showed good qualitative agreement with the X-point results, despite each particle having to initially drift into the weak field region where efficient acceleration can occur. The spectrum too showed the same qualitative behaviour. We obtained results for the Craig-Henton configuration for three values of the "effective" resistivity ($\eta_{\text{eff}} = 10^{-6}$, 10^{-7} and 10^{-8}) which we assume will give current sheet properties which mimic those obtained from non-collisional considerations. These showed that the upper energy cut-off decreases as η_{eff} is reduced while η_{eff} has no effect on the lower energy spread. Using these results we went on to predict the proton energy flux. We calculated that for $\eta_{\text{eff}} = 10^{-8}$ a flux of $1.8 \times 10^{34}\,\text{s}^{-1}$ for protons above 1MeV could be expected, with 7% of these being above 1GeV. These values agree favourably with observational data as mentioned in Chapter 1. We conclude that the electric field associated with reconnecting current sheets can provide proton en-

ergies consistent with observations. The fact that recent studies (Klein and Trottet, 2001) have confirmed that at least some particles are accelerated in coronal current sheets, as opposed to the shock wave associated with magnetic collapse, adds weight to our approach.

8.2 Suggestions for further work

The work in this thesis lends itself to extension in several places. Firstly, the effects of viscosity on the numerical 3-D spine solution of Chapter 4 requires further investigation. At this point it is not clear why the scaling results should be very different when we scale viscosity with resistivity, compared to holding viscosity fixed. Certainly all other two and three dimensional scalings work equally well in both regimes.

A second possibility for further work is to try to introduce the idea of anomalous resistivity into the reconnection models. This could take the form of a definition for the resistivity in terms of local current intensity. The analysis will of course become more difficult, but it should be relatively straight forward to include varying resistivity in a numerical code. This would provide a first step to understanding the transition from collisional to anomalous dissipation rates.

The compressible results of Section 5.3 are encouraging. They show that merging is qualitatively similar irrespective of the plasma beta. What Figure 5.17 shows, however, is that there are still some numerical difficulties to overcome. As such further work could include extensions to the code to improve it's accuracy. Since the configurations considered are "head-on", the code may be set up to take advantage of the symmetry so that higher resolutions can be more easily achieved. It would also be useful to have a self-consistent initial density profile that incorporates the level of compressibility in some way.

The final area for further work is the particle study of Chapter 7. The idea of using exact reconnection solution as the basis for acceleration experiments is still in its infancy. Future studies should include a constant magnetic field component perpendicular to the flow. It is predicted that electrons in particular can be efficiently accelerated by the inclusion of such a perpendicular field component. Of course our prescription can easily incorporate the fully three dimensional analytic solutions of Chapter 3 and these are expected to provide much richer particle dynamics.

Appendix A

Stability analysis for the 3-D code

Here we investigate the time-step condition for the Russian scheme using fourth-order differencing. The Russian scheme, which we employ in the 2-D, 3-D and 2-D compressible finite difference codes, is very similar to Lax-Wendroff, except that it uses "spread-out" differences as opposed to LW's compact differences. This adds some extra diffusion to the solution, making it more robust in situations where numerical artifacts may arise, while still retaining the same order of spatial accuracy. However, LW is second order accurate in time, while the Russian scheme is only first order in time. The scheme can be written to solve the advection equation

$$u_t = cu_x$$

as a two step predictor-corrector method in the following way.

$$\begin{aligned} u_j^{n+1*} &= u_j^n + c\mu\delta_j(u^n) \\ u_j^{n+1} &= u_j^n + c\mu\delta_j(u^{n+1*}) \end{aligned} \tag{A.1}$$

Here $\delta_j(u)$ is the difference operator of the desired accuracy (for example $\delta_j = (u_{j+1} - u_{j-1})/2$ for a standard second order central difference), and $\mu = \Delta t/\Delta x$.

Advection equation stability

We now derive the time-step requirement for the advection component of our solution assuming fourth-order differences are used. Firstly we analyse the 1-D case in detail, before extending this to three dimensions.

1-D Advection

Rewriting (A.1) with fourth-order derivatives we have

$$u_j^{n+1*} = u_j^n + \frac{c\mu}{12}\left(u_{j-2}^n - 8u_{j-1}^n + 8u_{j+1}^n - u_{j+2}^n\right)$$

$$\begin{aligned} u_j^{n+1} &= u_j^n + \frac{c\mu}{12}\left(u_{j-2}^{n+1*} - 8u_{j-1}^{n+1*} + 8u_{j+1}^{n+1*} - u_{j+2}^{n+1*}\right) \\ &= u_j^n + \frac{c\mu}{12}\left(u_{j-2}^{n} - 8u_{j-1}^{n} + 8u_{j+1}^{n} - u_{j+2}^{n}\right) \\ &+ \left(\frac{c\mu}{12}\right)^2\left(u_{j-4}^n - 16u_{j-3}^n + 64u_{j-2}^n + 16u_{j-1}^n\right. \\ &\left. - 130u_j^n + 16u_{j+1}^n + 64u_{j+2}^n - 16u_{j+3}^n + u_{j+4}^n\right) . \end{aligned}$$

Following a von Neumann stability analysis for a periodic domain we now set

$$u_j^n = \xi^n e^{ikx_j} \tag{A.2}$$

from which we find

$$\begin{aligned} \xi &= 1 + \frac{c\mu}{12}\left(e^{-2k\Delta x} - 8e^{-k\Delta x} + 8e^{k\Delta x} - e^{2k\Delta x}\right) \\ &+ \left(\frac{c\mu}{12}\right)^2\left(e^{-2k\Delta x} - 8e^{-k\Delta x} + 8e^{k\Delta x} - e^{2k\Delta x}\right)^2 . \end{aligned}$$

Taking $\theta = k\Delta x$, we have

$$\begin{aligned} \xi &= 1 + \frac{c\mu}{12}\Big(- 2i\sin(2\theta) + 16i\sin(\theta)\Big) - \left(\frac{c\mu}{12}\right)^2\Big(- 2\sin(2\theta) + 16\sin(\theta)\Big)^2 \\ &= 1 + \frac{c\mu}{3}i\sin(\theta)\Big(4 - \cos(\theta)\Big) - \left(\frac{c\mu}{3}\right)^2\sin^2(\theta)\Big(4 - \cos(\theta)\Big)^2 . \end{aligned} \tag{A.3}$$

We can now find the magnitude of ξ as follows.

$$\begin{aligned} \xi^2 &= \xi\bar{\xi} \\ &= \left[1 - \left(\frac{c\mu}{3}\right)^2\sin^2(\theta)(4 - \cos(\theta))^2\right]^2 + \left[\left(\frac{c\mu}{3}\right)\ \sin(\theta)(4 - \cos(\theta))\right]^2 \\ &= 1 + \left(\frac{c\mu}{3}\right)^2\sin^2(\theta)(4 - \cos(\theta))^2\left(\left(\frac{c\mu}{3}\right)^2\sin^2(\theta)(4 - \cos(\theta))^2 - 1\right) \end{aligned}$$

Since (A.2) represents the time evolution of a single Fourier mode, we require $\xi^2 \leq 1$ for stability. Hence we must have

$$\left(\frac{c\mu}{3}\right)^2\sin^2(\theta)(4 - \cos(\theta))^2 \leq 1 ,$$

which implies

$$c\mu^2 \leq \frac{9}{\max(\sin^2(\theta)(4 - \cos(\theta))^2)} = \frac{12}{3 + 8\sqrt{6}} .$$

Hence for stability we require

$$\Delta t < 0.72\frac{\Delta x}{c} . \tag{A.4}$$

This is a slightly stricter requirement than the standard result $\Delta t < \dfrac{\Delta x}{c}$ (CFL condition) when second order differences are used.

3-D Advection

Here we extend the stability analysis of the previous section for the Russian (A.1) scheme using fourth-order differences in three dimensions to solve

$$u_t = au_x + bu_y + cu_z \ .$$

The basic expansion will be similar, except that we now have terms with mixed derivatives. Setting $\mu = \Delta t/\Delta x$ and assuming $\Delta x = \Delta y = \Delta z$, we have

$$\begin{aligned} u_{ijk}^{n+1} = u_{ijk}^n \ &+ \ a\mu\delta_x u_{ijk}^n + b\mu\delta_y u_{ijk}^n + b\mu\delta_z u_{ijk}^n \\ &+ \ a^2\mu^2\delta_{xx}u_{ijk}^n + b^2\mu^2\delta_{yy}u_{ijk}^n + c^2\mu^2\delta_{zz}u_{ijk}^n \\ &+ \ 2ab\mu^2\delta_{xy}u_{ijk}^n + 2ac\mu^2\delta_{xz}u_{ijk}^n + 2bc\mu^2\delta_{yz}u_{ijk}^n \ . \end{aligned}$$

If we now take $\theta_1 = i\Delta x$, $\theta_2 = j\Delta x$ and $\theta_3 = k\Delta x$, and

$$\begin{aligned} A &= \frac{a\mu}{3}\sin(\theta_1)(4-\cos(\theta_1)) \\ B &= \frac{b\mu}{3}\sin(\theta_2)(4-\cos(\theta_2)) \\ C &= \frac{c\mu}{3}\sin(\theta_3)(4-\cos(\theta_3)) \ , \end{aligned}$$

equation (A.3) from the 1-D analysis becomes

$$\begin{aligned} \xi &= 1 + (A+B+C)i - A^2 - B^2 - C^2 - 2AB - 2AC - 2BC \\ &= 1 + (A+B+C)i - (A+B+C)^2 \ . \end{aligned}$$

Hence we have

$$\begin{aligned} \xi^2 &= \xi\bar{\xi} \\ &= \left[1-(A+B+C)^2\right]^2 + \left[A+B+C\right]^2 \\ &= 1 + 2(A+B+C)^2\left[(A+B+C)^2 - 1\right] \ . \end{aligned}$$

Hence for $\xi^2 < 1$ we require

$$(A+B+C)^2 < 1 \ .$$

Since $|\sin(\theta)(4-\cos(\theta))| \le (6\sqrt{6}+9/4)^{1/2}$, this gives

$$\left(\frac{4.12}{3}\mu\right)^2 (a+b+c)^2 < 1 \ .$$

So for stability we must have

$$\Delta t < 0.72\frac{\Delta x}{|a+b+c|} \ .$$

Since

$$|(a,b,c)\cdot(1,1,1)| \le |(a,b,c)||(1,1,1)| = \sqrt{a^2+b^2+c^2}\sqrt{3} \ ,$$

from the Cauchy-Schwartz inequality, we can write the stability condition as

$$\Delta t < 0.72\frac{\Delta x}{\sqrt{3(a^2+b^2+c^2)}} \ . \tag{A.5}$$

Stability of diffusion equation using fourth-order differencing

When solving the MHD equations numerically, both advection and diffusion time scales need to be considered. Having established the time-step criterion for stability of the advective component in the previous section, we now turn our attention to the diffusion time-scale.

1-D Diffusion

As for the advective case, we will calculate the time-step criterion for the 1-D problem first, before attempting the fully 3-D case. Substituting fourth-order differences into

$$u_t = \eta u_{xx}$$

we have

$$\begin{aligned} u_j^{n+1} &= u_j^n + \frac{\eta\Delta t}{144\Delta x^2}\Big(u_{j-4}^n - 16u_{j-3}^n + 64u_{j-2}^n + 16u_{j-1}^n \\ &\quad -130u_j^n + 16u_{j+1}^n + 64u_{j+2}^n - 16u_{j+3}^n + u_{j+4}^n\Big) . \end{aligned}$$

Note that we use the "non-compact" second derivative. As we stated in Section 4.2, we find this is required to conserve $\nabla \cdot \mathbf{B} = \nabla \cdot \mathbf{v} = 0$.

Substituting

$$u_j^n = \xi^n e^{ikx_j}$$

into the numerical scheme gives us the following formula for ξ.

$$\xi = 1 + \frac{\eta\Delta t}{144\Delta x^2}\left(e^{-2k\Delta x} - 8e^{-k\Delta x} + 8e^{k\Delta x} - e^{2k\Delta x}\right)^2$$

Taking $\theta = k\Delta x$, we have

$$\begin{aligned} \xi &= 1 + \frac{\eta\Delta t}{144\Delta x^2}\Big[-2i\sin(2\theta) + 16i\sin(\theta)\Big]^2 \\ &= 1 - \frac{\eta\Delta t}{9\Delta x^2}\Big[\sin(\theta)(4-\cos(\theta))\Big]^2 . \end{aligned} \tag{A.6}$$

Hence for $|\xi| < 1$ we require

$$\frac{\eta\Delta t}{9\Delta x^2}\sin^2(\theta)(4-\cos(\theta))^2 < 2 ,$$

so that the time-step criterion becomes

$$\Delta t < \frac{18\Delta x^2}{\eta \max(\sin^2(\theta)(4-\cos(\theta))^2)} = \frac{24}{3+8\sqrt{6}}\frac{\Delta x^2}{\eta} \simeq 1.06\frac{\Delta x^2}{\eta} . \tag{A.7}$$

The above requirement is more favourable than the standard result $\Delta t < 0.5\dfrac{\Delta x^2}{\eta}$ in the case of second order differencing. This is a consequence of the spread-out differences used here.

3-D Diffusion

Let us now extend the above analysis to solve the three dimensional diffusion equation

$$u_t = \eta u_{xx} + \eta u_{yy} + \eta u_{zz} \ .$$

Unlike the CFL analysis of the previous section, the absence of mixed derivatives greatly simplifies the situation. Clearly in this case expression (A.6) becomes

$$\begin{aligned} \xi &= 1 - \frac{\eta \Delta t}{9\Delta x^2}\Big([\sin(\theta_1)(4 - \cos(\theta_1))]^2 \\ &\quad + [\sin(\theta_2)(4 - \cos(\theta_2))]^2 + [\sin(\theta_3)(4 - \cos(\theta_3))]^2 \Big) \ , \end{aligned}$$

where $\theta_1 = k_1 \Delta x$, $\theta_2 = k_2 \Delta x$ and $\theta_3 = k_3 \Delta x$. Since

$$[\sin(\theta)(4 - \cos(\theta))]^2 \leq 6\sqrt{6} + 9/4 \ ,$$

the requirement for $|\xi| < 1$ is

$$\frac{\eta \Delta t}{9\Delta x^2}\left(18\sqrt{6} + \frac{27}{4}\right) < 2 \ .$$

Hence the 3-D diffusion time-step limit is given by

$$\Delta t < 1.06 \frac{\Delta x^2}{3\eta} \ . \tag{A.8}$$

Appendix B

Compressible MHD equations in conservative form

In order to find numerical solutions to the MHD equations we need to be able to write them in conservative form. We derive the conservative forms here for completeness, as these have been used in numerical simulations throughout this thesis.

The equations we solve are:

$$\frac{\partial \rho}{\partial t} + \nabla \cdot (\rho \mathbf{v}) = 0 \tag{B.1}$$

$$\rho \left[\frac{\partial \mathbf{v}}{\partial t} + (\mathbf{v} \cdot \nabla)\mathbf{v} \right] + \nabla p - \mathbf{J} \times \mathbf{B} = \nu \left(\nabla^2 \mathbf{v} + \frac{1}{3} \nabla (\nabla \cdot \mathbf{v}) \right) \tag{B.2}$$

$$\frac{\partial \mathbf{B}}{\partial t} - \nabla \times (\mathbf{v} \times \mathbf{B}) = \eta \nabla^2 \mathbf{B} \tag{B.3}$$

Note that here the viscous term has an extra component $\frac{1}{3}\nu\nabla(\nabla \cdot \mathbf{v})$ due to compressibility, which comes from the stress tensor of the fluid (see for example Shercliff (1965, §2.8)).

We will take

$$\mathbf{v} = (u, v, w) \quad , \qquad \mathbf{B} = (X, Y, Z) \, .$$

The first equation (B.1) can clearly be written as

$$\partial_t \rho + \partial_x (\rho u) + \partial_y (\rho v) + \partial_z (\rho w) = r_0 \, . \tag{B.4}$$

The first component of equation (B.2) implies

$$\rho u_t + \rho u u_x + \rho v u_y + \rho w u_z + p_x + Y Y_x - Y X_y + Z Z_x - Z X_z = r_1 \, .$$

Here r_0 represents the first component of the right hand side vector of the conservative system, while r_1 to r_6 will be the remaining components. Adding to this u times equation (B.4) as well as subtracting $X \nabla \cdot \mathbf{B}$ $(= 0)$ gives

$$\begin{aligned} \rho_t u + \rho u_t + \rho_x u^2 + 2\rho u u_x + \rho_y u v + \rho u v_y + \rho u_y v + \rho_z u w + \rho u w_z + \rho u_z w & \\ + p_x + Y Y_x - Y X_y - X X_x - X Y_y + Z Z_x - Z X_z - X X_z &= r_1 \, , \end{aligned}$$

which can be written as

$$\begin{aligned} \partial_t(\rho u) + \partial_x(\rho u^2 + Y^2/2 + Z^2/2 - X^2/2 + p) & \\ +\partial_y(\rho uv - XY) + \partial_z(\rho uw - XZ) &= r_1 \,. \end{aligned} \tag{B.5}$$

By symmetry (under the transformation $x \to y \to z \to x$ etc.) the second and third components must be

$$\begin{aligned} \partial_t(\rho v) + \partial_y(\rho v^2 + X^2/2 + Z^2/2 - Y^2/2 + p) & \\ +\partial_x(\rho uv - XY) + \partial_z(\rho vw - YZ) &= r_2 \end{aligned} \tag{B.6}$$

$$\begin{aligned} \partial_t(\rho w) + \partial_z(\rho w^2 + X^2/2 + Y^2/2 - Z^2/2 + p) & \\ +\partial_x(\rho uw - XZ) + \partial_y(\rho vw - YZ) &= r_3 \,. \end{aligned} \tag{B.7}$$

The components of equation (B.3) are

$$\partial_t(X) + \partial_y(vX - uY) + \partial_z(wX - uZ) = r_4 \tag{B.8}$$

$$\partial_t(Y) + \partial_x(uY - vX) + \partial_z(wY - vZ) = r_5 \tag{B.9}$$

$$\partial_t(Y) + \partial_x(uY - vX) + \partial_y(vZ - wY) = r_6 \,. \tag{B.10}$$

We can write these in the following conservative form:

$$\frac{\partial \mathbf{U}}{\partial t} + \frac{\partial \mathbf{F}}{\partial x} + \frac{\partial \mathbf{G}}{\partial y} + \frac{\partial \mathbf{H}}{\partial z} = \mathbf{R} \,,$$

where

$$\mathbf{U} = \begin{pmatrix} \rho \\ \rho u \\ \rho v \\ \rho w \\ X \\ Y \\ Z \end{pmatrix}, \quad \mathbf{F} = \begin{pmatrix} \rho u \\ \rho u^2 + \frac{1}{2}(Y^2 + Z^2 - X^2) + p \\ \rho uv - XY \\ \rho uw - XZ \\ 0 \\ uY - vX \\ uZ - wX \end{pmatrix},$$

$$\mathbf{G} = \begin{pmatrix} \rho v \\ \rho uv - XY \\ \rho v^2 + \frac{1}{2}(X^2 + Z^2 - Y^2) + p \\ \rho vw - YZ \\ vX - uY \\ 0 \\ vZ - wY \end{pmatrix}, \quad \mathbf{H} = \begin{pmatrix} \rho w \\ \rho uw - XZ \\ \rho vw - YZ \\ \rho w^2 + \frac{1}{2}(X^2 + Y^2 - Z^2) + p \\ wX - uZ \\ wY - vZ \\ 0 \end{pmatrix}$$

and the right hand side vector $\mathbf{R} = (r_0, r_1, r_2, r_3, r_4, r_5, r_6)$ is given by

$$\mathbf{R} = \begin{pmatrix} 0 \\ \nu(\nabla^2 u + \frac{1}{3}\partial_x(u_x + v_y + w_z)) \\ \nu(\nabla^2 v + \frac{1}{3}\partial_y(u_x + v_y + w_z)) \\ \nu(\nabla^2 w + \frac{1}{3}\partial_z(u_x + v_y + w_z)) \\ \eta\nabla^2 X \\ \eta\nabla^2 Y \\ \eta\nabla^2 Z \end{pmatrix}.$$

References

Alekseev, I.I. and Kropotkin, A.P., "Passage of energetic particles through a magnetohydrodynamic discontinuity surface." *Geomagnetism and Aeronomy* **10**, 755 (1970).

Bentley, R.D. and Mariska, J.T., Magnetic reconnection in the solar atmosphere. San Francisco, California: Astronomical Society of the Pacific (1996).

Biskamp, D., "Magnetic reconnection via current sheets." *Phys. Fluids* **29**, 1520 (1986).

Biskamp, D., Nonlinear magnetohydrodynamics. Cambridge: Cambridge University Press (1993).

Biskamp, D., "Magnetic reconnection." *Phys. Reports* **237**, 181 (1994).

Bray, R.J. and Loughhead, R.E., Sunspots. New York: Dover (1979).

Bruhwiler, D.L. and Zweibel, E.G., "Energy spectrum of particles accelerated near a magnetic x line." *J. Geophys. Res.* **97A**, 10825 (1992).

Bulanov, S.V., "The energy spectrum of particles accelerated near a singular magnetic field line." *Soviet Astron. Lett.* **6**, 206 (1980).

Bulanov, S.V. and Sasorov, P.V., "Energy spectrum of particles accelerated in the neighborhood of a line of zero magnetic field." *Soviet Astron.* **19**, 464 (1976).

Chen, J. and Palmadesso, P.J., "Chaos and nonlinear dynamics of single-particle orbits in a magnetotaillike magnetic field." *J. Geophys. Res.* **91A**, 1499 (1986).

Craig, I.J.D. and Fabling, R.B., "Exact solutions for steady-state, spine and fan reconnection." *Astrophys. J.* **462**, 969 (1996).

Craig, I.J.D. and Fabling, R.B., "Dynamic magnetic reconnection in three space dimensions: Fan current solutions." *Phys. Plasmas* **5**, 635 (1998).

Craig, I.J.D., Fabling, R.B., Heerikhuisen, J. and Watson, P.G., "Magnetic reconnection solutions in the presence of multiple nulls." *Astrophys. J.* **523**, 838 (1999).

Craig, I.J.D., Fabling, R.B., Henton, S.M. and Rickard, G.J., "An exact solution for steady-state magnetic reconnection in 3D." *Astrophys. J. Letters* **455**, L197 (1995).

Craig, I.J.D., Fabling, R.B. and Watson, P.G., "The power output of spine and fan magnetic reconnection solutions." *Astrophys. J.* **485**, 383 (1997).

Craig, I.J.D. and Henton, S.M., "Exact solutions for steady-state incompressible magnetic reconnection." *Astrophys. J.* **450**, 280 (1995).

Craig, I.J.D. and McClymont, A.N., "Dynamic magnetic reconnection at an X-type neutral point." *Astrophys. J. Letters* **371**, L41 (1991).

Craig, I.J.D. and McClymont, A.N., "Magnetic energy release in dynamic fan reconnection models." *Astrophys. J.* **510**, 1045 (1999).

Craig, I.J.D. and Watson, P.G., "Fast dynamic reconnection at X-type neutral points." *Astrophys. J.* **393**, 385 (1992).

Craig, I.J.D. and Watson, P.G., "Dynamic planar magnetic reconnection solutions for incompressible plasmas." *Astrophys. J.* **516**, 924 (1999).

Craig, I.J.D. and Watson, P.G., "Flare-like energy release by flux pile-up reconnection." *Solar Phys.* **191**, 361 (2000a).

Craig, I.J.D. and Watson, P.G., "Optimized magnetic reconnection solutions in three dimensions." *Solar Phys.* **194**, 251 (2000b).

DeLuca, E.E. and Craig, I.J.D., "Magnetic reconnection in incompressible fluids." *Astrophys. J.* **390**, 679 (1992).

Demoulin, P., Mandrini, C.H., van Driel-Gesztely, L., Priest, E.R., Henoux, J.C. and Schmieder, B., "3D magnetic reconnection: Example of an X-ray bright point." In R.D. Bentley and J.T. Mariska, editors, "Magnetic Reconnection in the Solar Atmosphere," pages 49–55 (1996).

Fabling, R.B., Exact magnetic reconnection solutions in three dimensions. Ph.D. thesis, University of Waikato (1997).

Fabling, R.B. and Craig, I.J.D., "Exact solutions for steady-state, planar, magnetic reconnection in an incompressible viscous plasma." *Phys. Plasmas* **3**, 2243 (1996).

Finn, J.M. and Sovinec, C.R., "Nonlinear tearing modes in the presence of resistive wall and rotation." *Phys. Plasmas* **5**, 461 (1998).

Furth, H.P., Killeen, J. and Rosenbluth, M.N., "Finite resistivity instabilities of a sheet pinch." *Phys. Fluids* **6**, 459 (1963).

Galloway, D.J. and Zheligovsky, V.A., "On a class of non-axisymmetric flux rope solutions to the electromagnetic induction equation." *Geophys. Astrophys. Fluid Dyn.* **76**, 253 (1994).

Golub, L. and Pasachoff, J.M., The Solar Corona. Cambridge: Cambridge university Press (1997).

Green, R.M., "Modes of annihilation and reconnection of magnetic fields." In "IAU Symp. 22: Stellar and Solar Magnetic Fields," volume 22, page 398 (1965).

Greene, J.M., "Geometrical properties of three-dimensional reconnecting magnetic fields with nulls." *J. Geophys. Res.* **93**, 8583 (1988).

Heerikhuisen, J., Craig, I.J.D. and Watson, P.G., "Time-dependent magnetic reconnection in two-dimensional periodic geometry." *Geophys. Astrophys. Fluid Dyn.* **93**, 115 (2000).

Heerikhuisen, J., Litvinenko, Yuri E. and Craig, I.J.D., "Proton acceleration in analytic reconnecting current sheets." *Astrophys. J.* (accepted August 2001).

Heyn, M.F. and Semenov, V.S., "Rapid reconnection in compressible plasma." *Phys. Plasmas* **3**, 2725 (1996).

Jardine, M., Allen, H.R., Grundy, R.E. and Priest, E.R., "A family of two-dimensional nonlinear solutions for magnetic field annihilation." *J. Geophys. Res.* **97**, 4199 (1992).

Ji, H.S. and Song, M.T., "Three-dimensional solutions for fan and spine magnetic reconnection in partially ionized plasmas." *Astrophys. J* **556**, 1017 (2001).

Klein, K.L. and Trottet, G., "The origin of solar energetic particle events: Coronal acceleration versus shock wave acceleration." *Space Sci. Rev.* **95**, 215 (2001).

Kobak, T. and Ostrowski, M., "Energetic particle acceleration in a 3d magnetic field reconnection model: a role of mhd turbulence." *Mon. Not. R. Astron Soc.* **317**, 973 (2000).

Lau, Y.T. and Finn, J.M., "Three-dimensional kinematic reconnection in the presence of field nulls and closed field lines." *Astrophys. J.* **350**, 672 (1990).

Litvinenko, Y.E., "Regular versus chaotic motion of charged particles in non-neutral current sheets." *Solar Phys.* **147**, 337 (1993).

Litvinenko, Yu. E. and Somov, B.V., "Particle acceleration in reconnecting current sheets." *Solar Phys.* **146**, 127 (1993).

Litvinenko, Yuri E., "Particle acceleration in reconnecting current sheets with a nonzero magnetic field." *Astrophys. J.* **462**, 997 (1996).

Litvinenko, Yuri E., "Interpretation of particle acceleration in a simulation study of collisionless reconnection." *Phys. Plasmas* **4**, 3439 (1997).

Litvinenko, Yuri E. and Craig, I.J.D., "Magnetic energy release in flux pile-up merging." *Solar Phys.* **189**, 315 (1999).

Litvinenko, Yuri E. and Craig, I.J.D., "Flare energy release in a turbulent current sheet." *Astrophys. J.* **544**, 1101 (2000).

Longcope, D.W. and Strauss, H.R., "The coalescence instability and the development of current sheets in two-dimensional magnetohydrodynamics." *Phys. Fluids B* **5**, 2858 (1993).

Martens, P.C.H., "The generation of proton beams in two-ribbon flares." *Astrophys. J.* **330**, L131 (1988).

Miller, J.A., Cargill, P.J., Emslie, A., Holamn, G.D., Dennis, B.R., Larosa, T.N., Winglee, R.M., Benka, S.G. and Tsuneta, S., "Critical issues for understanding particle acceleration in impulsive solar flares." *J. Geophys. Res.* **102A**, 14631 (1997).

Mori, K., Sakai, J. and Zhao, J., "Proton acceleration near x-type magnetic reconnection region." *Astrophys. J.* **494**, 430 (1998).

Parker, E.N., "Sweet's mechanism for merging magnetic fields in conducting fluids." *Phys. Rev.* **107**, 830 (1957).

Parker, E.N., "The solar flare phenomenon and the theory of reconnection and annihilation of magnetic fields." *Astrophys. J. Supp. Ser.* **8**, 177 (1963).

Parker, E.N., Cosmical Magnetic Fields. Oxford: Clarendon Press (1979).

Parker, E.N., Spontaneous current sheets in magnetic fields. Oxford: Oxford University Press (1994).

Petschek, H.E., "Magnetic field annihilation." In W.N. Hess, editor, "AAS/NASA Symp. on the Physics of Solar Flares," pages 425–439, Washington, DC (1964).

Potter, D., Computational physics. London, New York: J. Wiley (1973).

Priest, E.R., Solar magnetohydrodynamics. Dordrecht: Reidel (1984).

Priest, E.R. and Cowley, S.W.H., "Some comments on magnetic field reconnection." *J. Plasma Phys.* **14**, 271 (1975).

Priest, E.R. and Forbes, T.G., Magnetic Reconnection, MHD theory and applications. Cambridge: Cambridge University Press (2000).

Priest, E.R. and Titov, V.S., "Magnetic reconnection at three-dimensional null points." *Phil. Trans. Roy. Soc. Lond. A* **354**, 2951 (1996).

Richtmyer, R.D. and Morton, K.W., Difference methods for initial-value problems. New York: Interscience, 2d edition (1967).

Ryan, J.M., "Long-duration solar gamma-ray flares." *Space Sci. Rev.* **93**, 581 (2000).

Schopper, R., Birk, G.T. and Lesch, H., "Particle acceleration in three-dimensional reconnection regions: a new test particle approach." *Phys. Plasmas* **6**, 4318 (1999).

Shercliff, J.A., A text book of magnetohydrodynamics. London: Pergamon Press (1965).

Sonnerup, B.U.Ö. and Priest, E.R., "Resistive MHD stagnation-point flows at a current sheet." *J. Plasma Phys.* **14**, 283 (1975).

Spanier, J. and Oldham, K.B., An Atlas of Functions. New York: Hemisphere (1987).

Speiser, T.W., "Particle trajectories in model current sheets." *J. Geophys. Res.* **70**, 4219 (1965).

Spicer, D.S., "An unstable arch model of a solar flare." *Solar Phys.* **53**, 305 (1977).

Stix, M., The Sun, an introduction. Berlin: Springer-Verlag (1989).

Sturrock, P.A., editor, Solar flares. Colorado: Colorado Associated University Press (1980).

Sweet, P.A., "The production of high energy particles in solar flares." *Nuovo Cimento Suppl.* **8**, 188 (1958).

Syrovatskii, S.I., "Formation of current sheets in a plasma with frozen-in strong magnetic field." *Sov. Phys.* **33**, 933 (1971).

Thompson, K.W., Lecture series in computational fluid dynamics. Moffett Field, California: NASA Ames Research Center (1986).

Uzdensky, D.A. and Kulsrud, R.M., "On the viscous boundary layer near the center of the resistive reconnection region." *Phys. Plasmas* **5**, 3249 (1998).

van Hoven, G., Solar flare magnetohydrodynamics (ed E.R. Priest), chapter 4. New York: Gordon and Breach (1981).

Watson, P.G. and Craig, I.J.D., "Analytic solutions of the magnetic annihilation and reconnection problems. Part II: Three-dimensional flows." *Phys. Plasmas* **4**, 110 (1997).

Watson, P.G., Priest, E.R. and Craig, I.J.D., "The roles of advection and diffusion in planar magnetic merging solutions." *Geophys. Astrophys. Fluid Dyn.* **88**, 165 (1998).

Zalesak, S.T., "Fully multidimensional flux-corrected transport algorithms for fluids." *J. Comput. Phys.* **31**, 335 (1979).

Zhu, Z. and Parks, G., "Particle orbits in model current sheet with a nonzero B(y) component." *J. Geophys. Res.* **98A**, 7603 (1993).